Spheroidization in α/β titanium alloys : experimental analysis and numerical modeling

Danai Polychronopoulou

THÈSE DE DOCTORAT

de l'Université de recherche Paris Sciences et Lettres
PSL Research University

Préparée à MINES ParisTech

Spheroidization in α/β titanium alloys: numerical modeling and experimental analysis

Globularisation dans les alliages de titane α/β : analyse expérimentale et simulation

Ecole doctorale n°364 : Sciences Fondamentales et Appliquées

Spécialité : Mécanique numérique et Matériaux

COMPOSITION DU JURY :

Julien BRUCHON
EMSE, Rapporteur

Dominique CHATAIN
Centre Interdisciplinaire de Nanoscience de Marseille, Rapporteur

Frédéric PRIMA
Chimie ParisTech, Président du jury

Yvon MILLET
TIMET, Examinateur

Marc BERNACKI
MINES ParisTech, Examinateur

Nathalie BOZZOLO
MINES ParisTech, Examinateur

Confidentielle jusqu'au 18/07/2019

Soutenue par
Danai POLYCHRONOPOULOU
le **19 juillet 2018**

Dirigée par **Marc BERNACKI**
et **Nathalie BOZZOLO**

Acknowledgements

After an intensive period of four years, this research work has finally come to an end. Writing this note of gratitude is my final touch into this dissertation. Those four past years have been a period of intense learning for me, not only in the scientific and professional arena, but also on a personal level. I would not be able to complete this thesis without acknowledging the support I had by a number of people.

First of all, I would like to express my gratitude to my supervisors Marc Bernacki and Nathalie Bozzolo, for their support, patience and motivation all these years. They helped me the most to bring this research into a conclusion through their guidance and expertise in the field. Most important, they gave me a great opportunity to learn, to grow and to evolve professionally and personally.

I would like also to thank Julien Bruchon, Dominique Chatain, Frédéric Prima and Yvon Millet for accepting being in my jury and reviewing this manuscript. It was a great honor for me to defend my Thesis project in front of them.

A huge thanks to all my colleagues in CEMEF for their support and encouragement throughout all these years. I would like to particularly thank Daniel Pino Muñoz and Thoma Toulorge for the numerous helpful discussions we had. Also, I would like to express my gratitude to Suzanne Jacomet, Gilbert Fiorruci and Cyrille Collin for sharing their experience and expertise in the experimental part of this research with a clumsy simulation engineer like me.

Leaving CEMEF I take with me valuable friendships. I would like to express my gratitude to all my friends in French Riviera for their help and support during this project. Victor, Carlos and Luca thank you for the good laughs, the "scares" and the funny moments and for always having an ear to turn to when things were going bad. Jose Antonio, thank you for encouraging me and for teaching me to stay always optimistic. Modesar, thank you for sharing your knowledge with me and for all the moments we spent arguing about work and non-work related subjects. Marie-Agathe, thank you for showing me that with hard work and determination you can achieve whatever you want in life. Meriem, thank you for always being so kind with me and for always being like a big protective sister of mine. Maria-Nathalie, Maria-Daniela, Juliana, Jose, Luis-Fernando, Ghalia, Wafa, Chahrazad, Gabriel, Shitij, Pierre, Geraldine, Miren and Laura, I will never forget our lunch meetings, our coffee breaks, our parties and all the good times that we spent together. Meeting all of you have helped me to broaden my horizons and become a better person.

Special thanks to all my Greek friends Eleni, Evi, Giota, Georgia, Anargyros and Nikos for their presence and support despite the physical distance between us. I would like also to express my gratitude to Ioannis Politopoulos for his kind help and guidance regarding my work as well as everyday life issues during my four years stay in France.

Last but not least, I would like to express my gratitude to all my extended family back in Greece; sister, cousins, aunts, godmother and grandparents for always staying by my side whatever I might choose to do in life. Most of all, I would like to dedicate this Thesis to my parents Anna and Kostas for always being there for me when I need them and for teaching me to never give up and follow my dreams. They made me the person I am today.

Σας ευχαριστώ όλους μέσα από τα βάθη της καρδιάς μου!

Danai/Δανάη

Contents

List of Figures

List of Tables

Introduction

Spherodization is a microstructural phenomenon occurring in α/β titanium alloys during thermomechanical treatment, which may be described as follows. Starting from an initial lamellar microstructure of α colonies inside former β grains, a globular morphology of the α phase can be obtained by applying hot deformation and subsequent annealing. In the case of α/β titanium alloys, the spheroidized microstructure exhibits higher strength and ductility. For that reason, this phenomenon received considerable attention in the literature and industry.

α/β titanium alloys have various applications in many industrial fields such as aeronautics and biomechanics. The importance of spheroidization lies in the concept of microstructural control, and in turn of the alloy properties. Simulating microstructural evolution would allow saving time and would avoid going through expensive experiments to design processing routes for getting better or optimum material properties. In order to develop models for simulating the evolution of the microstructure, it is important to get first an insight onto the microstructural changes that the α/β titanium alloys get through thermomechanical treatment. Understanding the phase transformation and diffusion mechanisms occurring in the microstructure during thermomechanical treatment is essential for proposing physically based numerical methods that will efficiently and realistically simulate the involved phenomena.

There are several papers in literature describing spheroidization based on experimental observations but very little has been done towards modeling it. The phenomenon of spheroidization has been reported to occur in different stages and with the contribution of many different mechanisms. Long term annealing is not enough to break lamellar structures down and observe shape evolution, but deformation is needed.

Provided the complexity of the phenomenon, it would not be possible to take all the contributing mechanisms into account to build a complete model within the frame of a PhD work. The focus of the present work has therefore been placed on the interfacial kinetics mechanisms leading lamellae splitting, during isothermal post-deformation annealing. This is a necessary step before going into more complete modeling, where crystal plasticity and diffusive phase transformation mechanisms should also be considered.

Layout of the thesis

The thesis is organized in four chapters:

- Chapter 1 first covers a literature review regarding spheroidization phenomenon. Information regarding the involved mechanisms are presented. Furthermore, a mathematical description of interfacial kinetics leading to α lamellae splitting is detailed.

- In chapter 2, an experimental study/analysis of results coming from hot compression tests with Ti-64 material is detailed.

- In chapter 3, a full field model based on a Finite Element/ Level Set framework simulating the α lamellae splitting is detailed. Two different approaches are considered and tested. Academic cases validating the proposed methodologies are presented.

- In chapter 4, first simulations on real microstructures extracted from experimental images using the introduced numerical framework are presented and discussed.

Publications and Conferences

The work of this thesis has contributed to the following publications and conferences:

Articles

D. Polychronopoulou et al. Introduction to the level-set full field modeling of laths spheroidization phenomenon in α/β titanium alloys. International Journal of Material Forming, 2017. https://doi.org/10.1007/s12289-017-1371-6

Proceedings

D. Polychronopoulou et al. Introduction to the level-set full field modeling of laths spheroidization phenomenon in α/β titanium alloys. MATEC Web of Conferences, 80(02003), 2016.

International conferences

D. Polychronopoulou et al. Introduction to the level-set full field modeling of laths spheroidization phenomenon in α/β titanium alloys. In NUMIFORM

2016, Troyes, France, July 04-07 2016.

D. Polychronopoulou et al. Full-field modeling of spheroidization phenomenon in α/β titanium alloys during hot-deformation and subsequent annealing at a given temperature. EUROMAT 2017, Thessaloniki, Greece, Sept. 2017.

National conferences

- M. Bernacki, D. Polychronopoulou and N. Bozzolo. Full-field modeling of spheroidization phenomenon in α/β titanium alloys after deformation and during the annealing stage at a given temperature. Journées Technologiques Titane, 30-31 Mai 2017. Invited conference.
- D. Polychronopoulou et al. Full field modelling of lamella splitting and lath spheroidization in α/β titanium alloys. Colloque "Métallurgie, quel avenir!", Saint-Etienne, France, 27 Juin-01 Juillet 2016.
- M. Bernacki, N. Bozzolo, Y. Jin, B. Scholtes, R. Boulais-Sinou, D. Polychronopoulou and D. Ilin. Advances in level set modeling of recrystallization at the mesoscopic scale. 2eme Journées Matériaux Numériques, St-Aignan-sur-Cher, France, 03-05 Février 2015. Invited Conference.

Acknowledgment

I would like to thank AUBERT&DUVAL, TIMET, CEA and SAFRAN for funding this work within the industrial SPATIALES project.

Chapter 1

Literature Review

Résumé en français

Dans ce chapitre, une revue de la littérature concernant le phénomène de globularisation dans les alliages des titanes α/β est présenté. Les microstructures lamellaires des alliages de titane α/β sont constituées de colonies de lamelles de phase α parallèles qui se développent dans les grains β au cours de leur refroidissement. La globularisation est un phénomène qui se produit lors de la compression à chaud et du traitement thermique subséquent. Selon la littérature, la globularisation se fait en deux étapes: les lamelles se subdivisent d'abord en segments plus courts, puis ces segments globularisent. La subdivision des lamelles se fait au niveau des sous-joints formés au cours de la déformation à chaud. Lors de traitements thermiques prolongés, les plus gros globules de phase α grossissent au détriment des plus petits.

Tous les mécanismes prédominants de ce phénomène, qui ont été étudiés dans la littérature, sont analysés en détail dans ce chapitre. La plasticité cristalline est responsable de la formation de sous-joints dans les lamelles α au cours de déformation à chaud. La subdivision de lamelles de phase α est la conséquence des mécanismes simultanés de migration des interfaces α/β et interfaces α/α des sous-joints. De plus, le grossissement des particules de phase α est produit de diffusion volumique.

En ce qui concerne la partie modélisation, dans ce chapitre l'accent a été mis sur le modèle mathématique pour la description des deux mécanismes de migration des interfaces qui conduisent à la subdivision des lamelles et à leur globularisation.

1.1 Literature review on the physical description of the phenomenon of spheroidization in α/β titanium alloys

1.1.1 Titanium alloys and the studied Ti-64 alloy

Titanium alloys are materials with high strength, fatigue and corrosion resistance, low density and good ductility. Due to these characteristics, they have preferential use in the aerospace domain, biomedical engineering and energy/power industry [1]. Pure titanium exhibits an allotropic phase transformation at 882 °C from a hexagonal close packed crystallographic structure (HCP, α phase, stable at low temperature) to a body centered cubic crystallographic structure (BCC, β phase, stable at high temperature).

Microstructural evolution in titanium alloys is strongly dependent on this allotropic transformation and on the alloying elements, which govern the stability of both phases. In titanium alloys, the β phase can indeed be partially stabilized at low temperatures and the equilibrium volume fractions of α and β phases vary with temperature. The temperature at which a specific alloy becomes entirely composed of β phase is called β-transus. The β-transus temperature is a value relative to which the thermomechanical processing conditions are chosen [1, 2].

Commercial titanium alloys are classified conventionally into three different categories α, β and α/β alloys, based on the amount of β phase retained at room temperature.

- β and near β alloys have large to moderate amounts of β-stabilizing elements such as vanadium, molybdenum, chromium and iron. Their β transus temperature is typically in the range of 700 °C to 850 °C [1].
- The group of α alloys contain no or low volume fraction of β phase (2-5 vol %) at room temperature [1].
- The α/β titanium alloys contain a combination of α and β stabilizing elements. The two phases are coexisting at room temperature. The β transus temperatures of α/β titanium alloys are typically between 950 °C and 1050 °C [1].

The existence of two different crystal structures and the corresponding phase transformation are the main reasons of the appearance of a variety of properties in titanium alloys. The deformation temperature, the temperature of thermal treatments, as well as the cooling rates, are very important factors in the control of the final microstructure [2]. There are several metallurgical phenomena that take place in titanium alloys during thermomechanical processing and play a major role in controlling the final microstructure.

Solid state phase transformations, recrystallization and grain growth phenomena in single or two-phase alloys, spheroidization and coarsening of α phase in α/β alloys after hot forging are some examples of these phenomena.

Materials science is an extended domain that ranges from the microscopic atomic behavior of the material to the macroscopic mechanical behavior. The deep understanding of microstructural evolution is a necessity in many engineering fields, nowadays. Thanks to the microstructural control, structures with enhanced properties and desirable features can be built. This PhD work is focused on the phenomenon of spheroidization of α phase during thermomechanical treatment of α/β titanium alloys, with the Ti-64 alloy as a model material.

Ti-64 is the mostly used titanium alloy in industry. Its low density, high corrosion resistance and good strength-ductility balance makes it very popular for numerous industrial applications such as high-performance automotive parts, marine applications, medical devices and most of all in aircraft structural parts [1–6]. The mechanical properties of the alloy are very dependent on its microstructure. The chemical composition of Ti-64 or Ti-6Al-4V or TA6V as it is also denoted, contains $\sim$6 wt%Al and $\sim$4 wt%V and small amounts of other elements like Fe, Si, Zr, C (balance Ti). Ti-64 microstructural morphology builds up by a series of thermomechanical processing steps [1–9]. Thermomechanical processing must be optimized to obtain a suitable microstructure. A uniform equiaxed microstructure of primary α phase inside a matrix of transformed β offers a good compromise of mechanical properties. After casting, the produced ingots are typically hot-worked and heat-treated above the β transus temperature (i.e. within the single β phase domain) to eliminate casting inhomogeneities. After this stage, during cooling from the β phase region, the α phase forms. Depending on the cooling rate, the α phase appears in the form of small equiaxed grains at β grain boundaries and triple junctions (called primary α phase), or in the form of α lamellae colonies, or in the form of very fine acicular martensitic α phase inside β matrix [1–9]. As a general trend, the microstructure goes finer when increasing the cooling rate.

The phenomenon of spheroidization consists, at stable phase proportions, in the breaking of initial lamellar microstructures during deformation and subsequent heat treatment in order to obtain a globular α phase form that finally gives enhanced strength and ductility. For this PhD work, the Ti-64 material was provided with a lamellar microstructure. In the following section, more informations are provided regarding the formation of α colonies inside former β grains.

1.1.2 Lamellar $\alpha - \beta$ microstructures

The microstructure of α/β titanium alloys is basically described by the size, the volume fraction and the arrangement of the two phases α and β.

Microstructures with α lamellae are generated by phase transformation from β phase, while cooling down from the β domain. When the temperature falls below the β transus temperature, α phase nucleates at grain boundaries and then grows as lamellae into the prior β grain, with a thickness which depends on the cooling rate [1–9] . The initial α phase nucleation at the β/β grain boundaries leads to a more or less continuous α layer along boundaries, that is often called α_{GB}. Prior β grains can be as large as several millimeters. Sets of parallel lamellae (called α colonies) grow into the same direction inside β grains following a specific orientation relationship (Fig. 1.1) [1].

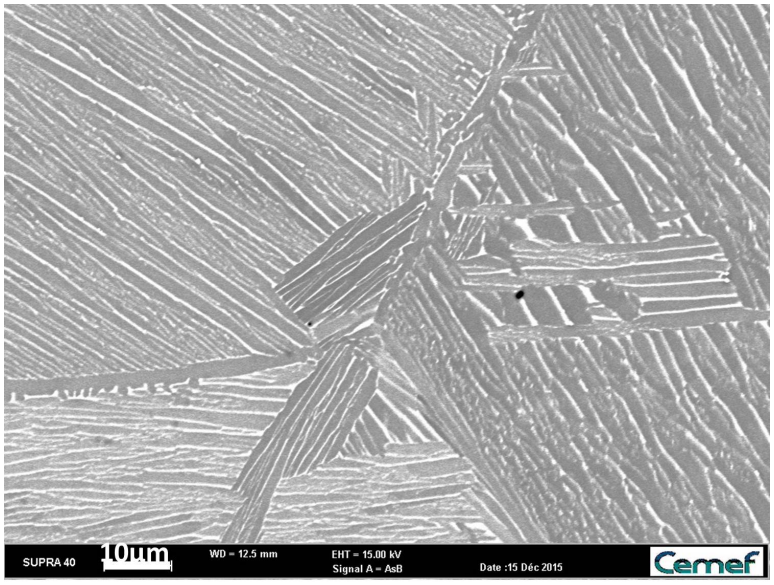

Figure 1.1: Backscattered electron micrograph showing α lamellae colonies in former β grains in a Ti-64 sample (LX2 as received material).

The β to α phase transformation is such that the most densely packed planes of the BCC β phase $\{110\}$ transform into the basal plane $\{0001\}$ of the hexagonal α phase. Within those planes the dense directions $< 111 >_\beta$ become $< 11\bar{2}0 >_\alpha$. This orientation relationship between β and α phase is referred to as the Burgers relationship [1, 2].

It has been shown that for an α/β two phase mixture, the Burgers orientation relationship between the α and β phases provides an easy slip transmission across the α/β interface since the respective close packed planes $\{0001\}_\alpha/\{110\}_\beta$ and the close packed directions $< 11\bar{2}0 >_\alpha /< 111 >_\beta$ are parallel [1–3].

In a β grain there are six $\{110\}_\beta$ planes, each containing two $< 111 >_\beta$ directions, on which an α variant/colony can form. So, there are 12 α variant orientations in a prior β grain which satisfy the Burgers orientation relationship Table 1.1.

Variants	Orientation relationships
A	$(1\bar{1}0)_\beta//(0001)_\alpha, <111>_\beta <11\bar{2}0>_\alpha$
B	$(10\bar{1})_\beta//(0001)_\alpha, <111>_\beta <11\bar{2}0>_\alpha$
C	$(01\bar{1})_\beta//(0001)_\alpha, <111>_\beta <11\bar{2}0>_\alpha$
D	$(110)_\beta//(0001)_\alpha, <\bar{1}11>_\beta <11\bar{2}0>_\alpha$
E	$(101)_\beta//(0001)_\alpha, <\bar{1}11>_\beta <11\bar{2}0>_\alpha$
F	$(01\bar{1})_\beta//(0001)_\alpha, <\bar{1}11>_\beta <11\bar{2}0>_\alpha$
G	$(110)_\beta//(0001)_\alpha, <1\bar{1}1>_\beta <11\bar{2}0>_\alpha$
H	$(10\bar{1})_\beta//(0001)_\alpha, <1\bar{1}1>_\beta <11\bar{2}0>_\alpha$
I	$(011)_\beta//(0001)_\alpha, <1\bar{1}1>_\beta <11\bar{2}0>_\alpha$
J	$(1\bar{1}0)_\beta//(0001)_\alpha, <11\bar{1}>_\beta <11\bar{2}0>_\alpha$
K	$(101)_\beta//(0001)_\alpha, <11\bar{1}>_\beta <11\bar{2}0>_\alpha$
L	$(011)_\beta//(0001)_\alpha, <11\bar{1}>_\beta <11\bar{2}0>_\alpha$

Table 1.1: 12 possible crystallographic orientations of the α colonies inside a (prior) β grain, which arise from the Burgers orientation relationship.

In a given β grain, the α lamellae can nucleate and grow according to the 12 orientations listed in Table 1.1. The lamellae of a given colony have the same crystallographic orientation. The orientation change across the colony boundaries prevents the slip transmission. Therefore, the nature of the colony boundaries and their orientation change are important factors for understanding deformation mechanisms in these alloys [1, 3].

1.1.3 The importance of the phenomenon of spheroidization

Spheroidization is the shape evolution of α phase from a lamellar form to an equiaxed form. It is a very important phenomenon for microstructure and properties control in two-phase titanium alloys as well as in two-phase carbon steels. In the case of α/β titanium alloys, spheroidization appears after hot working and thermal treatment (Fig. 1.2). The lamellar microstructure has moderate strength, fatigue resistance and crack growth resistance but low ductility. In contrast, a microstructure comprising globular α phase has enhanced strength and ductility [4].

One of the main goals of this PhD work is a better understanding of the mechanisms occurring during spheroidization in α/β titanium alloys, in order to build a numerical model which could efficiently describe the phenomenon. In the following sections of this chapter, the information available in the literature with regards to the thermodynamic driving forces of spheroidization and the related mechanisms will be described.

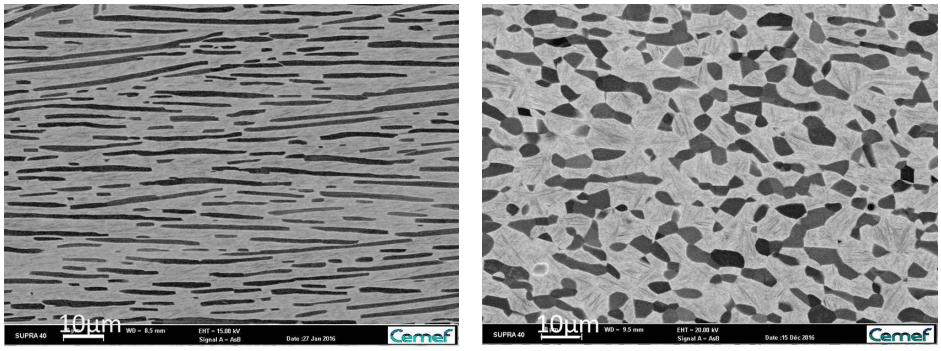

(a) (b)

Figure 1.2: Backscattered electron micrographs showing the spheroidization of Ti-64 alloy. (a) Microstructure after 30 min holding at 950 °C set as initial state for our research of microstructural evolution and (b) microstructure after hot-deformation and thermal treatment at 950 °C. The α phase is dark and the light grey regions is β- transformed.

1.1.4 Literature review regarding spheroidization

There are quite few papers in the literature concerning the experimental study of spheroidization in titanium alloys [1–9]. Those papers provide informations regarding the evolution of the microstructure topology as well as theories concerning the involved mechanisms.

Margolin and Cohen [8, 9] were the first to report on the fragmentation of the α lamellae during hot working and subsequent annealing. They suggested that recrystallized α grains are formed within the α lamellae and that there is a driving force for the penetration of the β phase along the α/α boundaries something that leads to the segmentation of the lamellae.

Later, Weiss et al. [7] described the α lamellae morphology change as a two steps process that occurs during hot-working and subsequent annealing. The first step is the formation of sub-boundaries inside the α lamellae or the appearance of shear bands across the α lamellae. It is followed by the penetration of the β phase to complete separation. If the initial strain is large enough the lamellae are fragmented immediately due to the formation of intense shear bands. Otherwise, if the strain is not so high, sub-boundaries appear and help the penetration of β phase into α phase. Weiss et al [7] also noticed that the thickness of the lamellae plays an important role. Lamellae are splitted easier and faster if they are initially thinner.

Mironov and Zherebtsov have used the EBSD technique to investigate microstructural evolution during warm working of Ti-64 alloy starting from a α colony microstructure [3, 4]. Kinking of the lamellae is reported in the colonies that were initially perpendicular to the compression axis [3]. What is called kinking of the lamellae is the bending of the lamellae under the

applied strain and this leads to faster splitting into shorter laths (Fig. 1.3). On the other hand, the colonies which were initially not perpendicular to the compression axis simply tend to align with the matter flow orientation. The lamellar structure actually appears to be surprisingly stable during warm deformation and only the kinked lamellae seem to start spheroidizing.

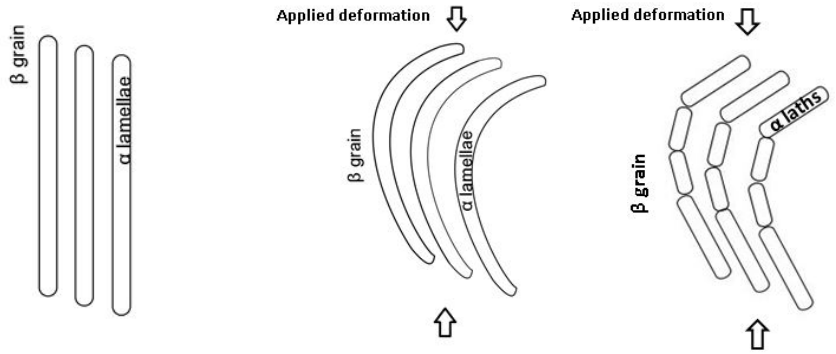

(a) (b) (c)

Figure 1.3: Lamellae splitting promoted by lamellae kinking: (a) lamellae initially vertical, (b) kinking and (c) splitting of the lamellae into smaller laths.

Later, they showed that the behavior of Ti-64 alloy microstructure during warm working and subsequent annealing is temperature dependent. They indeed suggest that the fragmentation of α lamellae is controlled by classical boundary splitting mechanisms and the subsequent spheroidization of the remaining α laths by means of termination migration [4]. The same group of authors also studied the formation of boundary misorientation spectrum in α/β titanium alloys [10]. The results showed that the accumulation and redistribution of dislocations result in the formation of sub-boundaries inside α lamellae which leads to their fragmentation. They also observed that the process depends on the lamellae orientation. Moreover, the strain distribution along the length of the lamellae is noticed to be non-uniform. Again, these authors report that the β phase penetrates into the α phase where sub-boundaries were formed.

Stefanson and Semiatin [2,5] studied in depth the phenomenon of static spheroidization (i.e. during annealing after deformation) and provided more information. In [5], the idea that spheroidization occurs in two stages is again supported, but with a somewhat different definition of the two stages. The first stage is the segmentation of the lamellae by boundary splitting and edge spheroidization which takes place during deformation and the early stages of static annealing. The second stage occurs over longer-term annealing and corresponds to microstructure coarsening by mechanisms such

as termination migration and Ostwald ripening. Furthermore, in [6] it is clearly proved that the kinetics of spheroidization depend on the strain level applied prior to heat treatment as well as on the heat treatment temperature. On the other hand, according to [6] the deformation temperature does not seem to be an important factor for the shape evolution of the α lamellae, at least within the temperature range explored in this work (compression tests done at temperatures between 900 °C and 955 °C).

Semiatin and Furrer [2] made a more complete description of the sequence of mechanisms governing spheroidization in an attempt to introduce a mathematical description of the phenomenon. The first stated mechanism is the localization of strain into intense shear bands inside the α lamellae, that eventually leads to their fragmentation. The limited number of available slip systems in HCP titanium (α phase) together with the anisotropy of the β phase favors strain localization and result in the appearance of intense shear bands that will subsequently lead to fragmentation. Here we can connect the shear band mechanism with the lamellae kinking mechanism since they both seem to lead to very fast lamellae fragmentation during hot deformation.

Both Semiatin [2] and Mironov et al. [3, 4] showed that, due to crystal plasticity, dislocations accumulate inside the α lamellae during deformation and lead to the formation of local crystal misorientations inside the α lamellae and in turn to α/α sub-boundaries. By subsequent annealing, these sub-boundaries lead to the formation of grooves at the surface of α lamellae, driven by atomic diffusion kinetics due to differences in chemical potentials between the α/α sub-boundaries and the α/β interface. The formation of grooves during deformation plays a key role for the following phenomenon of spheroidization (see Fig. 1.4) [2, 3, 7].

Semiatin in [2] addresses the already observed phenomenon of the penetration of β phase in the α phase as a grooving-related mechanism. He basically states that the penetration of the β phase where α/α sub- boundaries formed during deformation can be described using classical approach for grain boundary grooving originally developed by Mullins [11]. Though Mullins originally refers to the interaction of a grain boundary with a free surface, the approach could also be used for the interaction of α/α sub-boundaries with the α/β interphase boundary. In both cases, interfaces (solid/vacuum or α/β) evolve due to atomic surface/volume diffusion phenomena.

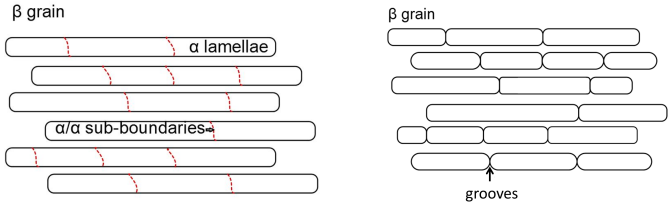

(a) (b)

Figure 1.4: Formation of grooves at the α/β interfaces due to the existence of internal α/α sub-boundaries: (a) microstructure after deformation where the sub-boundaries are appearing and (b) microstructure after thermal treatment where grooves are schematized.

Two phase alloys with lamellar microstructure are generally thermodynamically unstable due to their large interfacial area. After deformation the interfacial energy is even higher. First, the initial α/β interfaces (formed during cooling from the β domain (see paragraph 1.1.2) have a relatively low energy, but after deformation, both their misorientation and habit planes are very likely to have changed as a result of dislocation storage and/or plastic flow. The α/β interface energy is thus likely to be higher. In addition, the formation of sub-boundaries and lamellae fragmentation increases the interface area per unit volume. Reducing the interfacial energy constitutes a thermodynamic driving force for further microstructure evolution. Moreover, the interfacial energy balance between the α/β interfaces and the α sub-boundaries promotes local atomic diffusion, leading to grooving at the lamellae surface and finally to lamellae splitting into α laths with pancake shapes.

To reduce the free energy associated with the interfaces, two phase systems generally tend to adopt spheroidal topologies which minimize the surface to volume fraction ratios as compared to other morphologies (assuming that the interfacial energy is isotropic). Moreover, the gradient of chemical potentials provides a driving force for interfacial diffusion from the curved areas of α particles towards the flat ones. Subsequent coarsening of α globules (Ostwald ripening) is driven by the same minimization of the free energy associated with the interfaces and involves volume diffusion mechanisms.

Motion by surface diffusion at the α/β interfaces and motion by mean curvature at the α sub-boundaries (implying Young's law at the multiple junctions), occur simultaneously during deformation and at the first stages of the subsequent annealing. Both lead to the split of α lamellaes into α laths. Subsequent evolution of α laths towards a more spherical morphology is directly due to the motion by surface diffusion.

α/β interface motion by surface diffusion is initiated by differences in chemical potentials along α/β interface. Then it is obesreved the motion

of atoms between curved areas of the α lamellae towards the flat ones (see Fig. 1.5). In the Ti-64 alloy, the diffusion rate limiting solute is vanadium and as a result these atoms control the surface diffusion kinetic. At this point it is important to notice that in addition to the high interfacial energy obtained after deformation that promotes interface motion, temperature is also a very important factor that enhances the mobility of the interfaces.

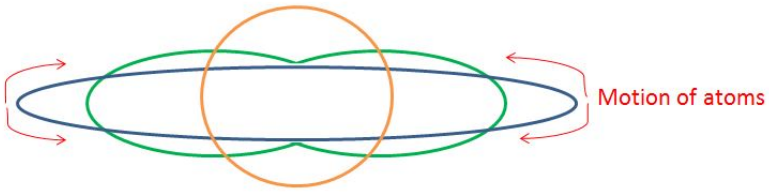

Figure 1.5: α lath morphology evolution due to surface diffusion from high to low curvature areas.

The α/α sub-boundaries formed during deformation interact with the α/β interfaces and also contribute to the shape evolution of the lamellae. Indeed, the respect of Herring's [12, 13] equation at the multiple junctions, derived from the local mean curvature driving force, between the α/β lamellae interfaces and the α/α sub-boundaries interfaces contribute in the appearance of grooves (see Fig. 1.6).

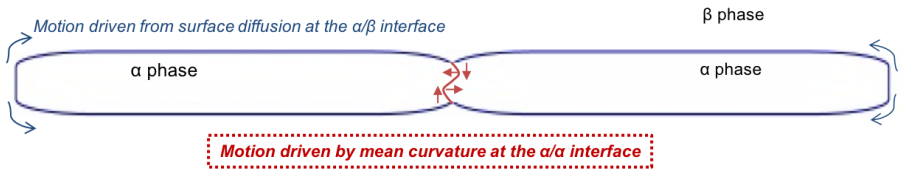

Figure 1.6: Splitting of a lamellae due to the combined effects of interface motion by surface diffusion at the α/β interface and the motion by mean curvature at the α/α interface.

The mechanisms described above are occurring during deformation and first stages of subsequent annealing. According to Semiatin and Stefanson et al. [2, 5, 6] another mechanism becomes the governing one during prolonged annealing, that is the coarsening mechanism. After the splitting of the lamellae, the α laths keep evolving and coarsen in order to minimize the α/β interfacial energy. The surface diffusion mechanism keep being active during annealing until the α laths reach the equilibrium state of a shape of minimized interfacial area (sphere if the interfacial energy is isotropic). On the other hand, coarsening involves bulk diffusion with the motion of atoms

from the smaller α particles with higher interface curvature to the bigger ones with lower curvature (phenomenon known as Ostwald ripening). This results in the disappearance of smaller particles and the growth of the bigger ones.

The complexity of the phenomenon does not stop here though. Indeed, during deformation, stress at the grain interfaces can also lead to grain boundary diffusion involving atoms moving along the grain boundaries. Moreover, literature on α/β titanium alloys [14–18] also shows that the α/β phase equilibrium is not the same under static or dynamic conditions, the β phase being promoted under hot-deformation conditions. For Ti-64 alloy, the higher the deformation the more the β phase volume fraction increases during deformation [14]. In this work, it is clearly stated that there is a strain threshold above which the β phase starts increasing significantly. The exact physical reasons for this shift in the thermodynamic equilibrium does not seem to be clear yet but may involve a change of Gibbs energies of both phase under the applied stress, the contribution of crystalline defects to that Gibbs energies, in addition to a possible stress-enhanced atomic diffusion. During isothermal annealing after hot-deformation, the α and β phase volume fractions get back to the static equilibrium values [14, 15]. Here, eventhough there is no obvious reason why that phenomenon would be sensitive to the phase topology, it is important to underline the fact that the cited literature does not refer to α/β alloys with initial lamellae microstructure. In the present work aiming at modelling of spheroidization, this dynamic equilibrium issue will not be considered, and the volume fractions will thus be considered to be constant during deformation and equal to the static phase equilibrium values reached before deformation starts.

1.2 Literature review on the mathematical description of interface kinetics

In this thesis the focus will mainly be placed on the simulation of two interface motion mechanisms, driven by surface diffusion and by mean curvature. The combined effect of both mechanisms leads to the grooving and subsequent splitting of the α lamellae.

1.2.1 Mullins model for thermal grooving

The mathematical model which will be used is based on the historical article of Mullins [11]. This paper describes the kinetics of a thermal groove formed where a grain boundary meets a free surface. Semiatin in [2] points out that the same model can be used to describe the grooving of α lamellae during spheroidization, by considering the kinetics of the α/α sub-boundary meeting the α/β interface.

Grooving is initiated by atomic-scale processes near the region of the α/α boundary and α/β interface intersection, and for the semi-infinite configuration of Fig. 1.7 a groove angle δ appears. Thanks to the Herring's equation [12, 13] in a context of a constant γ energy per interface and by a simple projection of the surface tension vectors on the α/α plane of the Fig. 1.7, the dihedral angle δ satisfies:

$$2\gamma_{\alpha\beta}\cos(\delta/2) = \gamma_{\alpha\alpha}. \tag{1.1}$$

Mass transfer from the curved areas to the flatten edges (as a result of curvature induced chemical potential gradients) leads to the development of the groove. This can thus be described by surface diffusion equations at α/β interfaces and motion by mean curvature equation at α/α sub-boundaries (Fig. 1.7). Both sets of equations will be presented in the following paragraphs.

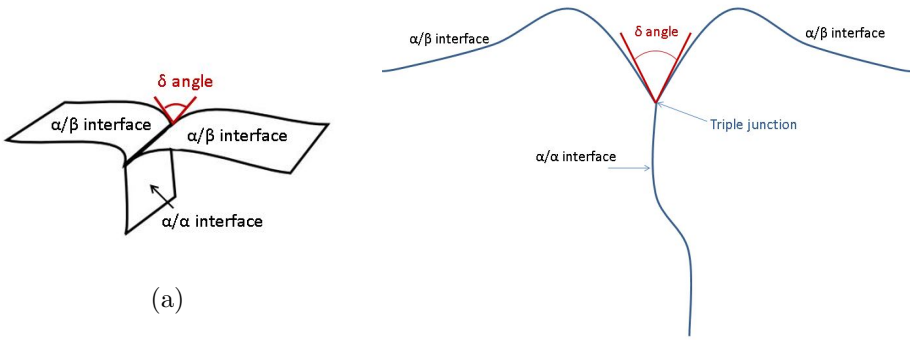

(a) (b)

Figure 1.7: Formation of a groove angle due to interaction of a α/α sub-boundary and a α/β interface: (a) a 3D diagram and (b) a 2D diagram.

1.2.2 Motion by surface diffusion at the α/β interfaces

According to Mullins [11], atomic flow at the α/β interface can be described by a surface flux $\vec{j}$:

$$\vec{j} = \nu\vec{v}, \tag{1.2}$$

where ν denotes the number of drifting atoms per unit area and $\vec{v}$ denotes the average velocity of the drifting atoms. Assuming local equilibrium, $\vec{v}$ can be expressed using the Nernst-Einstein formula as follows :

$$\vec{v} = \frac{D_{\alpha\beta}}{kT}\nabla_s\mu, \tag{1.3}$$

where $D_{\alpha\beta}$ denotes interfacial diffusivity, μ the chemical potential , k is the Boltzmann constant and T the absolute temperature. The ∇_s operator denotes the surface/interface gradient, defined as the tangential component of the gradient:

$$\nabla_s \mu = \nabla\mu - (\nabla\mu \cdot \vec{n})\vec{n} = P\nabla\mu, \tag{1.4}$$

with $\vec{n}$ the outward-pointing unit vector normal to the interface and P the matrix defined as $I - \vec{n} \otimes \vec{n}$ with I the identity matrix. Combining Eq. 1.2 and Eq. 1.3, we obtain the following equation:

$$\vec{j} = \frac{\nu D_{\alpha\beta}}{kT} \nabla_s \mu. \tag{1.5}$$

If we consider mass conservation, the evolution of the interface can then be described by the normal velocity to the interface:

$$\vec{v} = v_s \vec{n} = -\Omega \nabla_s \vec{j}, \tag{1.6}$$

where v_s denotes the surface diffusion velocity (here of vanadium) and Ω denotes the atomic volume. Combining Eq. 1.5 and Eq. 1.6 we obtain:

$$v_s = -\frac{\nu \Omega D_{\alpha\beta}}{kT} \Delta_s \mu, \tag{1.7}$$

with $\Delta_s = \nabla_s \cdot \nabla_s$ the surface laplacian operator (also called Laplace-Beltrami operator).

As it is observed from Eq. 1.7, the normal velocity is associated with the chemical potential. By considering κ as the mean curvature (sum of the main curvatures in 3D) and $\gamma_{\alpha\beta}$ the α/β interface energy without taken into account its possible anisotropy, chemical potential μ can be related to the mean curvature κ by Eq. 1.8 [19, 20]:

$$\mu = -\gamma_{\alpha\beta} \Omega \kappa. \tag{1.8}$$

Eq. 1.8 implies that a decrease in the α/β interface mean curvature leads to a decrease in the chemical potential, which in turn leads to a decrease in the total interface energy. Using Eq. 1.7 and Eq. 1.8, the motion of the interface can be described as:

$$v_s = \frac{\gamma_{\alpha\beta} \nu \Omega^2 D_{\alpha\beta}}{kT} \Delta_s \kappa. \tag{1.9}$$

By defining

$$B = \frac{\gamma_{\alpha\beta} \nu \Omega^2 D_{\alpha\beta}}{kT}, \tag{1.10}$$

as kinetic coefficient, we obtain:

$$v_s = B \Delta_s \kappa. \tag{1.11}$$

Eq. 1.11 describes the relation between the motion due to surface diffusion and the surface laplacian of the mean curvature [11, 21].

Several factors that can affect the α/β interface energy $\gamma_{\alpha\beta}$ and the interfacial diffusivity $D_{\alpha\beta}$. Semiatin, nevertheless, provided an approximation of the value $\gamma_{\alpha\beta}$ around 0.2- 0.4 $J \cdot m^2$ [21]. The α/β surface energy $\gamma_{\alpha\beta}$ is likely to be very anisotropic, but its anisotropy remains difficult to estimate. That is why anisotropy will be ignored in this work. Diffusivity is also influenced by several factors such as temperature, stress and the presence of dislocations. Diffusivity coefficients are likely to be very sensitive to changes in thermomechanical paths. Diffusivity coefficients of the limiting solutes of titanium alloys can be found in literature, in the form of experimental plots [22]. Semiatin [21], for Ti-64, refers to the diffusivity of the vanadium as the most influential one and uses this one in his models with a value of $D_{\alpha\beta} = 0.048\mu m^2/s$ at T=950 °C. A global discussion on the physical parameters is presented in the last chapter.

1.2.3 Motion by mean curvature at the α/α interfaces

The $\gamma_{\alpha\alpha}$ grain boundary energy is very important for boundary grooving. The relation between mean curvature motion and grain boundary energy is given by the well known Gibbs-Thompson relationship where the normal velocity $v_\kappa \vec{n}$ of the grain boundary is described as being proportional to the mean curvature κ:

$$v_\kappa = -\kappa \frac{\gamma_{\alpha\alpha} b f \Omega}{kT} e^{-\frac{Q}{RT}}, \tag{1.12}$$

with R the gas constant, b the norm of the Burgers vector, f the Debye frequency, $\gamma_{\alpha\alpha}$ the surface energy of the α/α boundary, and Q the activation energy. Eq. 1.12 can be re-written as:

$$v_\kappa = -A\kappa, \tag{1.13}$$

with:

$$A = \frac{\gamma_{\alpha\alpha} b f \Omega}{kT} e^{-\frac{Q}{RT}}. \tag{1.14}$$

1.2.4 Global equation for α lamellae splitting coupling both motions

As surface diffusion and mean curvature motions are taking part simultaneously during the phenomenon of globularization, we should proposed a numerical framework combining them. So the final form of our equation will be:

$$\vec{v} = (v_s + v_\kappa)\,\vec{n} = (B\Delta_s\kappa - A\kappa)\,\vec{n} \tag{1.15}$$

where B is defined by Eq. 1.10 in α/β interfaces and 0 elsewhere and A is defined by Eq. 1.15 in α/α interfaces and 0 elsewhere.

1.3 Summary

In this chapter, a literature review regarding the phenomenon of spheroidization has been presented. All the known governing mechanisms have been analyzed in detail as they were found in various papers. Regarding the modeling part, the focus was placed on the interface kinetics. A mathematical description of the two governing mechanisms of motion by surface diffusion and motion by mean curvature has been given. These two mechanisms are responsible for the α lamellae splitting.

In the following chapter, we are going to present an experimental analysis of results obtained after hot compression tests of Ti-64 samples.

Chapter 2

Experimental analysis of the metallurgical processes leading to spheroidization

Résumé en français

Dans ce chapitre, les résultats d'analyse expérimentale du phénomène de globularisation sont présentés. D'abord, le plan expérimental est expliqué en détail. Des échantillons biconiques de Ti-6Al-4V sont utilisés. Des essais de compression à chaud à 950 °C et des traitements thermiques sont effectués. Pour la caractérisation de la microstructure, les techniques de microscopie électronique à balayage (Scanning Electron Microscopy ou SEM en anglais) et de diffraction d'électrons rétrodiffusés (Electron Backscatter Diffraction ou EBSD en anglais) sont utilisées.

L'analyse expérimentale de ces résultats confirme que l'épaisseur des lamelles et leur orientation sont des facteurs importants pour la globularisation. Les lamelles plus fines et celles orientées parallélement à l'axe de compression globularisent plus facilement. Il est aussi prouvé que les sous-joints qui sont arrivé dans les lamelles α pendant la déformation sont essentiels pour l'évolution de la microstructure. Ce sont eux qui introduisent des instabilités dans les lamelles et déclenchent les mécanismes interfaciaux qui mènent à l'évolution de la forme de la phase α. De plus, en effectuant des traitements thermiques de durées différentes suivis d'une déformation, il est prouvé que la globularisation n'a lieu qu'après des traitements thermiques prolongés.

Ce travail expérimental a permis de mieux appréhender la complexité du phénomène de globularisation et de clarifier des mécanismes physiques prédominants aux différentes étapes du phénomène. Il a aussi aidé à introduire un cadre numérique adapté pour la simulation de la globularisation.

2.1 As received materials and experimental plan

Experiments consisting of thermomechanical tests, heat treatments and microstructure characterization were performed to help getting a general understanding of the behavior of the material with regards to α lamellae fragmentation and subsequent spheroidization. The second aim of those experiments is to collect quantitative information to enable us to model the phenomenon more efficiently and to have a reference for comparing/validating our numerical results. As already mentioned in chapter 1, the phenomenon of spheroidization in microstructures initially made of α colonies inside β grains proceeds in two steps. The first step is the splitting of the α lamellae into shorter α laths during hot deformation and/or subsequent annealing. The second step is when these α laths will subsequently spheroidized and is reported to occur during thermal treatment [2–10]. Over long term annealing the material may undergo coarsening of the spheroidized α phase.

The experimental plan was setup to follow topological evolutions in the Ti-64 alloy while being processed at 950 °C, a temperature which is relevant from an industrial point of view. Microstructure was characterized just before deformation (i.e. after holding at deformation temperature to achieve phase equilibrium), after quenching right at the end of deformation, after post-deformation holding, or after subsequent thermal treatment.

One question triggered from the literature is how much does the initial size of the α lamellae actually affect the studied phenomena. In order to be able to examine this factor, our industrial partners have provided us two materials with two different microstructures with different width of α lamellae and different sizes of β grains. Both materials will be submitted to similar thermomechanical routes.

2.1.1 As received materials

The as received Ti-64 materials have two different α lamellae widths, obtained by adjusting the cooling rate after holding in the β domain, for 1h at 1050 °C. A first block was air cooled, with a cooling rate of 30 °C/min. The microstructure of this block, referred to as Lx2, has a β grain size of 0.25 -0.7 mm and an α lamellae thickness in the range 1-2 μm (see Fig. 2.1(a) and Table 2.1). A second block was slowly cooled with a rate of 2 °C/min until it reached 600 °C. The microstructure, referred to as Lx4, has a β grain size of 0.7 -1.5 mm and α lamellae thickness of 5-15 μm (see Fig. 2.1(b) and Table 2.1).

as-received microstructure	Lx2	Lx4
β grain size	0.25-0.7mm	0.7-1.5mm
lamellae thickness	1-2μm	5-15 μm

Table 2.1: Typical β grain size and lamellae thickness of the as received materials.

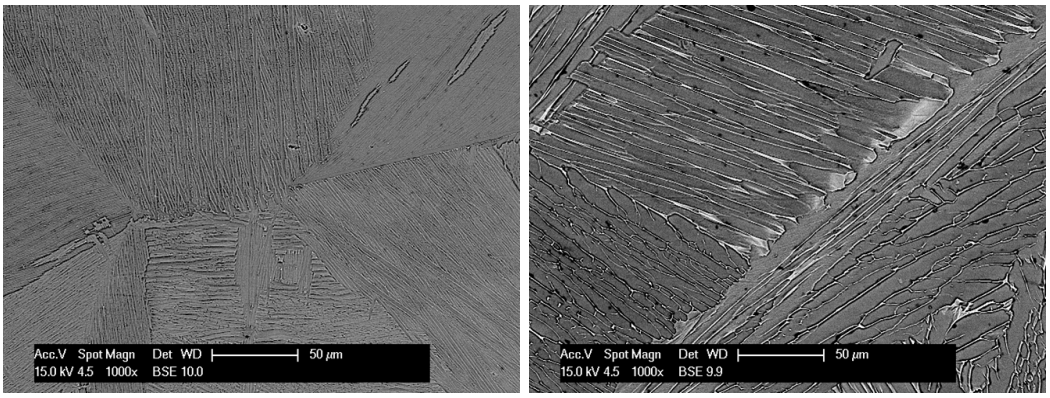

(a) Lx2 (b) Lx4

Figure 2.1: BackScattered Electron (BSE) micrographs of the two as-received microstructures: a) Lx2 and b) Lx4.

2.1.2 Geometry of the compression test samples

As already mentioned, we need to apply hot deformation and subsequent annealing in order to see spheroidization. Double cone samples were used in order to get a well-controlled strain gradient along the radius after hot-compression and directly assess the effect of the strain level within one sample. Nevertheless, unfortunately, only the microstructure at center of the samples has been analyzed in this work.

Two sample geometries have actually been used (see Fig. 2.2), in order to investigate the "low strain" range and the "high strain" range.

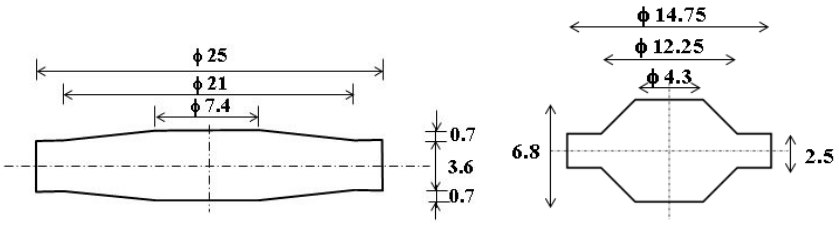

(a) low strain geometry

(b) high strain geometry

Figure 2.2: Dimensions of the double cone compression test samples used to investigate a) the low strain range (0 to 0.36 strain) and b) the high strain range (up to 1.34 strain).

In our experiments, compression is performed at 950 °C after 30 min holding and the targeted strain rate is 0.1 s^{-1}. The samples are compressed down to the cylindrical part, which allows getting a strain gradient from about 0 at the rim to 0.36 in the center for the low strain geometry, and up to 1.34 for the high strain geometry.

2.1.3 Applied thermomechanical paths

The performed thermomechanical experiments are summarized on Fig. 2.3. Some of those treatments were interrupted to characterize the current metallurgical state:

- after holding for 30 min at 950°C and quenching to assess the microstructure right before it starts being deformed (state 1 on Fig. 2.3a),
- hot compression at 950°C and 0.1 s^{-1} followed by immediate water quenching to assess the as-deformed state (state 2 on Fig. 2.3a),
- hot compression experiments followed by holding at the deformation temperature for 15 min before water quenching to assess post-dynamic microstructure evolution (state 3 on Fig. 2.3a),
- longer term annealing performed at 950°C in a conventional furnace (for optimizing the usage time of the compression machine, and avoiding damage risks for the tools) (see Fig. 2.3b).

The tests above were performed for both microstructures Lx2 and Lx4 and also for both sample geometries, low strain and high strain. The long term post-deformation annealings (see Fig. 2.3.b) have been performed only

on the high strain samples. According to Semiatin [2, 5], α laths indeed spheroidize and coarsen during prolonged annealing. The duration of annealing has been selected from the work of Semiatin and Stefanson [5, 6]. Over longer annealing the microstructural evolution reaches a plateau and it does not evolve significantly anymore.

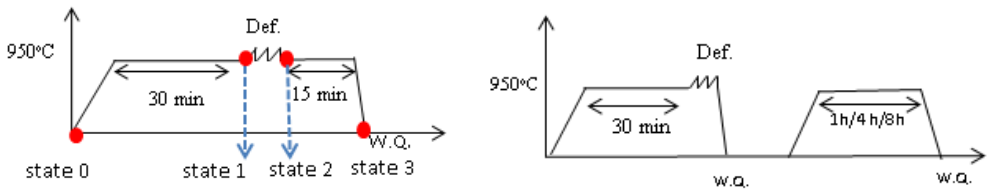

(a) (b)

Figure 2.3: Details of the performed thermomechanical experiments and interrupted tests.

Compression tests and thermal treatments have all been performed at 950°C which is in the α/β domain of the alloy. The equilibrium volume fraction of α phase at 950°C is ∼30 % [6]. Fig. 2.4 shows BSE micrographs of the microstructures Lx2 and Lx4 after 30 min holding at 950 °C and quenching. The alpha phase volume fraction measured on such images is ∼30% and ∼25% for Lx2 and Lx4 respectively which is close with the literature value of 30%. The microstructure of Fig. 2.4 will actually be the initial microstructure of which the isothermal microstructure evolutions obtained with a low strain (section 2.2) and with a high strain (section 2.3) will be described in the next sections.

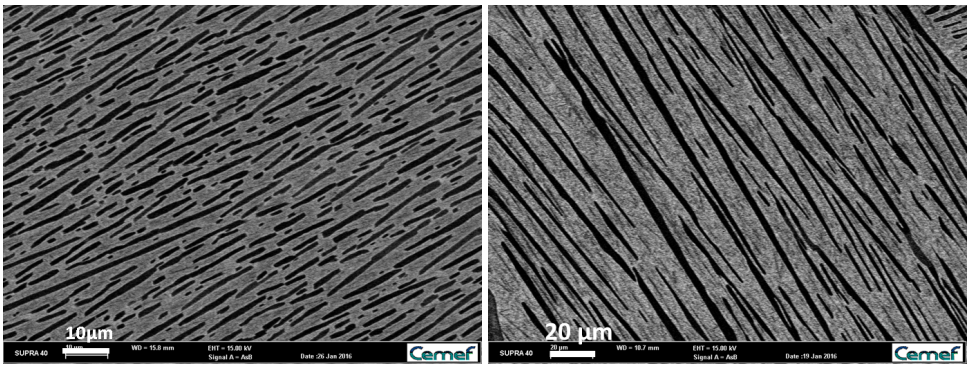

(a) "Initial state" of the Lx2 material (b) "Initial state" of the Lx4 material

Figure 2.4: BSE micrographs of the a) Lx2 and b) Lx4 materials after holding at 950°C for 30 min and water-quenching. Those are actually the initial microstructures for the hot-deformation process.

2.1.4 Sample preparation for microstructural characterization

In order to characterize microstructures, double cone samples have been cut and polished along a longitudinal section. Scanning Electron Microscopy (SEM) observations have been performed at the center of the compressed samples where the highest strain level is reached using mainly the BackScattered Electron (BSE) detector to enhance chemical contrasts and better depict α and β phases, and Electron BackScatter Diffraction (EBSD) scans. EBSD provides crystal orientation maps, which allows for detecting intragranular misorientations induced by plastic deformation. Plastic deformation indeed introduces dislocations which in turn lead to intragranular rotations of the crystal lattice. Even though a quantitative relationship is not that easy to perform, intragranular misorientations can semi-quantitatively be interpreted as the sign of the presence of dislocations. The higher the dislocation density, the higher the induced rotations.

Since quite conventional SEM and EBSD analyses have been performed, this thesis does not contain a section dedicated to the experimental protocols, but few relevant details are given here below and in the following sections dedicated to the presentation of the results.

- The local misorientations will be quantified and displayed as Kernel Average Misorientation (KAM) angle values that are available in any commercial EBSD data processing software package. The KAM value of a point is the average value of the misorientation angle between the point of interest and all its neighbors located at a given distance (i.e. Kernel radius). In this work, second or third neighbors have been considered in the calculation.

- orientation maps will be shown within a so-called IPF (Inverse Pole Figure) color coding, which shows which crystal direction is lying parallel to z axis of the sample frame.

- Image treatment of BSE micrographs will be performed with the use of ImageJ software in order to collect statistical values for α lamellae in each stage of the microstructure.

EBSD is a very demanding technique in terms of sample preparation. In order to get a suitable sample surface quality. The applied preparation procedure is the following:

- Starting with a sequence of polishing papers of $600\mu m$ for 90s, $1200\mu m$ for 90s, $2400\mu m$ for 90s applying force of $0.8daN$.

- Continuing with a sequence with powders disks of $6\mu m$ for 240s, $3\mu m$ for 240s, $1\mu m$ for 240s applying force of $0.8daN$.
- The final step is the use Oxide Polishing Suspension (OPS) for 240s applying force of $0.8daN$ in the rotative polishing machine and then changing to a vibrating machine using again OPS for 3h.
- The specimen is rinsed with water and subsequent rinse with alcohol to dry it before to proceed to SEM observations and EBSD measurements.

2.2 Microstructure evolution obtained with a strain of 0.36

2.2.1 For the Lx2 material (fine α lamellae) with a strain of 0.36

Fig. 2.5 is an EBSD map of the "initial" Lx2 microstructure already described in Fig. 2.4a, i.e. after holding 30 min of thermal treatment at 950°C. Only the points which could be indexed using the α phase structure (HCP) are shown. The α phase appears in the form of straight lamellae, that are those which were stable at 950 °C before quenching, and in the form of much finer lamellae, which arise from the $\beta \rightarrow \alpha + \beta$ phase transformation upon cooling.

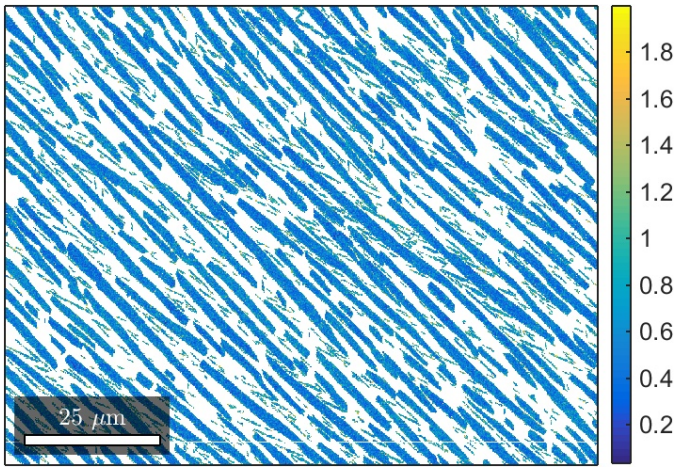

Figure 2.5: "Initial state" of the Lx2 material : KAM map after at 30 min at 950 °C.

The color-coding of Fig. 2.5 is related to local misorientation angle (KAM) between α phase neighboring points. The map exhibits blue colors corresponding to very low KAM values, in the range of 0.5°. This is actually

the accuracy with which crystal orientation can be determined using EBSD under the used setup. One can therefore consider that the dislocation content is very low in the initial microstructure, which is consistent with the thermal history of the sample. In other words, crystal orientation is uniform inside each lamella, and lamellae within a given colony have all the same crystal orientation.

After hot-compression to sample height reduction of 20% and a maximum strain of 0.36 at the sample center, orientation gradients developed inside the lamellae (as revealed by the color gradients on the IPF color coded orientation map of Fig. 2.6.a). Lamellae inside a given colony exhibit a similar but not exactly same behavior, as can be seen from the lamella to lamella color variations. Some colonies seem more deformed than others as can be appreciated from the orientation/color gradients inside them. Another important observation with regards to the mechanisms under study is the appearance of subgrain boundaries inside lamellae, visible on the KAM maps of Figs. 2.6b/c. The subboundaries are quite diffuse (thick) and have low local misorientation angles, typically 1-2 °(green-yellowish colors on Fig. 2.6b/c), but cumulated misorientation angles through the thick subboundaries which can reach up to 10 °(see the jumps on the profiles of Fig. 2.7).

Plots of misorientation profiles along lamellae chosen from the KAM map of Fig. 2.6b are shown in Fig. 2.7. Misorientation profiles are plots showing the cumulative misorientation in respect to the first point of the drawn lines. Line AB (Fig. 2.7a) and Line CD (Fig. 2.7b) indeed show that fairly large misorientations developed between the starting and ending points.

Some lamellae do even start to fragment, already at this relatively low strain level (examples arrowed on Fig. 2.6c). Nevertheless, the fragmentation process is quite heterogeneous from one colony to another. The orientation of the colonies with respect with the direction of the applied deformation, seem to be a very important factor for the fragmentation of the α lamellae (Fig. 2.6c compared to Fig. 2.6b), as reported already in the literature [3–5, 7].

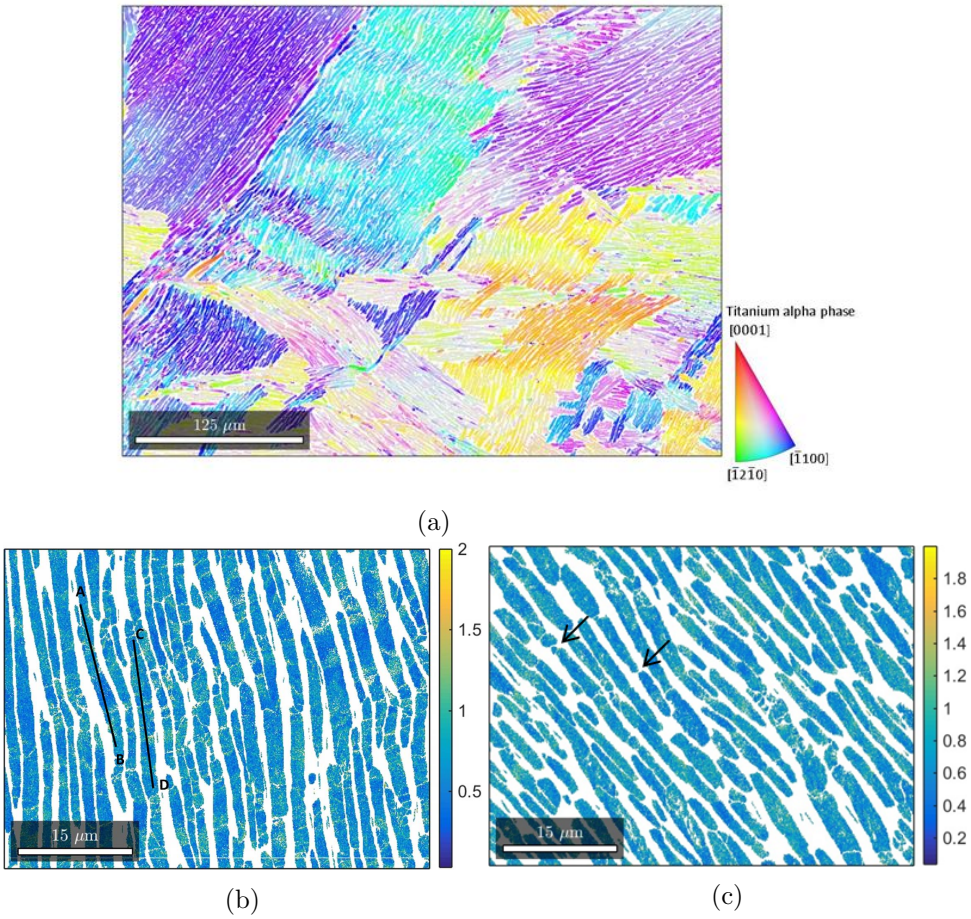

Figure 2.6: a) Crystal orientation map of the Lx2 material after hot-deformation to 0.36 strain. The color coding indicates which crystal direction is parallel to the direction normal to the map (z). b) and c) are KAM maps of zoomed colonies differently oriented in relation with the compression axis. The compression axis is vertical (↓).

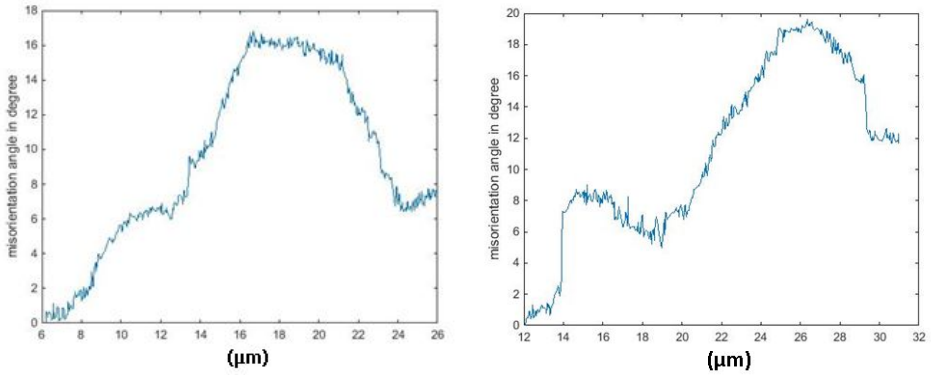

(a) (b)

Figure 2.7: a) Misorientation profiles of line segment AB drawn on Fig. 2.6b and b) misorientation profiles of line segment CD.

After the material was held for 15 min at 950°C after deformation, a significant microstructure change is observed (see Fig. 2.8) as compared to the case where it was quenched immediately after deformation (see Fig. 2.6). The orientation map of Fig. 2.8a shows that fragmentation of the lamellae has quite significantly progressed during the post-deformation holding. The fact that the microstructure is more fragmented after only 15 minutes annealing is fully consistent with the conclusions drawn in literature that misorientations and subboundaries developed inside the α lamellae during deformation subsequently form grooves during annealing and lead to lamella splitting into shorter laths.

Furthermore, Fig. 2.8 confirms the importance of the lamellae orientation with regards to the compression axis. Kinking of the lamellae parallel to the compression axis is visible on Figs. 2.8a/b. Fragmentation seems to be more advanced within the kink regions.

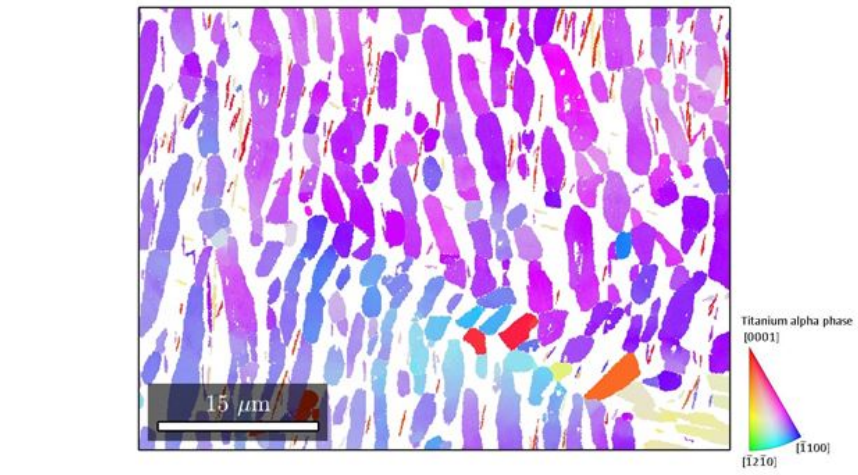

(a)

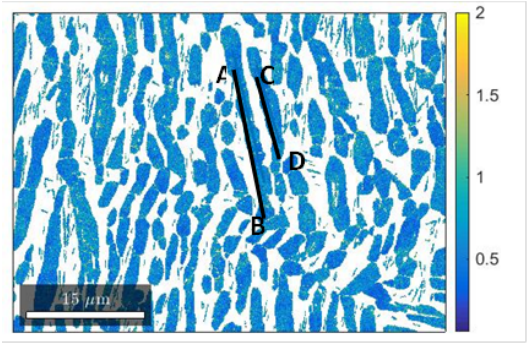

(b)

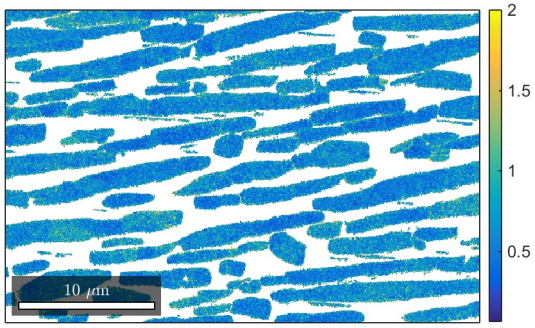

(c)

Figure 2.8: a) Crystal orientation map of the Lx2 material after hot-deformation to 0.36 strain and holding for 15 min before quenching. The color coding indicates which crystal direction is parallel to the direction normal to the map (z). Compression axis is vertical(↓). b) and c) are KAM maps of zoomed colonies with different orientation to the compression axis.

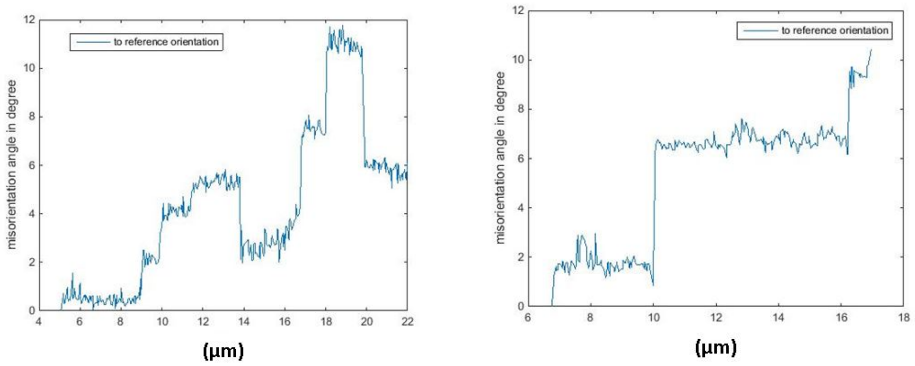

(a) (b)

Figure 2.9: a) Misorientation profiles of line segment AB drawn on Fig. 2.8b and b) misorientation profiles of line segment CD.

The misorientation profiles of segments AB and CD drawn on Fig. 2.8.b are shown on Figs. 2.9a and b, respectively. The jumps in the profiles, indicative for the presence of subboundaries along the lamellae, are of similar amplitude but much steeper than they were in the deformed and quenched material. This clearly proves that subboundaries re-organized during the post-deformation holding time. They became real subboundaries, whereas they were more like thick transition zones after deformation. These subboundaries delimit subgrains, which may subsequently separate from each other during the fragmentation process.

Globally and qualitatively, it can be seen from Figs. 2.8 and 2.10 that fragmentation of the α lamellae starts already during deformation and the shape keeps evolving towards a more circular form but without any big change in the length of the laths. For the purpose of quantifying the changes in the lamellae shape during annealing after deformation, BSE micrographs like those of Fig. 2.10 have been analyzed.

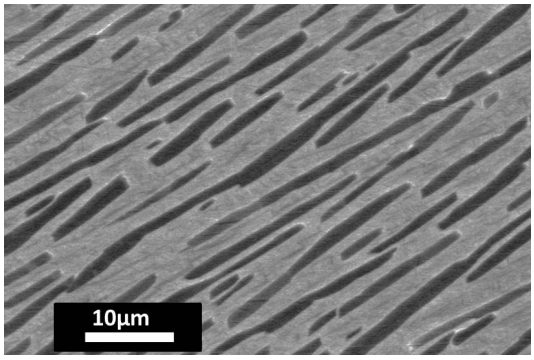

(a)

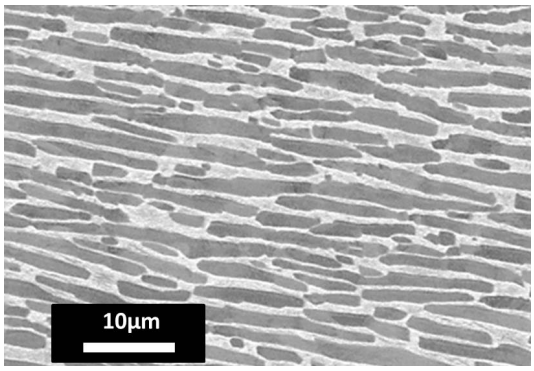

(b)

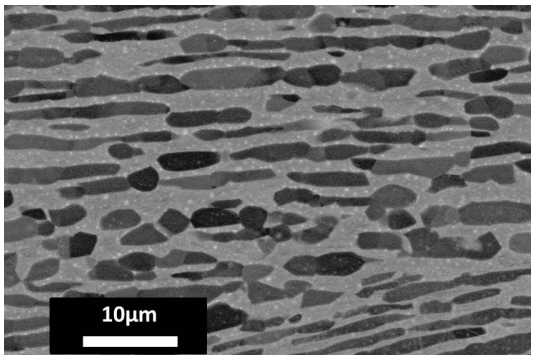

(c)

Figure 2.10: Typical BSE micrographs of the Lx2 material, in its a) initial state after 30 min of annealing at 950 °C, b) deformed state ($\epsilon = 0.36$), c) deformed and annealed (15 min) state, used for quantifying the shape evolution of the α lamellae.

A total number of about 700 laths have been analyzed in each state, by processing BSE images with the ImageJ software package. With ImageJ, the lath shapes could be approximated by ellipsoids whose length and width can then be measured. To describe the shape evolution, the lath/ellipsoid

aspect ratio, that is a dimensionless number, will be used:

$$\text{aspect ratio} = \frac{\text{major axis of ellipsoid}}{\text{minor axis of the ellipsoid}}. \tag{2.1}$$

The closer the aspect ratio goes to 1 the more circular is the shape.

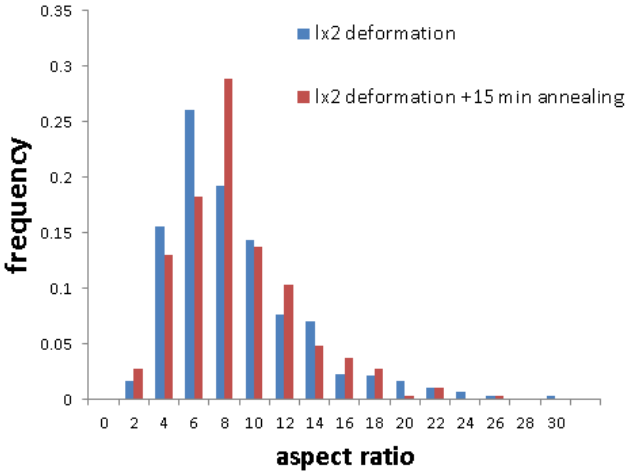

Figure 2.11: α lath aspect ratio histograms of the Lx2 material in its deformed state (blue),deformed and annealed state (15 min at 950°C)(red).

The aspect ratio histograms of the deformed state and of the deformed and annealed state (Fig. 2.11) keep being very similar. The mean values of the aspect ratio are close, 7.76 for the deformed state and 7.84 for the deformed and annealed state. The fragmentation process is likely to not be advanced enough yet to give meaningful results through the performed analysis. The small progression of the fragmentation obtained after 15 min annealing is consistent with what has been reported by Semiatin and Stefanson [5,6]. A short annealing time of 15 min was probably not enough to get significant fragmentation. Another possible explanation is the applied strain being too small. Other experiments will thus be described later on (section 2.3) where higher strain and longer annealing times were applied.

2.2.2 For the Lx4 material (thick α lamellae) with a strain of 0.36

In order to investigate the effect of the lamella thickness onto the onset of fragmentation mechanisms, the same experiments presented in the previous section for the Lx2 material have been conducted on the Lx4 material.

The initial state (after holding at 950°C for 30 min and quenching) is shown on Fig. 2.12, the deformed state on Fig. 2.13, and the deformed and annealed state (15 min post-deformation holding) on Fig. 2.15.

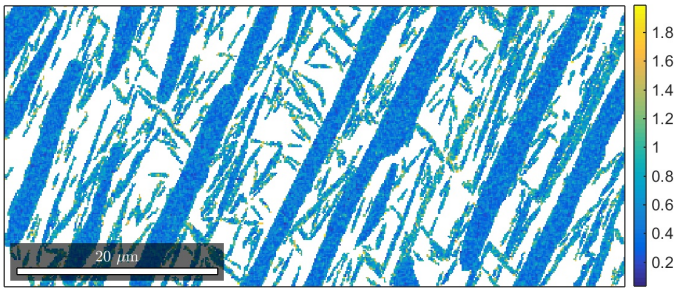

Figure 2.12: KAM map of the Lx4 material after at 30 min at 950 °C and quenching.

Regarding the initial state of Lx4 obtained after 30 min thermal treatment at 950 °C (Fig. 2.12) the same comments can be made as for the Lx2 material : lamellae are long and straight, and do not exhibit internal misorientations. The only difference is the lamella thickness (around 5-15 μm for Lx4 and around 1-2μm for Lx2).

The deformed Lx4 microstructure (Fig. 2.13) does not seem to be so affected by deformation as was the Lx2 material at the same strain level, but from KAM maps we can see that slight intra-lamellar misorientations have developed and this goes along with the appearance of diffuse subboundaries which start forming.

The misorientation profiles along AB and CD segments (drawn on Fig. 2.13a) of lamellae in the deformed state (plotted on Fig. 2.14a/b) have much lower amplitudes than the ones of the deformed state of Lx2 (see Fig. 2.7). Those profiles exhibit more regular orientation gradients, with jumps in the range of 2-3°at maximum (against up to 10°in the thin lamellae of Lx2).

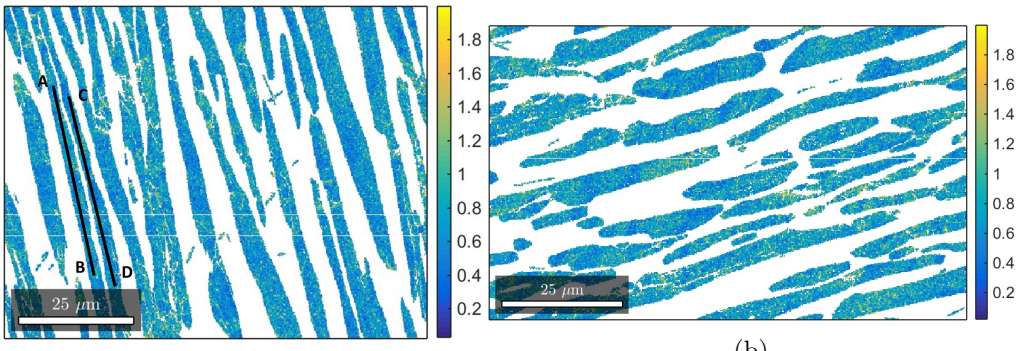

(a) (b)

Figure 2.13: KAM maps of the Lx4 material after hot-deformation to 0.36 strain: a) in a colony almost parallel to the compression axis and b) in a colony almost perpendicular to the compression axis.

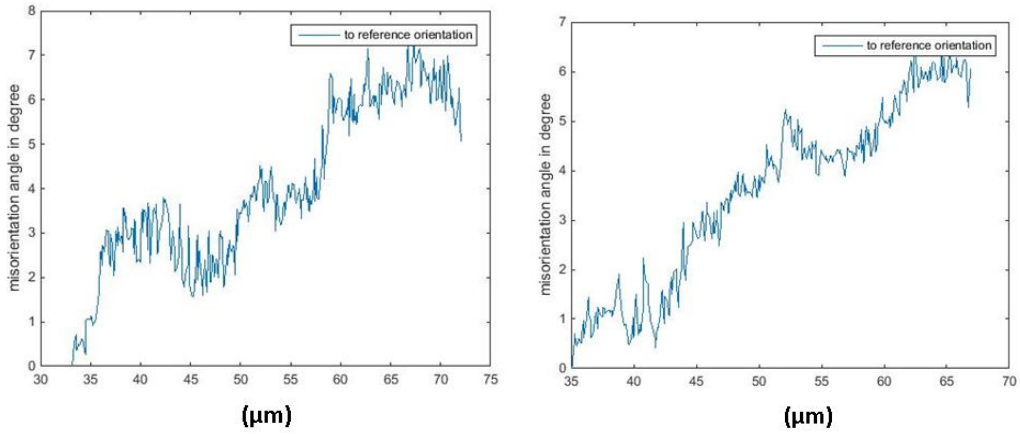

(a) (b)

Figure 2.14: Misorientation profiles along: a) segment AB and b) segment CD.

After post-deformation holding for 15 min, the Lx4 microstructure still exhibits misorientations inside the α lamellae, but on a first sight there is no microstructure change over post-deformation holding (Fig. 2.15 compared to 2.13). Apparently the 15 min of annealing is not enough time to see a significant evolution of those initially thick lamellae which developed only few degrees misorientations.

It is worth mentioning that some of the misorientation profiles, like the one plotted on Fig. 2.16a for lamellae after 15 min post-deformation annealing show steep orientation changes with an increased amplitude (8-10°) compared to the deformed Lx4 state (Fig. 2.14). A possible explanation is that recovery was active enough during post-deformation holding, so that the stored dislocations responsible for the continuous orientation gradients could migrate and gather into thin walls, i.e. well defined subboundaries.

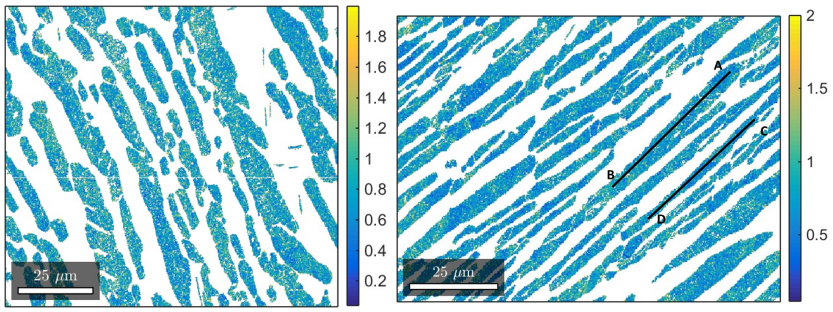

(a) (b)

Figure 2.15: KAM maps of the Lx4 material after hot-deformation to 0.36 strain and subsequent holding for 15 min at 950°C.

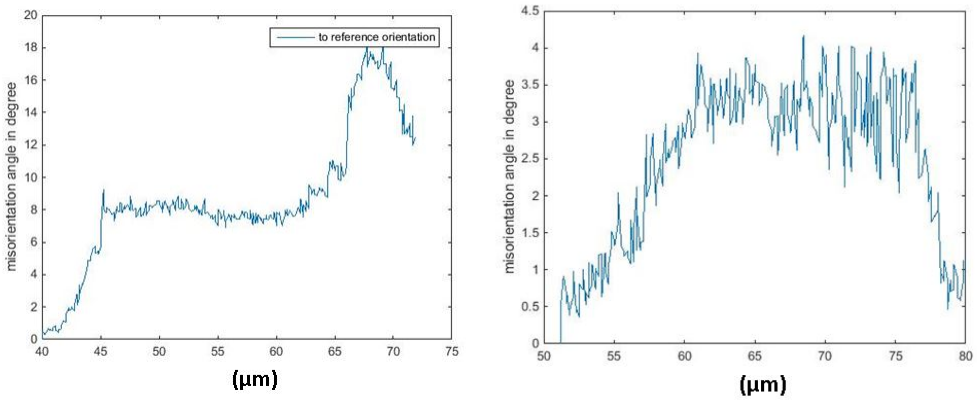

(a) (b)

Figure 2.16: Misorientation profiles along segments: a) AB and b) CD drawn on Fig. 2.15b.

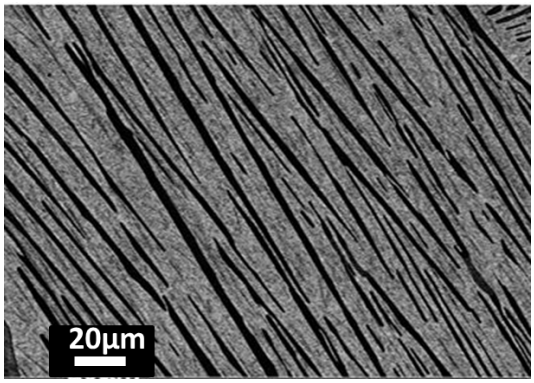

(a)

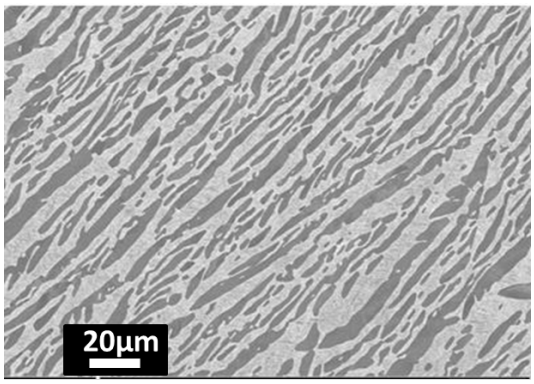

(b)

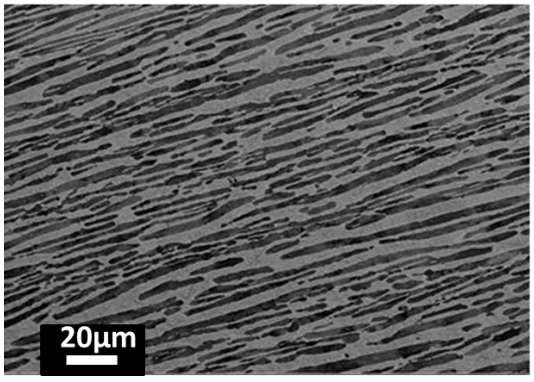

(c)

Figure 2.17: Typical BSE micrographs of the Lx4 material, in its a) initial state, b) deformed state, c) deformed and annealed (15 min) state, used for quantifying the shape evolution of the α lamellae.

BSE image analysis lead for the Lx4 material to the aspect ratio distributions of Fig. 2.18 (gathering the data of about 750 lamellae for each state, collected on images like those Fig. 2.17). Between the deformed stage and the deformed and annealed for 15 min stage the difference between both

distributions is not really significant. The mean value of aspect ratio for the deformed state is 8.74 and for the annealed state 8.40. No conclusion can be drawn from those analyses yet.

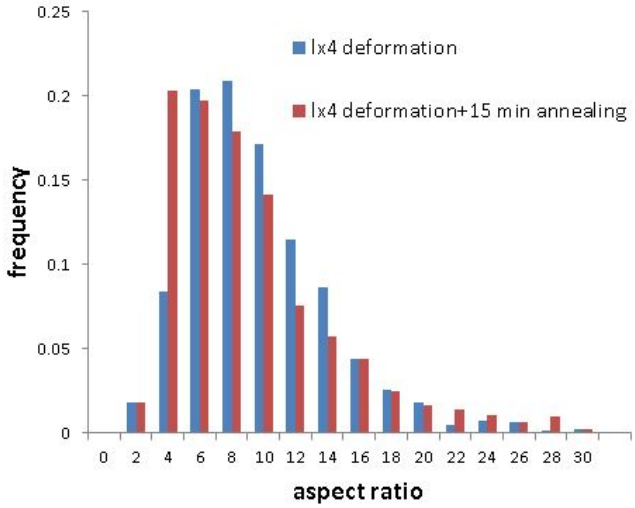

Figure 2.18: α lath aspect ratio histograms of the Lx4 material in its deformed state (blue) and deformed and annealed state (15 min at 950°C)(red).

2.2.3 Comparison of the Lx2 and Lx4 materials submitted to a strain of 0.36

The two materials at both deformed and deformed-and-annealed states with the same applied deformation conditions (up to 0.36 at 950°C and $0.1s^{-1}$) basically leads to the same conclusions. During deformation, misorientations and subboundaries start developing inside the α lamellae. subboundaries appear as diffuse orientation change areas after deformation and become better defined subboundaries during holding after deformation. The areas with higher misorientations (onset of subboundary formation) are the ones that are most likely to form grooves and subsequently lead to the lamella splitting. The misorientations developed in the fine lamellae are stronger (up to 10°) than in the coarse ones (only few degrees). This is basically the only difference that could be observed between both materials. With a post-deformation holding of 15 min at 950 °C, quite limited microstructure evolution occurs both in the fine and coarse lamellae materials. Basically, only the subboundaries become better depicted. The mean aspect ratio of the α lamellae/laths (obtained from BSE image analysis) follows very similar trends for both Lx2 and Lx4 materials (see Fig. 2.19). Deformation strongly affects the shape of the lamellae/laths as compared to the initial state, but the post-deformation holding has almost no influence.

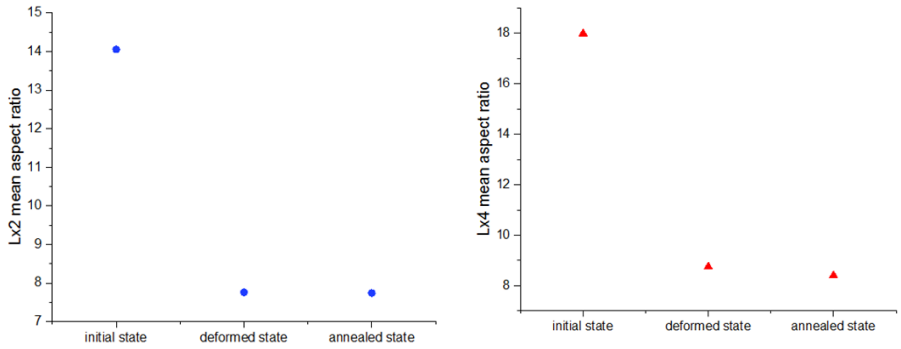

(a) (b)

Figure 2.19: Mean value of the α lamella/lath aspect ratio of a) the Lx2 and b) Lx4 materials in their initial state, deformed state and deformed and annealed state (15 min at 950°C).

As the Lx2 and Lx4 materials led to the same observations, the lamella thickness does not seem to have any significant influence on the overall evolution with regards to the fragmentation process, under the applied thermo-mechanical conditions. On the other hand, the orientation of the lamellae with regards to the compression axis appeared to strongly affect the lamella shape after deformation, and this hold for both materials. The lamella which are initially lying parallel to the compression axis undergo kinking, and this helps further fragmentation mechanisms (subboundary formation, grooving and finally splitting). Striking examples of lamellae kinking in both materials are shown in Fig. 2.20. These micrographs have been taken at the center of the deformed samples, and are very similar to some reported in the literature [2–4].

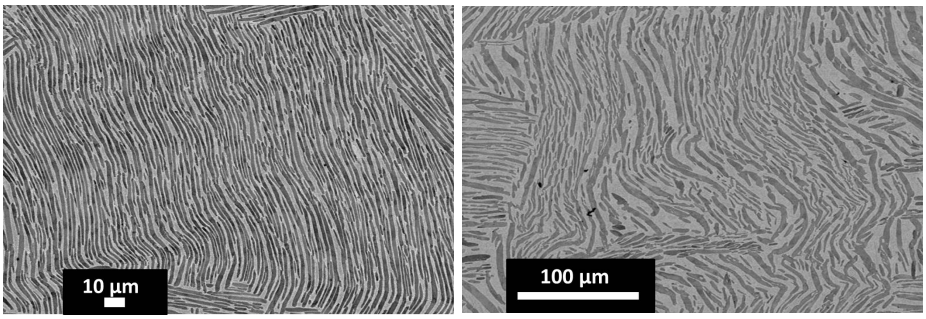

(a) (b)

Figure 2.20: Lamella kinking observed at the center of a) Lx2 and b) Lx4 samples after hot-compression, in areas where lamellae were obviously initially parallel to the compression axis. The compression axis is vertical.

The strain level will be increased in the following section, in order to induce more significant microstructure changes, and more advanced fragmentation states.

2.3 Microstructure evolution obtained with a strain of 1.34

With the double cone geometry of Fig. 2.2.b, a strain level of 1.34 can be reached at the center of the sample. In this section, the same as-received materials (Lx2 and Lx4) as in the previous section will be used and submitted to the high strain compression experiments. In addition to the strain level, the duration of the post-deformation annealings will be increased as well to promote spheroidization of α lamellae.

2.3.1 For the Lx2 material (thin α lamellae) with a strain of 1.34

Fig. 2.21a shows an orientation map of Lx2 microstructure after hot compression with sample height reduction 63 % and the maximum strain of 1.34 at the sample center. The deformed microstructure is much more fragmented than that of Lx2 after 0.36 strain (see Fig. 2.6). The map of Fig. 2.21a covers a wide area with different orientations of α colonies. In the lower half of the area, the microstructure is very fragmented and there are no more signs of the previous elongated laths. On the other hand, in the upper area of the map not obvious fragmentation is observed but orientation gradients are developed inside the α lamellae (indicated by the variation of colors). This map is one more clear proof that all colonies do not exhibit the same behavior under deformation.

In addition, on the following KAM map (Fig. 2.21b) very clear subboundaries are observed inside the remaining elongated laths. For better observations, Fig. 2.21b shows the KAM map of the zoomed area inside the rectangle of Fig. 2.21a. For complementary information, further data analysis regarding the subboundaries on this specific map has been done with MTEX toolbox (EBSD data post-processing software). On Fig. 2.21c, again the zoomed area inside the rectangle, the α lamellae boundaries are defined with a threshold angle of 10°are plotted black. At the same image the magenta color depicts the 2°to 3°angle subboundaries and the green color depicts the 3°to 4°angle subboundaries. From the combination of these two Figs. 2.21b/c, it is shown that smaller laths are already schematized. At the same time, well defined internal subboundaries appear inside the remaining lamellae.

On Fig. 2.22 plots of misorientation profiles inside laths of the KAM map of Fig. 2.21b are shown. Both given plots are representative, since these two

are not the only lamella/lath measured. By comparing the misorientation profiles inside elongated lamellae and smaller α laths, it is observed that the longest one exhibits higher misorientations.

From the information above, it is obvious that the fragmentation process is initiated during deformation at high strains. There are α colonies that are already very fragmented and others which are still very elongated but include subboundaries. These observations are in agreement with what is reported in the literature: during deformation, due to crystal plasticity, subboundaries appear and are the main reason for the subsequent splitting of lamellae.

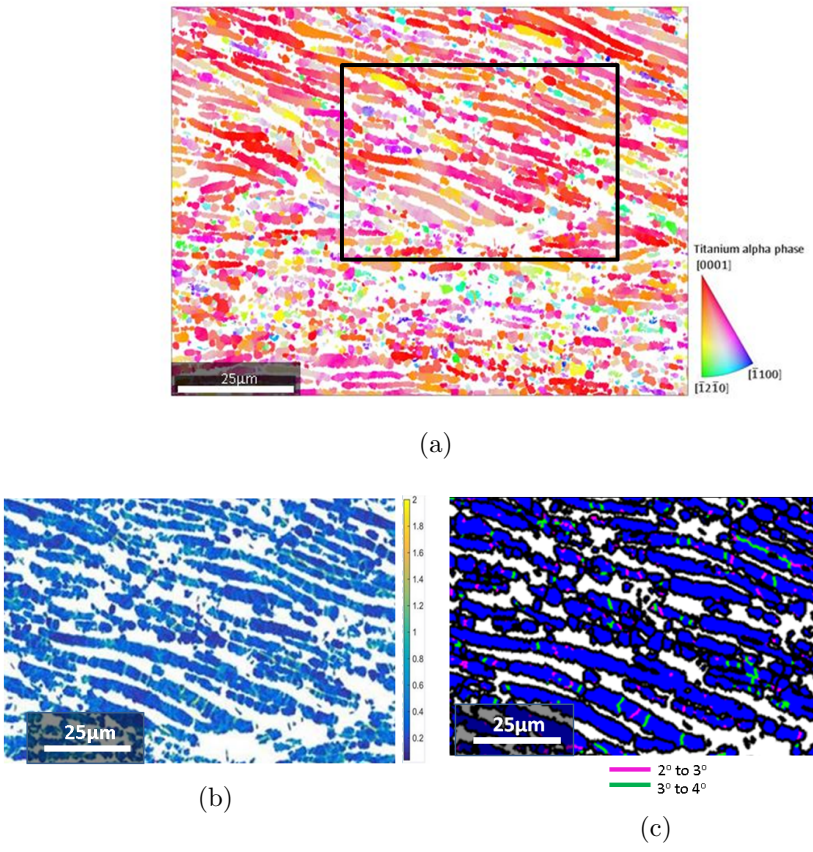

Figure 2.21: a) IPF map of Lx2 material after hot deformation to 1.34 strain at 950°C. The color coding indicates which crystal direction is parallel to z axis. b) KAM map of the area in the rectangle a), c) boundaries plotted black and subboundaries plotted pink (2°- 3°) and green (3°- 4°) in the rectangle area drawn on a).

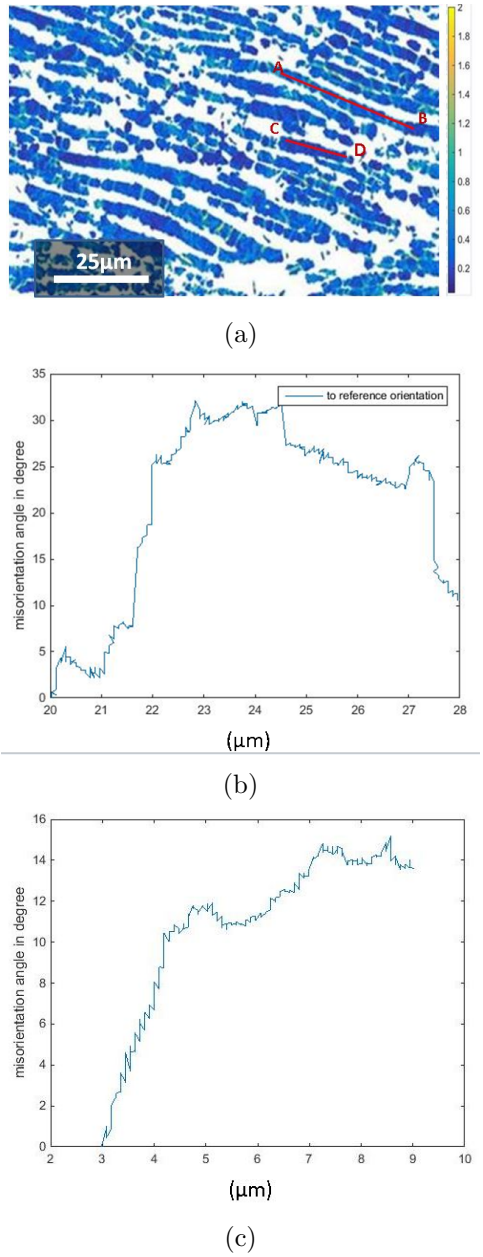

(a)

(b)

(c)

Figure 2.22: Misorientation profiles of segments: a)AB and b)CD.

Fig. 2.23 shows an EBSD map of Lx2 microstructure after hot compresion at 1.34 strain and post-deformation annealing for 15 min at 950 °C. The shape evolution towards smaller α laths is clearly visible after only 15 min of annealing. On Fig. 2.23a an IPF map is presented where the α laths are smaller and exhibit a more spheroidized shape. Each lath also has a uniform color which indicates a uniform crystal orientation. No subbound-

aries are left inside the laths. The KAM map on Fig. 2.23b confirms that no significant internal misorientation exist inside the smaller and circular α laths.

Fig. 2.23c is another representation of the microstructure, using the same interface color coding as in Fig. 2.21c. Comparing Fig. 2.23c with 2.21c, only few subboundaries still appear, which confirms that the lamellae splitting has already progressed a lot in certain colonies and new well defined and shorter α laths have already been formed after only 15 min of annealing.

The 1.34 strained Lx2 microstucture after 15 min post-deformation holding is very different to the Lx2 microstructure after the same post deformation holding time (15 min) but lower strain 0.36 (see Fig. 2.8). The higher the strain the more subboundaries appear inside the α lamellae, which leads to a faster evolution during annealing.

The lath formation in Fig. 2.23 only occurs in some colonies in the area of maximum strain of the sample. In the same area, other colonies have also been observed with not much shape evolution. This confirms the assumption that the colony orientation with respect to the orientation of applied deformation plays a very important for how quick spheroidization will occur.

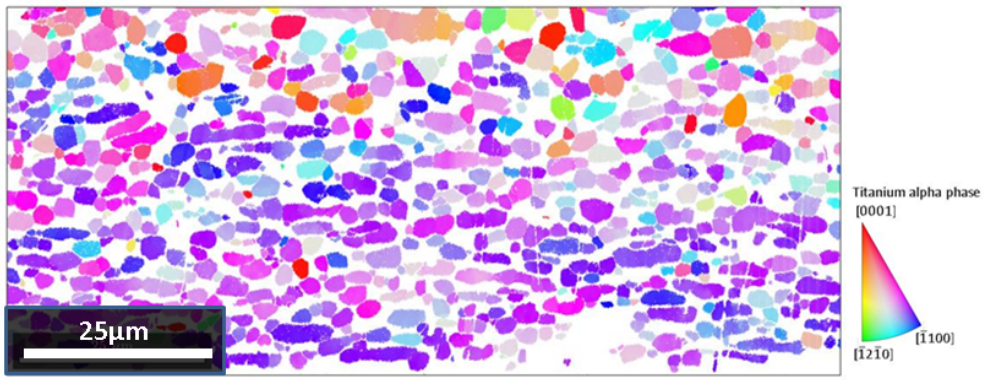

(a)

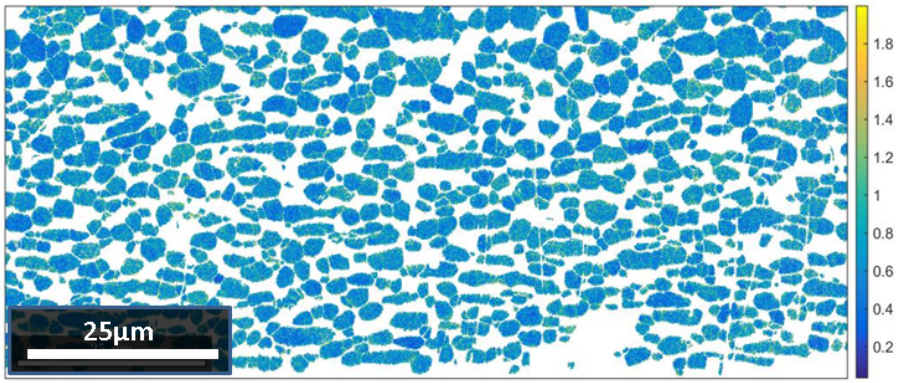

(b)

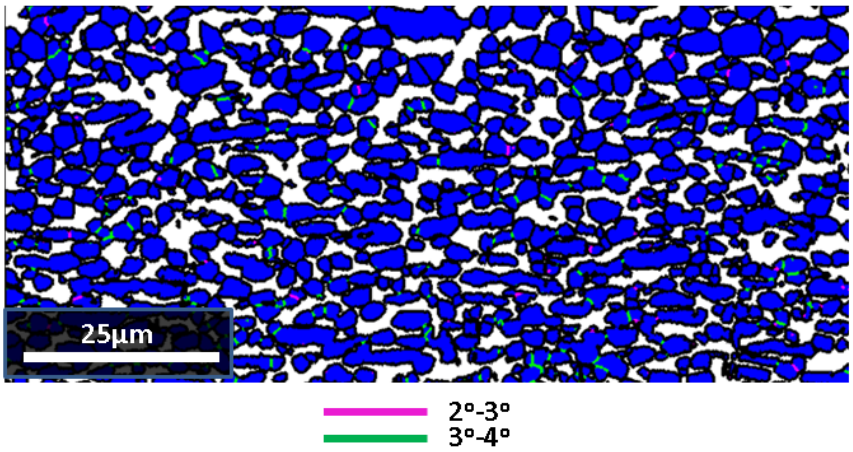

(c)

Figure 2.23: a) IPF map of Lx2 material after hot deformation to 1.34 strain and 15 min holding at 950 °C. The color coding indicates which crystal direction is parallel to z axis, b) KAM map and c) boundaries plotted black and subboundaries plotted pink (2°- 3°) and green (3°- 4°).

Figs. 2.24a and 2.24b show the Lx2 microstructure hot deformed to the same strain of 1.34 but submitted to a longer subsequent annealing, for 1h. The relatively wide field BSE image of Fig. 2.24 shows that the microstructure became homogeneous, the initial colonies can hardly be recognized anylonger. Furthermore, the KAM map on Fig. 2.24b shows that α particles have homogeneous orientation. The center of the sample, strained to 1.34 shows thus the expected microstructural evolution towards a more globular and coarser shape.

Other areas of the same sample, where the strain level was lower have been also observed. Two of such areas are shown in Figs. 2.24c and 2.24d. In those ones, the initial colonies and the initial grains can still be recognized, both because the fragmentation progressed to different levels, and because the orientations keep some link to initial colony orientation. In addition to the initial orientation of the lamellae with regards to the compression direction, the crystallographic orientation could also possibly be a reason for a different evolution of each colony. Actually the morphological orientation of the initial lamellae can not be unambiguously determined from 2D sections, 3D microscopy would be usefull to really comprehend the phenomenon of spheroidization of α lamellae and its mechanisms.

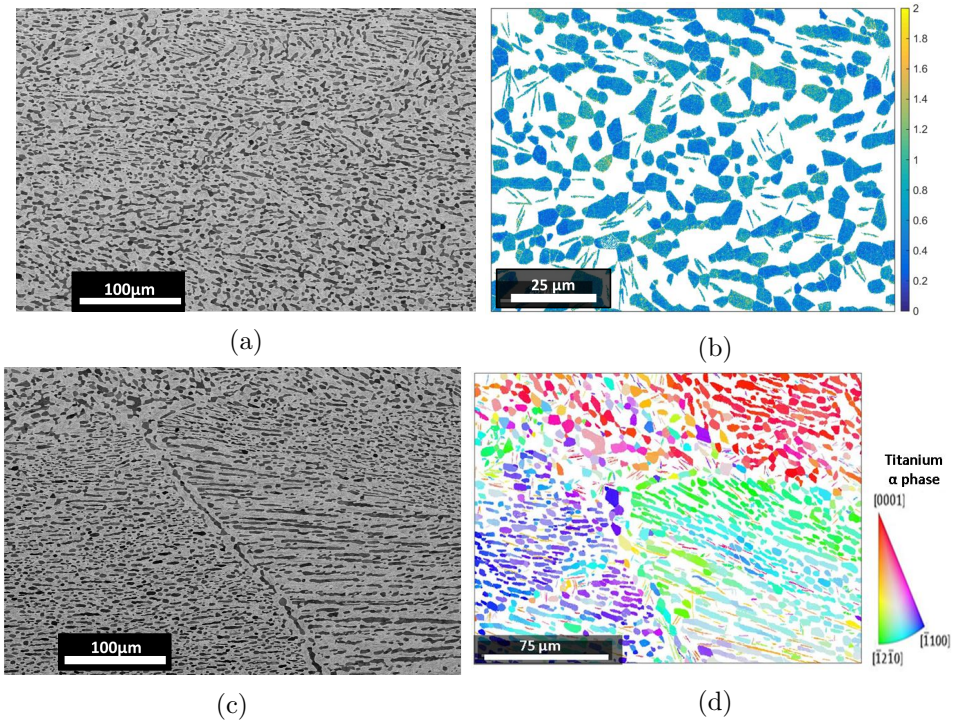

Figure 2.24: Lx2 material after hot deformation and 1 h holding at 950 °C. a) BSE micrograph and b) KAM map the center of the sample with 1.34 strain. c) BSE micrograph and d) IPF map in a lower strain area of the same sample. The color coding indicates which crystal direction is parallel to z axis.

Next, the Lx2 material submitted to hot-compression, immediate water quenching and subsequently reheated for 4h and 8h annealing at 950 °C in a separate furnace are presented, on Figs. 2.25 and 2.26, respectively. A clear image at the exact center of the sample with the maximum strain was not possible for sample with 4h annealing, so Fig. 2.26 shows EBSD maps from lower strain areas of that sample. α phase coarsened significantly during those long term annealings, as compared to the previously described samples. α phase keeps coarsening between 4h and 8h annealing. This meets up with the expectations given from literature for coarsening of the microstructure during prolonged annealing. Furthermore, in the EBSD map of Fig. 2.25.b from the material annealed for 4h, there are groups of α laths with the same orientation. This leads to the assumption that given a starting colony breaks up to smaller laths that they keep some orientation relationship with the mother colony. Further analyses regarding the quantification of the microstructural evolution will be made in sections 2.4 and 2.5.

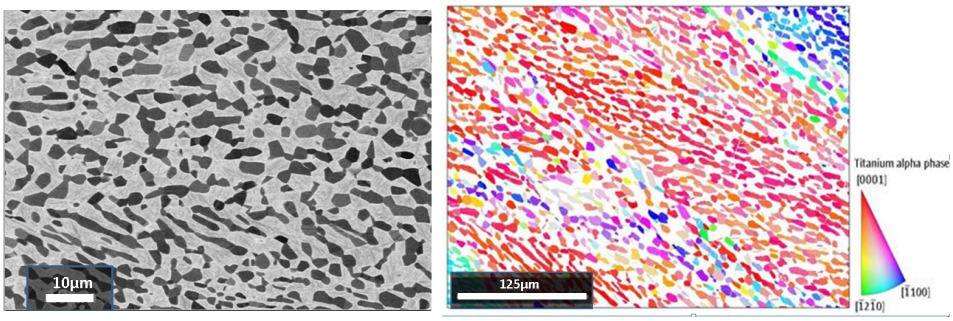

(a) (b)

Figure 2.25: Lx2 material after hot deformation at strain 1.34 and 4h holding at 950°C: a) BSE micrograph and b) IPF map at lower strain area of the sample. The color coding indicates which crystal direction is parallel to z axis.

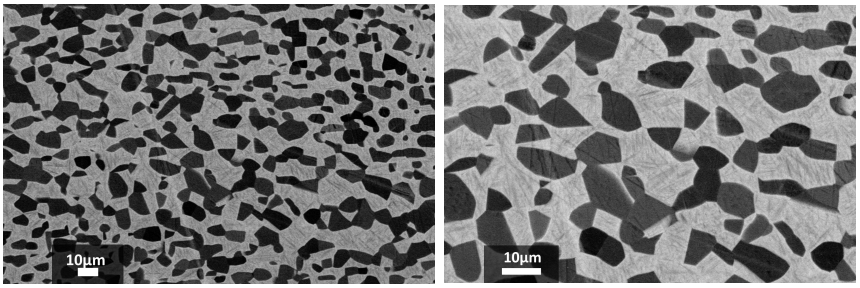

(a) (b)

Figure 2.26: BSE micrographs of Lx2 material after hot deformation at strain 1.34 and 8 h holding at 950 °C.

2.3.2 For the Lx4 material (coarse α lamellae) with a strain of 1.34

In this section, results regarding the Lx4 material after deformation and subsequent annealing are presented following the same sequence as presented for Lx2 in the previous section.

BSE micrographs and EBSD maps of Lx4 after hot compression to 1.34 strain at 950 °C are presented on Fig. 2.27. The microstructure does not seem to be highly fragmented and no obvious shape evolution is observed, except for the kinked areas. On Fig. 2.27c the orientation map shows color variations inside lamellae which indicate orientation gradients developed during deformation. In addition, the KAM map of Fig. 2.27d reveals the existence of areas with higher misorientations along the α lamellae. It is also interesting to note that some of the lamellae came into contact but did not merge. Instead, they formed a subboundary/interface between them.

Possibly related to the large width of the lamellae, many colonies with lamellae kinking were found in this sample. Let's remind here that lamellae kinking was reported in the literature [3] as one of the mechanisms that promotes fragmentation of the α lamellae. Figs. 2.27e/f show orientation and KAM maps of kinked but not yet fragmented lamellae. On Fig. 2.27f, we observe high misorientations inside the lamellae especially at the kinked areas.

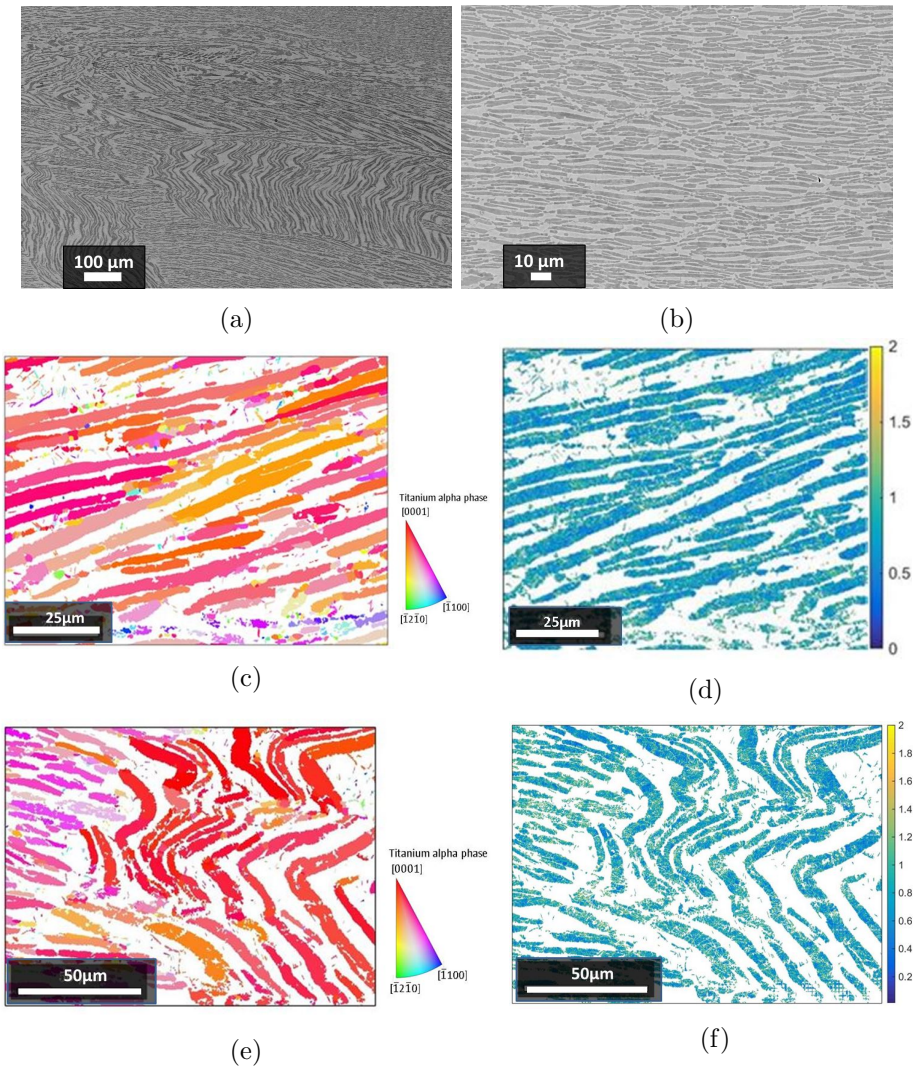

Figure 2.27: Lx4 material after hot deformation at strain 1.34 at 950°C: a)b) BSE micrographs, c)d) IPF map and KAM map of lamellae which did not bend during deformation, e)f) IPF map and KAM map of kinked lamellae. The IPF color coding indicates which crystal direction is parallel to z axis.

Lx4 microstructure under hot compression to 1.34 and subsequent 15

min holding at 950°C has significantly changed in comparison with previous state, fragmentation onset is observed. Fig. 2.28 shows that fragmentation occurred but the laths are still elongated with no subsequent spheroidization for the moment. Complementary the KAM map on Fig. 2.28b does not show a lot of misorientation inside the formed laths.

Over longer term annealing (see Figs. 2.29, 2.30, 2.31 for 1h, 4h and 8h post-deformation annealings, respectively), globularisation progresses and coarsening occurs, as already observed in samples Lx2. With the Lx4 material, globularization has only started after 15 min holding (Fig. 2.28), contrary to Lx2 where it was more advanced. After 1h annealing (Fig. 2.29), fragmentation is more advanced, but also elongated laths remain. Starting from 4h annealing, well defined gobularized and coarsened particles, some of them in touch with each other, are formed (Fig. 2.30). Longer term annealing of 8h just leads to slight further coarsening (Fig. 2.31).

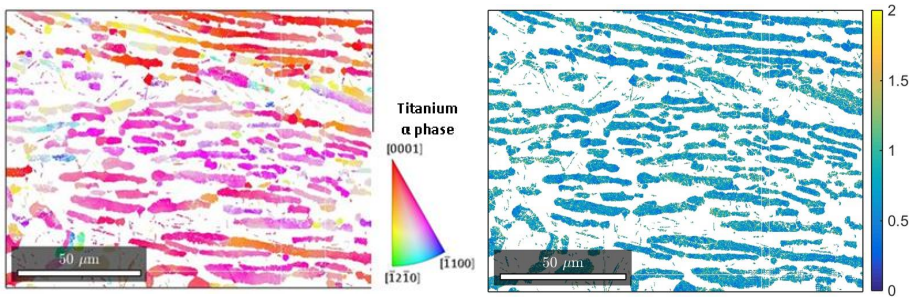

(a) (b)

Figure 2.28: Lx4 material after hot deformation at strain 1.34 and holding for 15 min at 950°C: a) IPF map. The color coding indicates which crystal direction is parallel to z axis and b) KAM map.

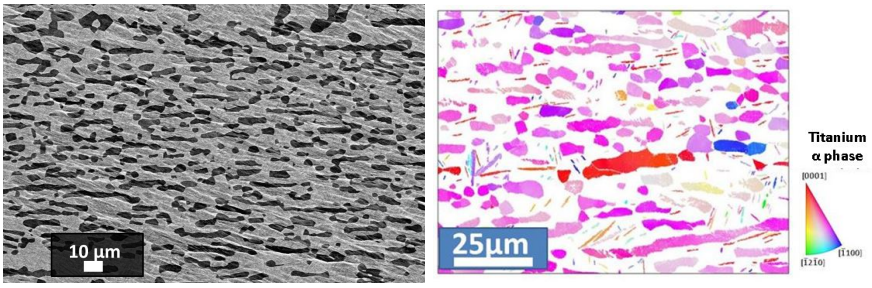

(a) (b)

Figure 2.29: Lx4 material after hot deformation at strain 1.34, immediate water quenching and subsequent 1 h annealing at 950°C: a) BSE micrograph and b) IPF map. The color coding indicates which crystal direction is parallel to z axis.

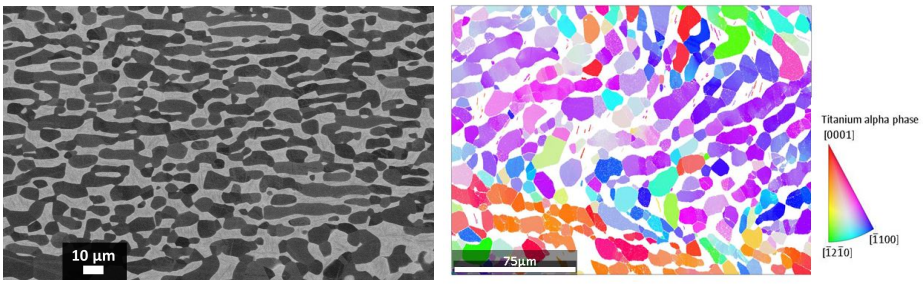

(a) (b)

Figure 2.30: Lx4 material after hot deformation at strain 1.34, immediate water quenching and subsequent 4 h annealing at 950°C: a) BSE micrograph and b) IPF map. The color coding indicates which crystal direction is parallel to z axis.

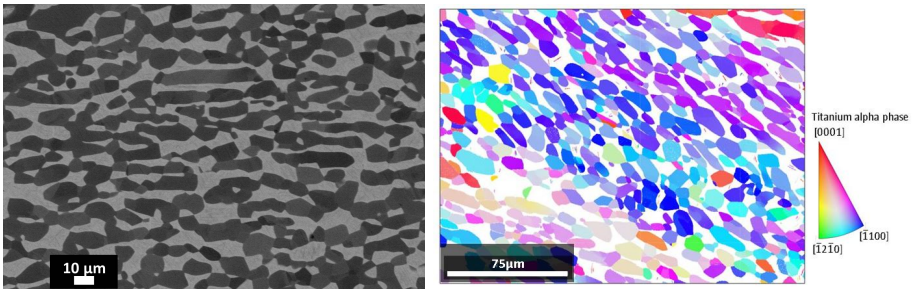

(a) (b)

Figure 2.31: Lx4 material after hot deformation at strain 1.34, immediate water quenching and subsequent 8 h annealing at 950°C: a) BSE micrograph and b) IPF map. The color coding indicates which crystal direction is parallel to z axis.

Lx4 after deformation at 1.34 strain follows the same behavior as Lx2 at the same state. After deformation the microstructure exhibits significant misorientations inside α lamellae but no real fragmentation yet. Shape evolution and then coarsening occurs mainly during the post-deformation holding or annealing. The main difference between both materials is that Lx4 microstructure with post-deformation 15 min annealing does not tend to the spheroidized microstructure as observed in Lx2 material at the same state (Fig. 2.23). Lx4 has coarser lamellae which may not facilitate the formation of subboundaries inside the lamellae, even at the relatively high strain level of 1.34.

The difference in the behavior of Lx4 compared to Lx2 materials can be globally appreciated on the low magnification BSE micrographs of Fig. 2.32. Those images are taken at the center of the compressed double cone samples,

but at a magnification low enough that the effect of strain gradients can be appreciated as well.

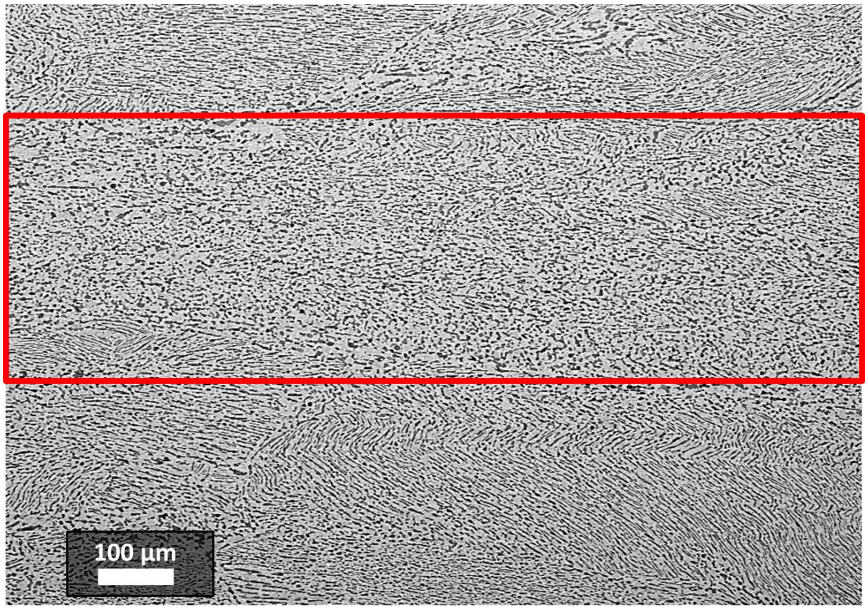

(a)

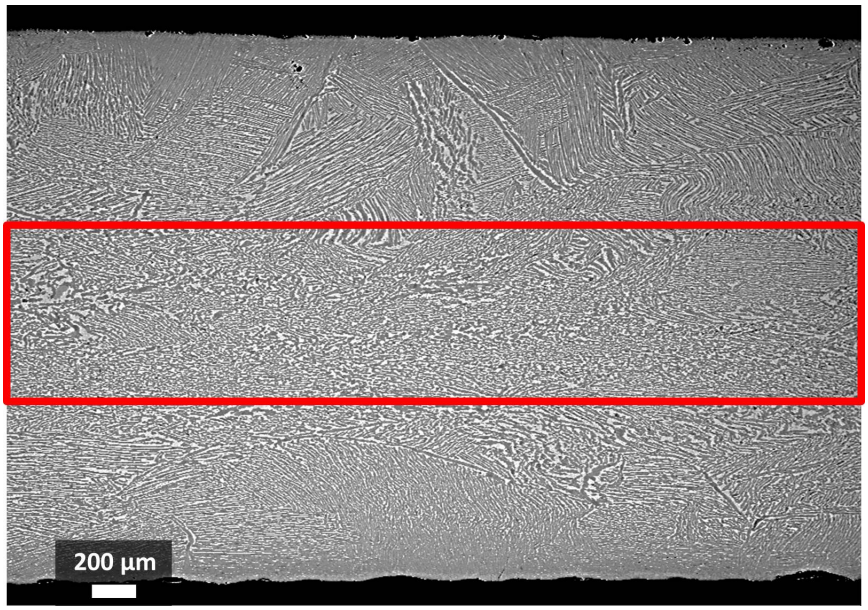

(b)

Figure 2.32: a) BSE micrograph at the center of the sample of Lx2 material after hot deformation at strain 1.34, immediate water quenching and subsequent 1 h annealing at 950°C and b) BSE micrograph at the center of the sample of Lx4 material after hot deformation at strain 1.34 immediate water quenching and subsequent 8h annealing at 950°C.

Fig. 2.32a is a BSE micrograph of the middle of the sample of Lx2 where

the applied strain is 1.34, observed after hot deformation and 1h subsequent annealing at 950°C. The area inside the red box is depicting the middle of the sample where no more colonies can be seen as spheroidization of the α phase has occurred. Also there is no indication of former β grain boundaries. Outside the red box where the strain is lower, colonies are still detectable and less fragmented. Similar comments can be made from Fig. 2.32b, concerning the Lx4 microstructure after hot deformation and subsequent annealing of 8h at 950°C. In this case, since the microstructure is coarser, an overall image across the whole sample could be obtained. In the red box, no former grain boundaries and no colonies can be recognized.

Further quantitative information regarding the microstructural evolution of both microstructures are presented in the following section.

2.4 Quantitative description of the microstructural evolution of Lx2 and Lx4 materials upon annealing after hot deformation to 1.34 strain

In the previous sections, experimental results are presented for both the Lx2 and Lx4 materials strained to 1.34. In addition, to the results of Lx2 and Lx4 at 0.36 strain, it appears that the globularization process is more difficult in the coarser lamellae material Lx4. The evolution of both microstructures during the post-deformation annealing will be described more quantitatively in the following. The focus will be placed on the experiments performed with the high applied strain, since the lower one, 0.36, appeared to be insufficient to promote significant globularization.

BSE micrographs were analyzed with the ImageJ software package to measure the α lamellae evolution from the experiments above described. The average area of individual lamellae/laths and their aspect ratios will be shown and commented below. Fig. 2.33 shows the evolution of these two quantities as a function of the annealing time for Lx2 and Lx4 materials after hot compression to 1.34.

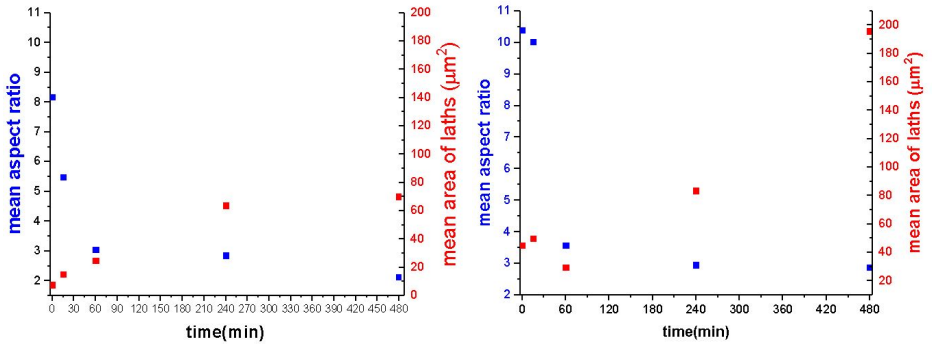

(a) (b)

Figure 2.33: Evolution of the average aspect ratio (blue) and average area of α lamellae/laths (red) in materials: a) Lx2 and b) Lx4 during annealing after hot compression to 1.34.

The mean aspect ratio decreases very quickly from the beginning in the Lx2 material (Fig. 2.33a, about 500 laths measured for each point). The mean aspect ratio decreased from about 8 to about 5.5 during the first 15 min annealing. Between the first 15 minutes and 1 hour, it keeps decreasing quickly, and then the change is much slower upon annealing beyond 1 hour. On the other hand, the average area of the laths increases steadily up to 4 hours annealing and then the growth rate slows down.

For the Lx4 microstructure, the measurements were more difficult to be done because the quality of our results was not as good as was for Lx2. The material was more difficult to be polished. Only 300 to 350 laths could be measured to build Fig. 2.33b. The points corresponding to 1 hour annealing are out of the global trend depicted by the other data. We suspect that something could go wrong with the experiment, possibly with the control of the annealing temperature, and the corresponding data will thus be ignored in the following comments. After 15 min annealing, very little change in both the average aspect ratio and lath area is observed, consistently with the EBSD maps shown on Figs. 2.29, 2.30 and 2.31. After 4h, the aspect ratio has significantly been reduced and the mean area increased but to a lower extent. Between 4h and 8h annealing, the aspect ratio does not really change any longer but the α laths are getting significantly coarser.

The results above suggest two regimes in the microstructure evolution. At the beginning, the aspect ratio decreases quickly and the area of the laths increases relatively slowly.

The governing mechanisms at the early stages of spheroidization are supposed to be those leading to α lamellae splitting : the motion due to surface diffusion at the α/β interfaces and the motion by mean curvature at the α/α subboundaries interfaces. If only those mechanisms would be active, the individual lath area would go down as a result of the splitting

process, and then keep being more or less constant as the shape of the lath is evolving. The average area of the laths is on the contrary slightly increasing from the beginning, which suggest that coarsening also occurs to some extent. The increase in size being rather small, one can nevertheless consider the splitting mechanisms as being the predominant ones in the early stages of the globularization process. On the other hand, over longer annealing times, the shape came close to globular and does not evolve so drastically anylonger, but the average area keeps increasing. The mechanism governing microstructure evolution is then turning to be the coarsening of the α particles.

To conclude, the appearance of subboundaries is confirmed to be of great importance for how the microstructure will be evolving and further investigation should be done on this subject.

2.5 Phase transformation during the experiments

Phase transformation is one of the possible mechanisms going along with the phenomenon of spheroidization, but will not be considered in the numerical modeling developments for the sake of simplification. Since isothermal evolutions were investigated, ignoring a possible change in phase volume fractions sounds reasonable. Nevertheless, it is has been reported in the literature [14–18] that α/β titanium alloys may undergo phase transformation from α to β during hot-deformation. An increase in β phase fraction has indeed been observed after deformation and quenching. During annealing after hot-deformation, the volume fractions came back to the static equilibrium values that can be predicted based on thermodynamic calculations. Taking this into account, it is worth checking the phase volume fraction evolution among our deformation experiments of initially lamellar microstructures.

Again by using the image processing software ImageJ, the α phase volume fraction was measured from BSE micrographs. The results displayed on Fig. 2.34 are average values obtained with about 10 pictures for each sample.

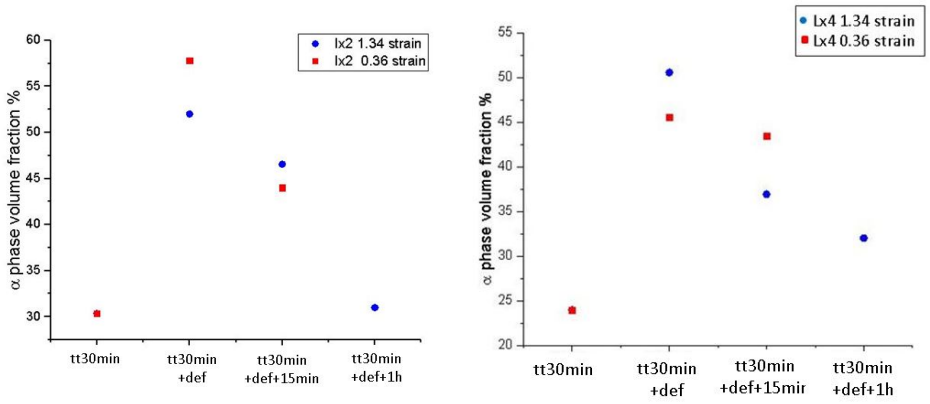

(a) (b)

Figure 2.34: Evolution of the α phase volume fraction before and after deformation, and during subsequent annealing for: a) Lx2 and b) Lx4.

The results are contradictory with the literature [14–18]. A raise in the β volume fraction during deformation was expected but instead a raise in α volume fraction was observed. This increase is quite large, from 25-30% to 45-55% within few seconds of deformation, and the value slowly goes back to the initial one upon subsequent long term annealing. On the other hand, experiments with both microstructures and both strain levels exhibit the same trends regarding the α phase evolution, which gives some consistency to these unexpected results. It is clear that further research should be done on this issue to better understand the mechanisms and kinetics of dynamic phase equilibrium and to validate the current results. At the present time, we can only keep in mind that the phase volume fractions are actually not constant during the spheroidization process, and include this point into the perspectives of this work.

2.6 Attempt of quantifying subboundaries

In previous sections of this chapter, as well as in the literature review, the important role of subboundaries formed during deformation on the further evolution of the microstructure was already emphasized. The most obvious example was material Lx2 which did not show any significant evolution upon the 15 min post-deformation annealing when submitted to the low strain of 0.36, but greatly evolved when deformed up to 1.34 strain. This is quantified on Fig. 2.35 where the evolution of the mean aspect ratio of the α laths during the 15 min holding is shown for both levels of strain. The aspect ratio of the α laths in both deformed microstructures is more or less the same but evolves very differently during the annealing. After 1.34 strain, the deformed lamellae presented much more subboundaries (Fig. 2.23) and their

the aspect ratio goes down during post-deformation annealing, as a result of lamellae fragmentation, while the 0.36 strained microstructure basically does not evolve with these regards.

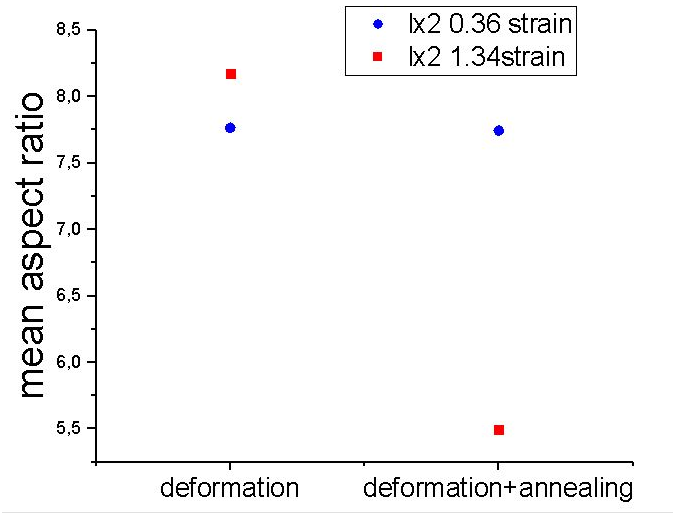

Figure 2.35: Evolution of the mean aspect ratio of α lamellae/laths in Lx2 material when hot-deformed to 0.36 (blue) strain and at 1.34 strain (red).

As reported in the literature [2–10], subboundaries initiate the process of lamellae splitting through the formation of grooves on α/β interfaces. Higher strains lead to the storage of more dislocations in the lamellae, and thus to the appearance of higher misorientations and subsequently to the formation of more subboundaries inside the lamellae. Somehow, the instability introduced by subboundaries is the reason why the mechanisms such as surface diffusion and motion by mean curvature are initiated.

EBSD data were analysed using the MTEX toolbox for the sake of quantifying the numbers of particles separated by subboundaries after deformation and after 1h or 4h subsequent annealing of Lx2 material at 1.34 strain. Maps with similar α lath total area were selected for these analyses. A threshold angle of 10°was set to define boundaries and the number of particles detected base on this criterion was measured. The particles detected with a 10°threshold are supposed to be the lamellae or laths. Then lower thresholds were applied (7°, 5°,4°and then 3°), leading to higher numbers of detected particles, representative for sub-grains delimited by the subboundaries. This way, the amount of subboundaries in the microstructures could be indirectly assessed. The number of particles was normalized for each data set by the total area of α laths. The results are shown on Fig. 2.36.

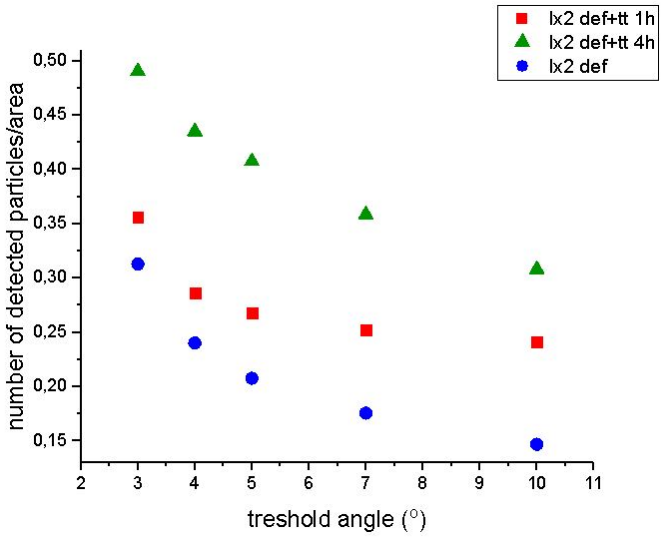

Figure 2.36: Number of particles detected per total α lamellae/laths area as a function of the considered angle threshold in Lx2 material submitted to 1.34 strain. Deformed state in blue, deformed and annealed for 1h in red, deformed and annealed for 4 hours in green.

As a general trend, the number of particles is increasing when decreasing the threshold angle, and this holds for all states, deformed, and deformed-and-annealed. This means that individual lamellae, and later laths, are composed by several portions delimited by subboundaries. Furthermore, as compared to the deformed state, the annealed materials have higher number of detected particles. This trend is more pronounced after 4h annealing than after 1h anneling. This is consistent with the fragmentation the lamellae into more and more (smaller) laths and/or the formation of more subboundaries (by recovery mecanisms) during annealing.

2.7 Conclusion

The performed experiments allowed to confirm the mechanisms reported in the literature and to get a clearer picture of how deformation and annealing affect the phenomenon of spheroidization.

Deformation is not homogeneous throughout the colonies. The colonies of lamellae that are parallel to the compression direction usually form kinks, which lead to quicker fragmentation. The areas where the lamellae are not parallel to the compression direction are more difficult to be fragmented. During deformation, lamellae accumulate dislocations, which induce internal misorientation and the formation of subboundaries. The number of subboundaries is increasing with increasing the strain level. Subboundaries

are the key for the future spheroidization of the α laths, which is initiated by the formation of grooves at the α/β interfaces.

The thickness of the lamellae was also confirmed to be an important factor. Thicker lamellae form less subboundaries (at a given strain level) and are more difficult to spheroidize. For the Lx4 material, with thick lamellae, a shape change towards a spherical form could indeed be detected only after long term annealing.

Subboundaries destabilize the lamellar microstructure and trigger interfacial mechanisms as surface diffusion at the α/β interface and motion by mean curvature at the α/α subboundaries. These two mechanisms are predominent at the beginning of the process and they lead the lamellae splitting into shorter laths. This can occur either already during deformation (at high strains and for thin lamellae), or during subsequent annealing.

Over long-term annealing, lath coarsening becomes the predominant and later on the only active mechanism. The physical mechanism behind coarsening is bulk atomic diffusion.

Even though only isothermal experiments have been performed, the phase volume fractions appeared to evolve significantly during deformation. An increase in α phase fraction was observed during deformation, which was unexpected (and remained unexplained) since the literature has reported the opposite trend in the same alloy (but with a different starting microstructure). During annealing, inverse phase transformation occurs to retrieve the static phase equilibrium volume fractions. Since it was impossible to consider the whole complexity of the involved mechanisms in the model to be developed, this effect was left apart, but this is definitely something which should be studied in the future.

All mechanisms contributing to the spheroidization of initially lamellar microstructures can be listed as follows:

Mechanism	Consequence	Occurs during
Crystal Plasticity	Formation of sub-boundaries	Hot deformation
Surface diffusion at the α/β interface	Grooving of the α/β interface	Hot deformation and/or early annealing stages
motion by mean curvature at the α/α sub-boundaries	Lamellae splitting Lath Spheroidization	
Bulk diffusion	Lath coarsening	Long-term annealing
	Dynamic phase transformation	Deformation
	Static phase transformation	Annealing

The following chapters will present the numerical framework that was de-

veloped with the aim of being able in the future to simulate the spheroidization process in a digital microstructure. In this numerical part of the PhD, the focus will be placed on the lamellae splitting in a system already containing subboundaries, and thus on the two involved mechanisms: the motion by surface diffusion at the α/β interfaces and the motion by mean curvature of the α/α interfaces.

Chapter 3

Introducing a numerical framework for the numerical modeling of α lamellae splitting

Résumé en français

Une méthode à champ complet basée sur la méthode Level-Set implémente dans un cadre Eléments Finis a été teste pour simuler les mécanismes physiques de migration interfaciale menant à la subdivision des lamelles et à l'évolution vers une forme globulaire. Deux approches sont présentées en détail dans ce chapitre, la première utilise un cadre Eulérien et la deuxième dans un cadre Lagrangien. Ces deux approches sont basées sur plusieurs outils numériques existants dans la librairie Elément Finis C++ CIMLIB, qui a été développée dans le laboratoire du CEMEF.

Plusieurs cas académiques sont présentés pour valider les deux approches. Ensuite, les deux approches sont comparées pour trouver la plus efficace pour la simulation de la subdivision des lamelles α et l'évolution des particules α vers une forme globulaire. De plus, différentes techniques d'adaptation de maillage sont testées pour simuler efficacement l'évolution de la forme des particules de phase α.

Il est trouvé que la méthode dans le cadre Lagrangien avec l'outil d'adaptation de maillage conforme FITZ est la plus efficace pour modéliser les mécanismes physiques considérés dans ce travail, et c'est donc cette méthode qui a été choisie pour les cas plus complexes considérés dans les chapitres suivants.

3.1 Numerical modeling

Both chapter 1 and chapter 2 have drawn the attention to the importance of the appearance of subboundaries inside the α lamellae for the post-deformation microstructural evolutions. Due to the existence of α/α subboundaries after deformation, the α lamellae turn into an unstable configuration and diffusion mechanisms take place in order to restore microstructural equilibrium.

By considering the importance of this behavior to the spheroidization phenomenon, one of the main objectives of this work is, at the scale of Fig. 3.1, to efficiently simulate the α lamellae splitting inside a β grain due to the appearance of α/α subboundaries during deformation.

To reach this objective, it is important to propose an adapted numerical framework. As already mentioned, the two instantaneous mechanisms responsible for the α lamellae splitting are the motion due to surface diffusion on the α/β interfaces and the motion due to mean curvature on the α/α subboundaries. The rest of the involved mechanisms are not taken into account in this work.

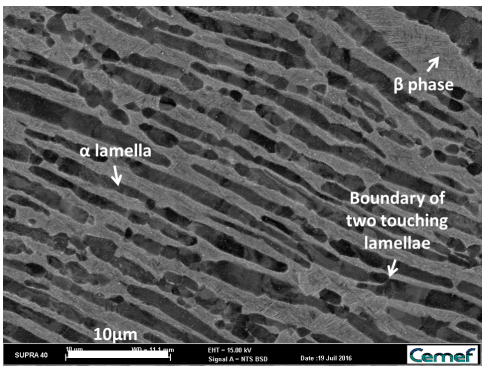

Figure 3.1: Experimental image of α lamellae inside a β grain.

A FE/level-set method is proposed for simulating the splitting of the α lamellae and the subsequent shape evolution of the α laths towards a spheroidal shape during the stage of annealing. The basic idea is that the α lamellae are represented as a signed distance function. The simulation domain will be considered as the β phase/grain.

This provides a global framework for simulating efficiently the lamellae splitting mechanisms during the spheroidization phenomenon. This chapter will illustrate in detail all the steps followed in order to build the numerical framework.

In all the numerical simulations, unstructured FE meshes, $\mathcal{T}_h$, of the domain calculation Ω are considered. The elements, $e \in \mathcal{T}_h$, are assumed triangular in 2D and tetrahedral in 3D. In the following, the space of con-

tinuous piecewise linear functions (P1) over the domain Ω will be denoted $\mathcal{V}_h$.

3.2 A level-set method to describe the α/β lamellae interfaces

A level-set (LS) method was used since it enables to implicitly represent an object and to describe its evolution on a domain Ω [23]. The main idea behind this method is that a distance function ϕ returns the Euclidean distance, denoted d, to the boundary Γ of a sub-domain $\Sigma \in \Omega$:

$$\Gamma(t) = \{x \in \Omega, \phi(x,t) = 0\}, \tag{3.1}$$

and generally a signed convention is assumed where ϕ is defined positive inside Γ and negative outside as following:

$$\phi(x,t) = \begin{cases} d\left(x, \Gamma\left(t\right)\right), x \in \Sigma \\ -d\left(x, \Gamma\left(t\right)\right), x \notin \Sigma \end{cases} \tag{3.2}$$

The evolution of $\phi(x,t)$ for an imposed velocity field $v(x,t)$ is then governed by the following convection equation [23, 24]:

$$\frac{\partial \phi}{\partial t} + \vec{v} \cdot \nabla \phi = 0. \tag{3.3}$$

The main advantage for using LS method is that topological changes can be captured efficiently. Some intrinsic geometric properties of the interfaces can also be easily determined. More details are given below.

3.3 Level Set formulation of α lamellae

A level-set (LS) model was formulated in order to deal with the topological changes at the α/β interfaces. The 0-isosurface of the LS will represent the α/β interfaces. One of the main advantages of the LS method, as already mentioned, is that certain geometric entities can be easily computed [25, 26]. Specifically, with the chosen sign convention, the unitary outside normal $\vec{n}$ and the mean curvature (i.e. the trace of the curvature tensor in 3D equivalent to the sum of the main curvatures) κ can be obtained as:

$$\vec{n} = \frac{-\nabla \phi}{\|\nabla \phi\|}, \tag{3.4}$$

and

$$\kappa = div(\vec{n}) = -\nabla \cdot \frac{\nabla \phi}{\|\nabla \phi\|}. \tag{3.5}$$

The interface Γ submitted to a velocity field $\vec{v}$ can be modeled by solving the convective equation Eq. 3.3. If the LS function is initially defined as a distance function (see Eq. 3.2), this property is not naturally preserved during convection. This metric property is equivalent to verifying $\|\phi(x,t)\| = 1$ and can be retrieved by a reinitialization/redistancing procedure [23]. More details are given in section 3.5.

Taking into account Eq.1.15, the following form of $\vec{v}$ can be considered to simulate α laths/lamellae:

$$\vec{v} = v_n\vec{n} = (v_s + v_\kappa)\,\vec{n} = (\underbrace{B\Delta_s\kappa}_{v_s}\underbrace{-A\kappa}_{v_\kappa})\vec{n}, \tag{3.6}$$

with

$$B = \begin{cases} \frac{\gamma_{\alpha\beta}\nu\Omega^2 D_{\alpha\beta}}{kT} & at\ the\ \alpha/\beta\ interfaces \\ \\ 0 & otherwise \end{cases} \tag{3.7}$$

and

$$A = \begin{cases} \frac{\gamma_{\alpha\alpha}bf\Omega}{kT}e^{-\frac{Q}{RT}} & at\ the\ \alpha/\alpha\ interfaces \\ \\ 0 & otherwise \end{cases} \tag{3.8}$$

It can also be proven that in the considered LS formulation, v_n [26] can be rewritten as

$$v_n = B\Delta_s\kappa - A\kappa = \frac{B}{\|\nabla\phi\|}\nabla\cdot(\|\nabla\phi\|P\nabla\kappa) - A\kappa, \tag{3.9}$$

where P is the projection matrix on the tangent plane to the surface:

$$P = I - \vec{n}\otimes\vec{n} = I - \frac{\nabla\phi}{\|\nabla\phi\|}\otimes\frac{\nabla\phi}{\|\nabla\phi\|}. \tag{3.10}$$

and I is the identity matrix.

In the considered LS framework, the velocity is then defined in the entire domain and corresponds to the vicinity of the 0-isovalue of the LS function, i.e. Γ, to the interface velocity. In the following section, more information are given regarding the formulation of the surface diffusion velocity as proposed in [26].

3.4 Velocity approximation in context of surface diffusion

In order to model the induced flow from the surface diffusion mechanism at the α/β interface, a FE methodology is adopted. At any time t, the normal transport velocity v_n is expressed as:

$$v_n = v_s = B\Delta_s\kappa = \frac{B}{\|\nabla\phi\|}\nabla\cdot(\|\nabla\phi\|P\nabla\kappa) \tag{3.11}$$

with B defined in Eq. 3.7 and P as defined in Eq. 3.10.

The B coefficient is defined as a constant. Thus, it is chosen to neglect any anisotropy concerning the interface energy and the diffusivity. Furthermore, isothermal conditions are assumed. The time evolution of $\Gamma(t)$ due to surface diffusion can then be obtained by solving the following convective system:

$$\begin{cases} \frac{\partial\phi}{\partial t} + v_s\vec{n}\cdot\nabla\phi = 0 \\ \\ \phi(x,0) = \phi^0(t) \end{cases} \tag{3.12}$$

The interface can then be obtained at each time step as the 0-isovalue of the LS function and the velocity is updated by using Eq. 3.11 before the following time step.

3.4.1 Surface diffusion velocity identification and transport resolution

Looking at Eq. 3.11, one of the basic problems that arises is that the velocity v_s is defined by the surface Laplacian of the mean curvature. Since a P1 description of the LS is used, the velocity is then a function of the fourth order spatial derivative of ϕ. The methodology used to solve this problem and to calculate the surface diffusion velocity at each time step of the FE scheme is based on the FE strategy introduced by Bruchon et al. in [26, 27]. This surface diffusion methodology which is integrated in CimLib (the parallel C++ FE library used in this work [28]), will be called from now on in the manuscript as (κ,v_s)-identification solver.
The methodology is based on a FE strategy detailed below.

To begin with, a smoothed modified $\tilde{\phi}$ LS function is evaluated to describe the interfaces, rather than using directly the distance function as in Eq. 3.2:

$$\tilde{\phi}(x,t) = \begin{cases} \frac{2E}{\pi}\sin\left(\frac{\pi}{2E}d(x,t)\right) \text{ if } d(x,t)\in[-E,E] \\ -\frac{2E}{\pi} \text{ if } d(x,t)\leq -E \\ \frac{2E}{\pi} \text{ if } d(x,t)\geq E \end{cases} \tag{3.13}$$

The paramater E can be seen as the $\tilde{\phi}$ mid-thickness and it will be generally directly linked (equal) to the mesh adaptation and reinitialization thicknesses in the following. As $sin\,(x) \approx x$ for small values of $|x|$:

$$\tilde{\phi} \approx d \text{ near the 0-isovalue.} \tag{3.14}$$

Moreover, as a LS function, Eqs. 3.1, 3.3, 3.4, 3.5 and 3.11 are, of course, verified by $\tilde{\phi}$.
The unknowns $\tilde{\phi}$, κ and v_s are then approximated, respectively, by $\tilde{\phi}_h$, κ_h and v_{s_h} belonging to $\mathcal{V}_h$. The time scale is discretized and a field, F, evaluated at time t will be denoted F^t. In every time step $\tilde{\phi}_h^t$ is assumed to be known. Then, by evaluating Eqs. 3.5 and 3.11 for $\tilde{\phi}$, the κ_h^t and the $v_{s_h}^t$ fields could be computed *a priori*. However, at this point the first difficulty appears. Since $\tilde{\phi}_h$ is piecewise linear, the gradient will be a constant per element (P0) and the following derivatives will be equal to zero. A weak formulation is adopted to solve this problem. The second difficulty comes from the non-linear relationship between $\tilde{\phi}$, κ and v_s. In order to overcome this difficulty, $\tilde{\phi}_h^{t+dt}$ is explicitly determined by considering the surface diffusion velocity at time t. Finally, in order to avoid numerical oscillations in the full explicit resolution [26, 27], the numerical method consists of building a system where the unknowns are the P1 mean curvature κ_h^t and the P1 velocity $v_{s_h}^t$ and by introducing a regularization term. In order to introduce implicitly this regularization term, a first order Taylor expansion is considered:

$$\tilde{\phi}_h^{t+dt} + o(dt) = \tilde{\phi}_h^t + \frac{\partial \tilde{\phi}_h^t}{\partial t} dt, \tag{3.15}$$

which is defined as $\tilde{\phi}_h^{t+\frac{1}{2}}$.

Substituting $\tilde{\phi}$ in Eq. 3.3, we obtain $\frac{\partial \tilde{\phi}}{\partial t} = -\vec{v} \cdot \nabla \tilde{\phi}$. By substituting this equation at time t in the right side of Eq. 3.15:

$$\tilde{\phi}_h^{t+\frac{1}{2}} = \tilde{\phi}_h^t - \vec{v}_h^t \cdot \nabla \tilde{\phi}_h^t dt. \tag{3.16}$$

By using $\vec{v}_h^t = v_{s_h}^t \vec{n} = -v_{s_h}^t \nabla \tilde{\phi}_h^t / \|\nabla \tilde{\phi}_h^t\|$, Eq. 3.16 becomes:

$$\tilde{\phi}_h^{t+\frac{1}{2}} = \tilde{\phi}_h^t + v_{s_h}^t \|\nabla \tilde{\phi}_h^t\| dt. \tag{3.17}$$

Furthermore, by considering Eq. 3.5 applied to $\tilde{\phi}$ at time t with the use of $\tilde{\phi}_h^{t+\frac{1}{2}}$ and Eq. 3.17:

$$
\begin{aligned}
&\kappa = -\nabla \cdot \left(\frac{\nabla \tilde{\phi}}{\|\nabla \tilde{\phi}\|} \right) \Rightarrow \kappa_h^t = -\nabla \cdot \left(\frac{\nabla \tilde{\phi}_h^{t+\frac{1}{2}}}{\|\nabla \tilde{\phi}_h^{t+\frac{1}{2}}\|} \right) \\
&\Rightarrow \kappa_h^t = -\nabla \cdot \left(\frac{\nabla \tilde{\phi}_h^t + \nabla \left(v_{s_h}^t \|\nabla \tilde{\phi}_h^t\| dt \right)}{\|\nabla \tilde{\phi}_h^{t+\frac{1}{2}}\|} \right) \\
&\Rightarrow \kappa_h^t + dt \nabla \cdot \left(\frac{\nabla \left(\|\tilde{\phi}_h^t\| v_{s_h}^t \right)}{\|\nabla \tilde{\phi}_h^{t+\frac{1}{2}}\|} \right) = -\nabla \cdot \left(\frac{\nabla \tilde{\phi}_h^t}{\|\nabla \tilde{\phi}_h^{t+\frac{1}{2}}\|} \right).
\end{aligned}
\tag{3.18}
$$

In addition, by considering Eq. 3.11 applied to $\tilde{\phi}$, we obtain:

$$
v_{s_h}^t \|\nabla \tilde{\phi}_h^t\| - B \nabla \cdot \left(\|\nabla \tilde{\phi}_h^t\| P_{\tilde{\phi}_h^t} \nabla \kappa_h^t \right) = 0. \tag{3.19}
$$

The idea of the mixed formulation proposed by Bruchon et al. [26, 27], is then to solve the system defined by the Eqs. 3.18 and 3.19 with some simplifications. First, $\|\nabla \tilde{\phi}_h^t\|$ is replaced by the value 1 in the second term of the left-side part of Eq. 3.18. This approximation is acceptable thanks to Eq. 3.14. Second, the term $\|\nabla \tilde{\phi}_h^{t+\frac{1}{2}}\|$ in Eq. 3.18 is replaced by the approximation $C = \|\nabla \tilde{\phi}_h^t + dt \nabla v_{s_h}^{t-dt}\|$.

Finally, the following system is solved:

$$
\begin{cases}
\kappa_h^t + dt \nabla \cdot \left(\frac{\nabla v_{s_h}^t}{C} \right) = -\nabla \cdot \left(\frac{\nabla \tilde{\phi}_h^t}{C} \right) \\
\\
v_{s_h}^t \|\nabla \tilde{\phi}_h^t\| - B \nabla \cdot \left(\|\nabla \tilde{\phi}_h^t\| P_{\tilde{\phi}_h^t} \nabla \kappa_h^t \right) = 0
\end{cases}
\tag{3.20}
$$

which leads to the following weak formulation: at time t, assuming $\tilde{\phi}_h^t$ known, find $\left(\kappa_h^t, v_{s_h}^t\right) \in \mathcal{V}_h \times \mathcal{V}_h$ as

$$
\forall \varphi_h \in \mathcal{V}_h \begin{cases}
\int_\Omega \kappa_h^t \varphi_h \, d\Omega + dt \int_\Omega \nabla \cdot \left(\frac{\nabla v_{s_h}^t}{C} \right) \varphi_h \, d\Omega = -\int_\Omega \nabla \cdot \left(\frac{\nabla \tilde{\phi}_h^t}{C} \right) \varphi_h \, d\Omega \\
\int_\Omega v_{s_h}^t \|\nabla \tilde{\phi}_h^t\| \varphi_h \, d\Omega - B \int_\Omega \nabla \cdot \left(\|\nabla \tilde{\phi}_h^t\| P_{\tilde{\phi}_h^t} \nabla \kappa_h^t \right) \varphi_h \, d\Omega = 0
\end{cases}
\tag{3.21}
$$

Interestingly, by assuming that no lamella crosses the boundary domain, the use of $\tilde{\phi}$ rather than ϕ ensures that the boundary terms which can be obtained by the divergence theorem applied to Eq. 3.21 vanish.
Finally, Eq. 3.21 is equivalent to: at time t, assuming $\tilde{\phi}_h^t$ known, find $\left(\kappa_h^t, v_{s_h}^t\right) \in \mathcal{V}_h \times \mathcal{V}_h$ as

$$
\forall \varphi_h \in \mathcal{V}_h \begin{cases}
\int_\Omega \kappa_h^t \varphi_h \, d\Omega - dt \int_\Omega \frac{1}{C} \nabla v_{s_h}^t \cdot \nabla \varphi_h \, d\Omega = \int_\Omega \frac{1}{C} \nabla \tilde{\phi}_h^t \cdot \nabla \varphi_h \, d\Omega \\
\int_\Omega v_{s_h}^t \|\nabla \tilde{\phi}_h^t\| \varphi_h \, d\Omega + B \int_\Omega \|\nabla \tilde{\phi}_h^t\| P_{\tilde{\phi}_h^t} \nabla \kappa_h^t \cdot \nabla \varphi_h \, d\Omega = 0
\end{cases}
\tag{3.22}
$$

3.5 Direct Reinitialization (DR) Methodology

One of the weaknesses of using the LS method is that, after the resolution of the advection equation Eq. 3.3, the LS function, initially defined as a signed distance function (Eq. 3.2), stops being a distance function, i.e. the metric property $\|\nabla\phi\| = 1$ is no longer satisfied. Reinitialization is then needed in order to restore this metric property [23].

Reinitialization is a very important step for our LS methodology. Indeed, as usual in a LS convective Eulerian framework, a periodic reinitialization procedure is needed to keep a precise description of the interface. In our computations, the reinitialization must be performed at each time step for two main reasons. First, as it will be illustrated in the next section, our metric-based meshing/remeshing strategy undermines the use of the distance to the laths interface. Second, it was illustrated in the previous section that the the metric property $\|\nabla\tilde{\phi}\| = 1$ is a hypothesis of the (κ,v_s)-identification solver. Thus, it was important to use in this work an efficient and precise methodology to reinitialize the LS functions (around their 0-isovalues) used at each time step of our simulations.

Different methods exist for reinitialization of the LS. Classical approaches consist in solving, separately, the convective part and the reinitialization part thanks to the resolution of a classical Hamilton-Jacobi system [23], [29] or to adopt an unified advection and re-distancing methodology by solving one single equation based on a smooth description of the LS [30, 31].

Here, a new approach is followed as it was developed from Shakoor et al. [32]. In this work, a new parallel and direct reinitialization algorithm based on the use of a *k-d tree* space-partitioning strategy is presented. In this algorithm, the $\Gamma(t)$ interface is firstly discretized into a collection of segments (or triangles in 3D cases). Reinitialization of the signed distance function can be performed at any mesh node by computing the distance function between the node and all the segments (or triangles) and by storing the smallest one as the new value of the distance function. In this rough shape, the aforementioned algorithm can be time consuming. Thus, it has been enhanced with *k-d tree* and an efficient bounding box strategy enabling to maximize the numerical efficiency [32].

There are many advantages for using this algorithm. Firstly, given a P1 representation of the LS function (linear by element interpolation), the Direct Reinitialization method which gives a geometrical solution is very accurate in comparison with other solutions [32]. Also, it enables us to avoid the validation/ calibration of non-physical parameters necessary to reinitialize the LS function as in classical Hamilton-Jacobi resolution [29], [31]. Furthermore, another advantage in comparison with the other methods is that we can obtain directly an exact P1 description of the normal $\vec{n}$ to $\Gamma(t)$, which helps to compute the transport velocity, rather than following the classical way where we compute the normals by performing a P1 interpola-

tion of the first derivative of the LS function [33]. Since restoring the metric property $\|\nabla\phi\| = 1$ everywhere in the domain can be time consuming, this algorithm also provide us with the possibility of restoring the metric property only at the direct vicinity of the interface. This, in addition to the *k-d tree* methods and bounding box, renders the algorithm extremely time efficient.

In the next section we are going to present the main methodologies followed in this PhD in order to efficiently simulate the shape evolution of the α lamellae.

3.6 Simulating motion that leads to lamellae splitting

In the previous sections all the numerical tools used for the simulations have been described. The final goal is to be able to efficiently simulate the α lamellae splitting and subsequent α lath spheroidization.

In this section we will describe two different methodologies developed for this purpose in order to test their efficiency and to choose the best one. The first methodology was built in an Eulerian framework and the second was built in a Lagrangian framework. The following sections describe both methodologies and academic tests cases to compare it.

3.6.1 Eulerian approach

3.6.1.1 The procedure

The first approach is based on a classical Eulerian framework. The method can be summarized by the flow chart described in Fig. 3.2:

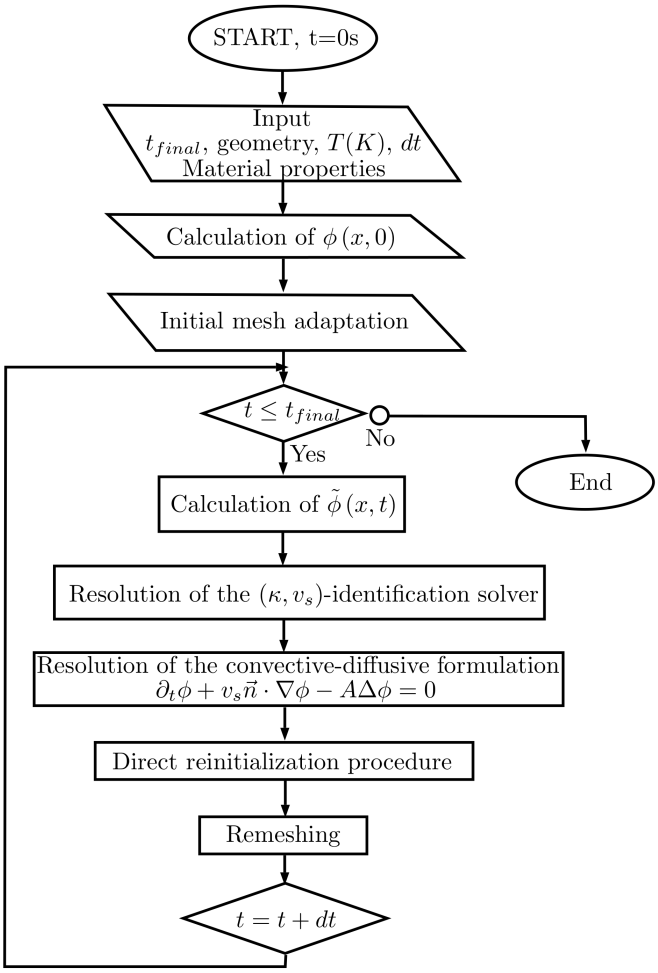

Figure 3.2: Flow chart of the methodology in the Eulerian framework.

The first step of our methodology consists of the calculation of the velocity v_s with the $(\kappa,\ v_s)$-identification solver described in section 3.4. As in [34], the mean curvature part of the velocity is, in fact, taken into account thanks to the diffusive formulation. Indeed, if ϕ remains a distance function, $v_\kappa \vec{n} \cdot \nabla\phi$ can be simplified as $v_\kappa \vec{n} \cdot \nabla\phi = -A\nabla \cdot (\nabla\phi)\, \nabla\phi \cdot \nabla\phi = -A\Delta\phi$. Finally, Eq. 3.3, can be written:

$$\partial_t \phi + v_s \vec{n} \cdot \nabla\phi - A\Delta\phi = 0. \tag{3.23}$$

An implicit P1 solver with a Streamline Upwinding Petrov-Garlerkin (SUPG) method for the stabilization, and the Generalized Minimal Residual Method (GMRES) for the numerical resolution of the linear system of equations are used to solve Eq. 3.23 [28, 35]. Subsequently, direct reinitialization around the 0-isovalue is performed.
Different remarks can be done here:

- the use of a diffusive part in the kinetic resolution given by Eq. 3.23 is a third reason explaining the necessity of reinitialization at each time step,
- if $\tilde{\phi}$ was used for the (κ, v_s)-identification solver and could be used for the kinetic equation as well, we prefer here to deal with the distance function, ϕ, reinitialized in the thickness $[-E, E]$ in order to verify precisely that the norm of the gradient of the used LS function remains equal to 1 in all the thickness $[-E, E]$,
- by assuming that no lamella crosses the boundary domain, no boundary conditions are needed to solve Eq. 3.23.

In the next section, our meshing strategy is described.

3.6.1.2 Mesh adaptation techniques

One of the main difficulties that we have faced during our developments is that in comparison with the β grain size, the α lamellae are very thin. As a result the LS of the lamellae are very difficult to be described within a reasonable FE mesh. In specific, as we have seen in the previous chapters, the average size of α lamellae is in μm while the mean size of the β grains is in mm. As the distance calculation in a LS method is in dependence with the mesh size, it is very important to use a non homogeneous mesh in order to represent efficiently the α lamellae without dealing with a homogeneous very fine and computationally demanding FE mesh.

In a context of numerical simulations based on FE methods, mesh adaptation techniques can improve the efficiency of numerical resolutions and reduce the calculation time. The mesh adaptation method followed in our Eulerian context was based on the calculation of a metric on each node of the FE mesh and the use of a topological mesher, MTC, developed in CEMEF [36]. Using local meshing/remeshing strategies enable us to describe the LS interface evolution in a precise way by limiting the computational cost.

A metric is a symmetric positively defined tensor which represents a local base to modify the way of computing a distance, so that:

$$\|\vec{u}\|_M = \sqrt{{}^t\vec{u}M\vec{u}}, \qquad <\vec{u},\vec{v}>_M = {}^t\vec{u}M\vec{v}, \tag{3.24}$$

with M a symmetric positive definite tensor [35]. The eigenvalues of the metric tensor M are linked with the mesh sizes, and the eigenvectors define the direction in which these mesh sizes are applied.

The first metric calculation used was proposed in [35]. To begin with, the length $2E$ is defined as the characteristic thickness around the interface for the mesh adaptation. Far from the interface the mesh is fixed as isotropic

and the mesh size is equal to h_d. Inside the narrow band around the 0-isovalue defined by $|\phi| \leq E$, the mesh size is then reduced by a factor $m = \frac{h_d}{h}$ in the normal direction of the interface. This result is obtained by considering the following metric:

$$M = C(\frac{\nabla\phi}{\|\nabla\phi\|} \otimes \frac{\nabla\phi}{\|\nabla\phi\|}) + \frac{Id}{{h_d}^2}, \tag{3.25}$$

with

$$C = \begin{cases} 0 & if|\phi| \geq E \\ \frac{1}{h^2} - \frac{1}{{h_d}^2} & if|\phi| \leq E \end{cases} \tag{3.26}$$

where Id corresponds to the identity tensor [35]. This metric corresponds to an anisotropic mesh close to the interface, with reduced mesh size h near to the interface in the direction $\nabla\phi$ and equal to h_d in the other directions. Furthermore, with some modifications on Eqs. 3.25 and 3.26, we can deal with other remeshing strategies. Firstly, we can consider:

$$M = \tilde{C}Id, \tag{3.27}$$

with

$$\tilde{C} = \begin{cases} \frac{1}{h^2} & if|\phi| \leq E \\ \frac{1}{{h_d}^2} & if|\phi| \geq E \end{cases} \tag{3.28}$$

to obtain an isotropic fine mesh around the interface with a mesh size equal to h and a coarse mesh far ($|\phi| \geq E$) from the interfaces with a mesh size equal to h_d. This metric is illustrated in Fig. 3.3 for the case of an ellipse ($a = 0.5mm$ and $b = 0.1mm$ with $h = 1\mu m$, $h_d = 10\mu m$ and $E = 10\mu m$). If we also consider h as a function of $|\phi|$ in Eq. 3.26 or in Eq. 3.28, we can obtain a continuous refinement from the coarse mesh size to the fine mesh size as proposed in [37].

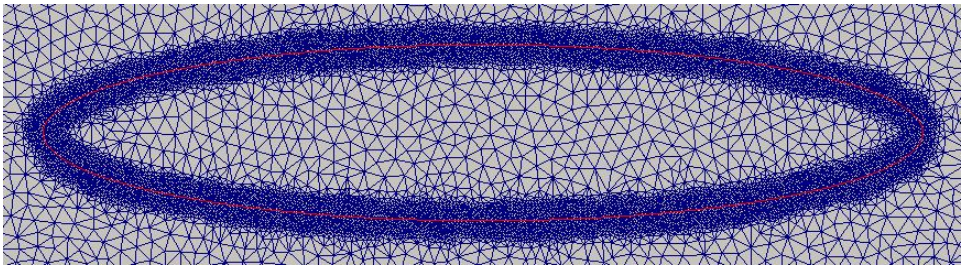

(a)

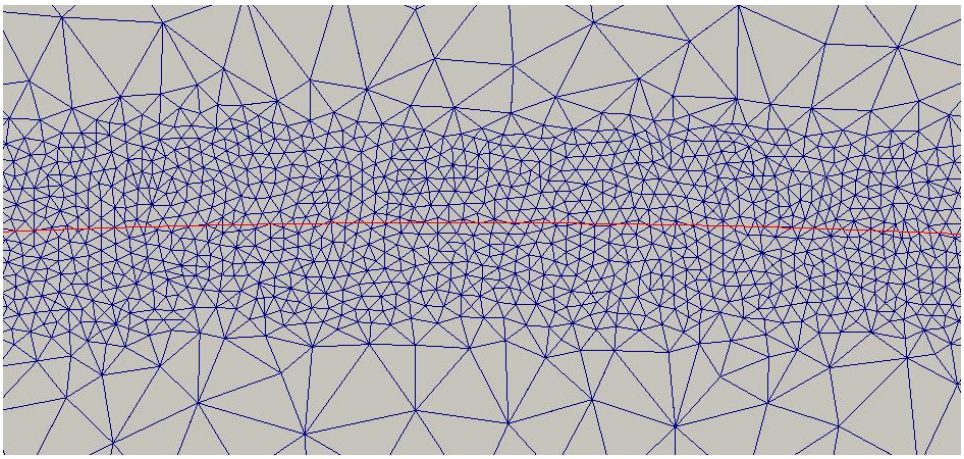

(b)

Figure 3.3: (a)Global isotropic mesh refinement with the use of the metric defined by Eq. 3.25 and Eq. 3.26, (b) A zoom. The red lines correspond to the 0-isovalue of the LS function.

A second method of metric calculation tested during our computations in the Eulerian framework was to perform an error analysis in order to reach an ideal mesh (without real improvement on the results comparatively to the method described previously). This notion of ideal mesh undermines generally the minimization of a discretization error for a given field and a fixed number of elements. The metric is then directly given by the error estimator which will concentrate the mesh adaptation in the sharpest gradient zones of the considered field [38–40]. The method adopted here was the one proposed in [38] and [40]. No mechanical field was considered to evaluate the discretization error but a function linked to the distance function. Indeed, as a function of constant gradient in norm, the distance function can't be used directly. Finally, the function $\tilde{\phi}$ described previously was an input of the error estimator when it was used.

3.6.2 Lagrangian approach

3.6.2.1 The procedure

The second approach tested is based on an enhanced Lagrangian framework. This second method is summarized by the flow chart described in Fig. 3.4:

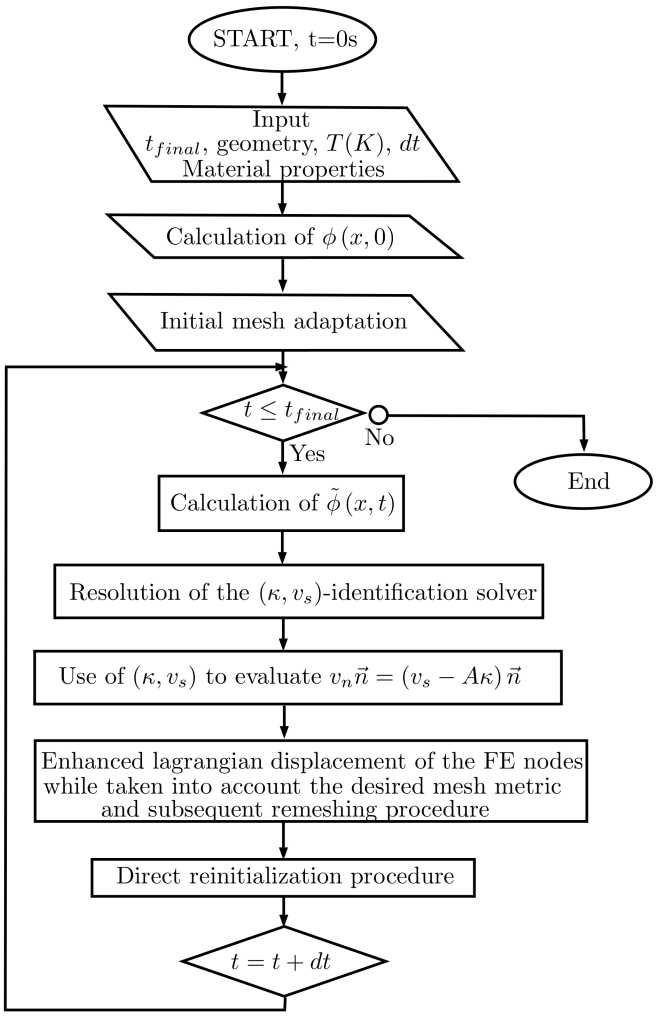

Figure 3.4: Flow chart of the methodology in the Lagrangian framework.

The first step remains the calculation of the surface diffusion velocity and the mean curvature using the (κ, v_s)- identification solver. The velocity (see Eq. 3.6) that couples both motion by surface diffusion and motion by mean curvature is constructed by calculating separately and adding the two different velocities as : $\vec{v} = (v_s - A\kappa)\vec{n} = (B\Delta_s\kappa - A\kappa)\vec{n}$. An enhanced Lagrangian formulation is then used, where we employ the advantages of a new mesh adaptation tool (FITZ) developed by M. Shakoor et al. [41]. In

the following section, we are going to give a short description of FITZ mesh adaptation methodology and on its advantages.

3.6.2.2 Adaptive meshing and remeshing with Fitz

It has been clearly stated numerous times until now in this work, that meshing and remeshing is very important for efficiently capturing the shape evolution of the α lamellae and to avoid numerical diffusion. This holds true, especially for simulating the interfacial kinetics during the spheroidization phenomenon where the volume conservation is very important since physically we do not consider yet phase transformation but only the shape evolution of the phases.

By working on a Lagrangian framework, the convection problem is solved by updating the mesh. As previously mentioned, the α lamellae are described by a signed distance function with a P1 formulation. The signed distance function is computed at the mesh nodes and the evolution of the interfaces is then obtained by computing the Lagrangian displacements of each node. Usual Lagrangian mesh movement leads to deterioration of the quality of the elements (or even to possible flipping of elements) and as a result, frequent remeshing operations are required. During remeshing, there is a tendency of diffusing the interfaces and volume at each iteration. The new meshing and remeshing method realized in the FITZ tool, has been proven to reduce volume diffusion in a Lagrangian framework especially in a context of large deformation and displacement. A part of FITZ is common with the mesher MTC. Since MTC was developed many years ago, the developments of FITZ come to enhance the existing algorithms with some new operators as fitting, locking, refining and coarsening of the interface of the LS [41, 42].

Taking into account that the LS function represents α lamellae inside the domain, FITZ first considers the metric field, described in the previous section 3.6.1.2, in order to have more refined mesh around the interfaces, and to control the mesh size in the whole domain. Remeshing is performed. If the quality of the mesh is not good enough, the sequence of firstly calculating the LS, afterwards defining the metric and at the end remeshing, is repeated several times until reaching the desired mesh quality. At that point FITZ operates the fitting of mesh at the interface. The procedure lists all the edges in the mesh and then splits the ones where the LS function changes its sign. For more information regarding this procedure the reader can refer to [41,42]. In the cited papers the criteria and regulations of FITZ performing meshing and remeshing are explained in depth, as well as the methodologies followed in order to prevent poor quality elements. After the body fitted interface is obtained, remeshing is again performed by FITZ in order to maintain the quality of the mesh at the interface and the whole domain.

To conclude, the main advantages of using FITZ for our developments

are: (a) the volume conservation and that (b) the body fitted interface help us capture efficiently the triple junction that is formed between an α/α sub-boundary and the α/β interfaces. Both seem very interesting advantages regarding the simulation of the lamellae splitting in order to avoid the volume diffusion that is observed in classical Eulerian formulation. Fig. 3.5 illustrates, in context of the Fig. 3.3, the results obtained with the use of the FITZ meshing algorithm for the same metric. The main difference this time is that 0-isovalue (red line) is conformed to the mesh.

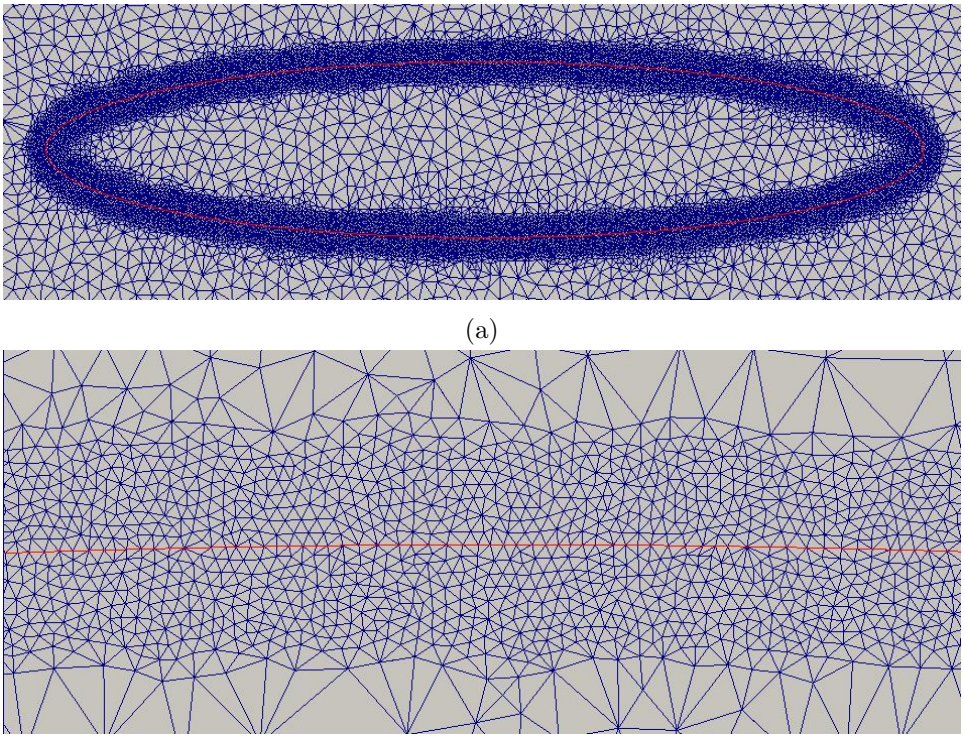

(a)

(b)

Figure 3.5: Same case than the Fig. 3.3 realized with the FITZ capabilities: (a) global mesh, (b) zoom. The red lines corresponds to the 0-isovalue of the LS function.

3.7 Velocity application area

At this point, it is important to be more precise regarding how we apply the velocity field in order to move our LS. In both Eulerian and Lagrangian space, we define a P1 velocity field (linear by element interpolation). The whole process of surface diffusion and motion by mean curvature occurs either at the α/β interface either at the α/α interface, respectively. For that reason the velocity field is then applied only in the narrow band around the

0-isovalue already defined as $|\phi| \leq E$.

We have described the two methodologies considered in order to simulate the α lamellae splitting. In the following section, we are going to present results from simulations performed with these two methodologies in order to examine and compare their efficiency.

3.8 Results

Having discussed the theoretical background of the Eulerian approach and the Lagrangian approach, results from some first academic cases are presented. By comparing these results, we are going to decide which of the two approaches is more efficient for simulating the lamellae splitting phenomenon. To begin with, we perform academic cases for simulating surface diffusion and motion by mean curvature separately using both approaches. Tests comparing the efficiency of different mesh adaptation techniques are also presented. Finally, the final academic case of this chapter illustrates the coupling of the two motions again by comparing the two proposed approaches.

3.8.1 Tests on surface diffusion simulations on static mesh using the Eulerian approach

In this section, we are considering an ellipsoid shape under surface diffusion. We want to test the efficiency of the proposed formulation for a simple case where an analytical solution is known. We considered a computational domain of $1mm \times 1mm$ square centered in (0,0). An initial ellipse of axis $a = 0.3mm$ and $b = 0.2mm$ is considered:

$$\frac{x^2}{a^2} + \frac{y^2}{b^2} = 1. \tag{3.29}$$

Under surface diffusion, the ellipse shape is going to evolve towards a circular shape while conserving its area. Thus limit radius, i.e. the limit value of a and b is given by the value $\sqrt{\pi ab} \approx 0.43416mm$.

The flow chart of Fig. 3.2 with $A = 0$ is implemented. A static mesh is used and an initial isotropic mesh adaptation is realized in a ring centered at (0,0) and defined as $0.19mm \leq r \leq 0.31mm$. This refined mesh area is defined to enforce a fine mesh size over the entire area crossed by the zero-isovalue of the LS during the simulation. The mesh size in this zone is defined by h. A description of one of the initial configuration of this case ($h = 1\mu m$) is given in Fig. 3.6 where we can observe: (a) the global mesh with the interface (red ellipse), (b) a zoom on the mesh, (c) the initial mean curvature field κ, (d) the initial $x-$component of the velocity field $v_s\vec{n}$ (see Eq. 3.6):

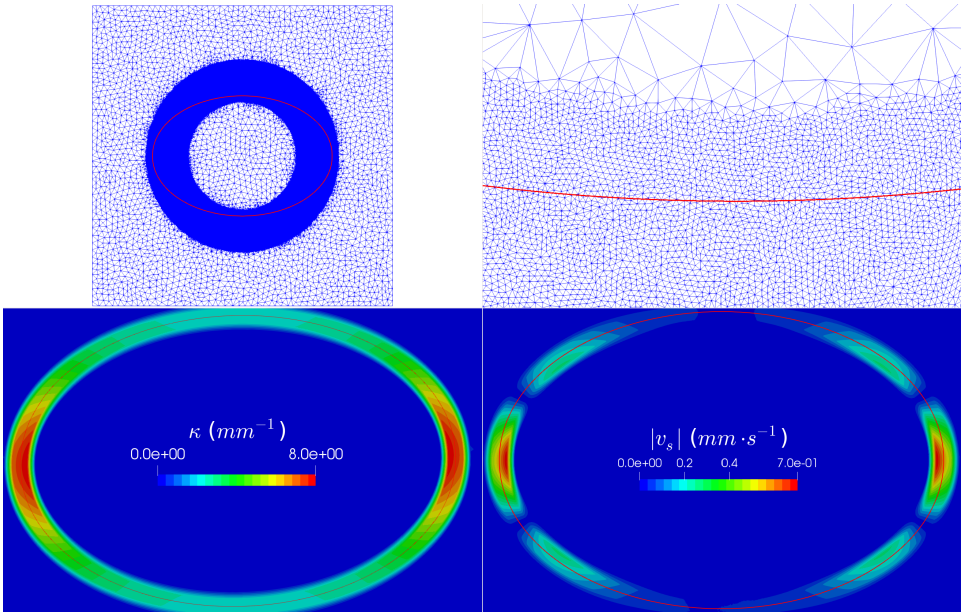

Figure 3.6: case 1 - Initial Configuration, from top to bottom and left to right: the global mesh, a zoom on the mesh, the initial mean curvature field κ and the initial norm of the velocity field $v_s\vec{n}$ (see Eq. 3.6). The ellipse interface is given by the red line in all the pictures.

The shape evolution of the numerical solution is compared to the exact solution [27]. The exact velocity of the point(a(t),0) can indeed be obtained by the following strategy:

$$\vec{v}_a\left(t\right) = B\frac{3(b^2-a^2)a}{b^6}\vec{i} = v_a\vec{i}, \tag{3.30}$$

with $\vec{i}$ the first basis vector of the cartesian coordinate system. Then, a(t+ dt) is approximated with an Euler forward scheme :

$$a(t+dt) = a(t) + dtv_a(t), \tag{3.31}$$

and by considering the area conservation, b(t+ dt) can be easily obtained with:

$$b(t+dt) = \frac{a(0)b(0)}{a(t+dt)}. \tag{3.32}$$

The coefficient B for all the chapter 3 simulations is set at 1e-3$mm^4 \cdot s^{-1}$. The mesh size in the finer mesh circle is $h = 1\mu m$ and the time step is $dt = 1ms$. The same time step and initial geometry is used for the analytical solution. Fig. 3.7 illustrates the comparison between the shape evolution of the analytical solution, represented by the blue line, and the numerical

one, represented by the red line, for the numerical approximation for t=0s, t=0.20s and t=1s. Taking a closer look at Fig. 3.7b, at time t=20s, a small difference between the two solutions can be observed.

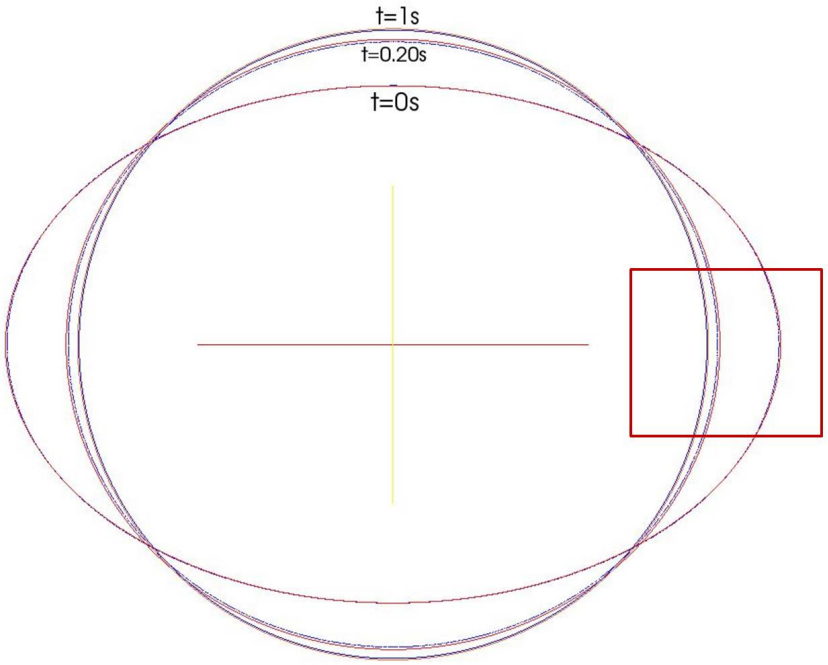

(a)

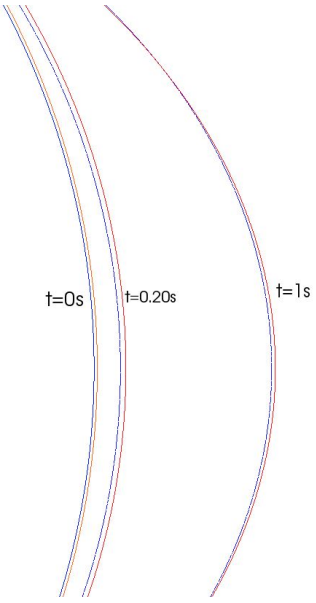

(b)

Figure 3.7: (a)Ellipse interface at 0s, 0.2s and 1s in blue for the analytical solution and in red for the LS methodology, (b) zoom.

The same simulation is performed on Eulerian framework with the same stable mesh but using a unified approach of convection + reinitialization, as it is detailed in [27]. Comparing these two formulations is of interest in order to investigate how efficient is the proposed Eulerian formulation/approach.

First, we have examined how the time step and the mesh size affect the response of our simulations and the corresponding precision of the results. The most important parameters regarding our study cases, the mesh size used in the refined zone, the time step, the CPU simulation time and finally the corresponding precision of the results obtained concerning the position of (a(t),0) in comparison with the solution, are summarized in Table 3.1. The errors have been defined as:

$$e_1 = \frac{\|a_{sim}(t) - a_{exact}(t)\|_{L1}}{\|a_{exact}(t)\|_{L_1}} = \frac{\Sigma_i \|a_{sim\,i} - a_{exact\,i}\|}{\Sigma_i \|a_{exact\,i}\|}, \tag{3.33}$$

$$e_2 = \frac{\|a_{sim}(t) - a_{exact}(t)\|_{L_2}}{\|a_{exact}(t)\|_{L_2}} = \frac{\sqrt{\Sigma_i (a_{sim\,i} - a_{exact\,i})^2}}{\sqrt{\Sigma_i {a_{exact}}^2}}, \tag{3.34}$$

where i denotes the time discretization.

Data	Case 1	Case 2	Case 3	Case 4
h in μm in the mesh refined zone	1	1	2	1
# Elt	∼2.7e5	∼2.7e5	∼7e4	∼2.7e5
Time step in ms	1	5	10	0.1
Convect+Direct Reinit	X	X	X	
Unified approach [27]				X
Calculation time using 12 CPU	1h	17 min	1 min	6h
e1 in % after 1s	2.5	2.6	2.1	2.2
e2 in % after 1s	3	3.1	2.9	2.8

Table 3.1: Ellipse under surface diffusion: comparisons between two Eulerian approaches for different numerical parameters and a static mesh.

Taking into account the first simulations summarized in Table 3.1, we can make the following remarks:

- in contrast with the unified approach of case 4 [27], our new approach with DR seems to reduce drastically the calculation time. This result illustrates the interest of the proposed direct renitialization procedure as already discussed in [32],
- for the first three simulations with the DR (cases 1,2 and 3) the variation in time step and mesh size does not affect significantly the e1 and e2 errors.

From these first tests, we have established that the new method of convection with DR is more efficient regarding the calculation time in comparison with a classical Hamilton-Jacobi resolution for the reinitialization. In the next section, we consider surface diffusion tests, using mesh adaptation techniques.

3.8.2 Tests on surface diffusion with mesh adaptation operations in an Eulerian approach

In this section, some first results are described regarding tests with surface diffusion on ellipsoids using the *a priori* mesh adaptation techniques described in section 3.6.1.2.

The initial geometry remains an ellipse of $a = 0.3mm$ and $b = 0.2mm$ axes, in a square domain $1mm \times 1mm$. We use the Eulerian approach with the convection + Direct Reinitialization algorithm. Mesh adaptation is performed at each time step.

Two different mesh adaptation metrics are tested. The considered metrics are calculated thanks to the method described in [31]. It enables us to obtain isotropic or anisotropic (in the normal direction of the interface) fine mesh at the vicinity of the interface. The definition of this metric is based on the distance function and is described in section 3.6.1.2. See Eqs. 3.25 and 3.26 for the anisotropic formulation and Eqs. 3.27 and 3.28 for the isotropic one.

Table 3.2 summarizes the results of several simulations. The most efficient mesh adaptation method is examined regarding the ellipse evolution and area conservation. For the latter,the area of the shape is measured at every time step and the loss is calculated with the following equation:

$$Area\,loss\% = 100 \cdot \frac{|Area_{t_{init}} - Area_{t_{final}}|}{Area_{t_{init}}}. \tag{3.35}$$

technique	Isotropic	Anisotropic
h in μm in the mesh refined zone	1	1
h_d in μm	10	10
E in μm	10	10
# Elt	∼9000	∼8000
Time step in ms	l	1
Convect+ Direct Reinit	X	X
Calculation time 12 CPU	2 min	2 min
Area loss % at t=1s	3.5	6

Table 3.2: Ellipse under surface diffusion: comparisons between two mesh metrics.

Initial meshes of Table 3.2 are presented in Fig. 3.8.

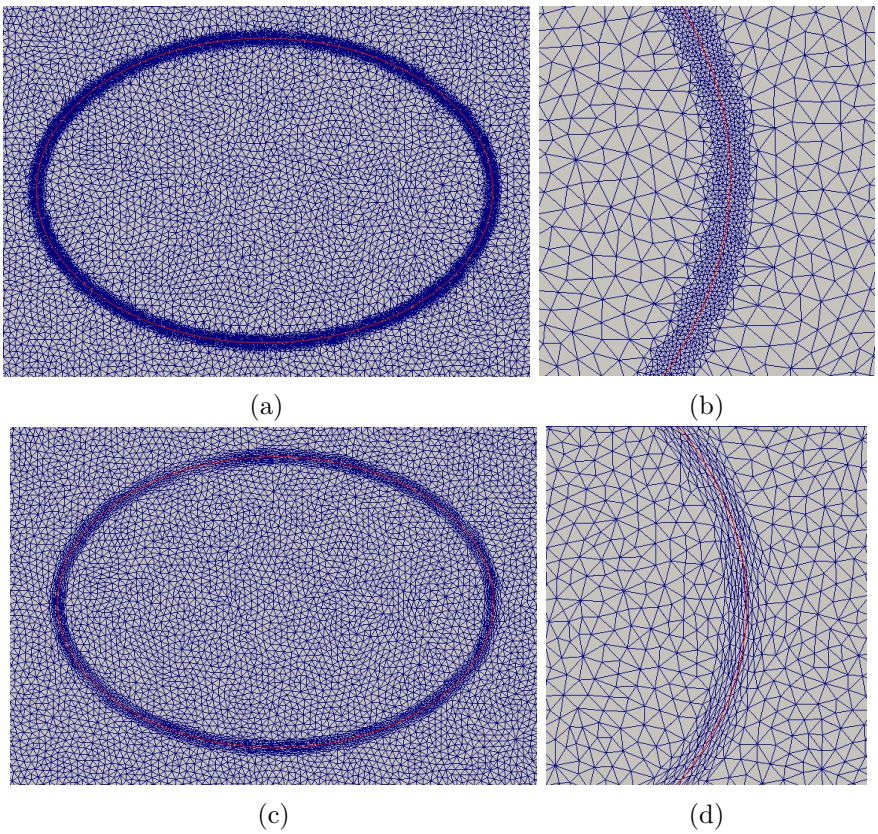

Figure 3.8: (a) Isotropic mesh adaptation, (b) zoom of (a), (c) Anisotropic mesh adaptation, (d) zoom of (c).

Taking into account Table 3.2, it seems that the time calculation has considerably decreased in comparison with the cases without mesh adaptation summarized in Table 3.1. The final shape of the ellipses in the two cases are circular. For the same time step and the same value of h at the refined area, isotropic refining seems to be more efficient in terms of volume conservation for a comparable calculation time. Furthermore, by making a comparison of the evolution of the axis for each case with the analytical solution (Eqs. 3.30, 3.31 and 3.32), the curves of Fig. 3.9 are obtained.

The a-value and the b-value should converge towards $R_{limit} \approx 0.2444 \mu m$. By comparing the axis evolution with the two different methods, the isotropic case seems to converge towards the analytical limit. For each of these two cases, there is an initial difference regarding the slopes of the curves.

Finally, regarding the shape evolutions during the simulations, it seems that the isotropic mesh adaption technique is much more appropriate for our simulations in comparison with the anisotropic one. The same analysis

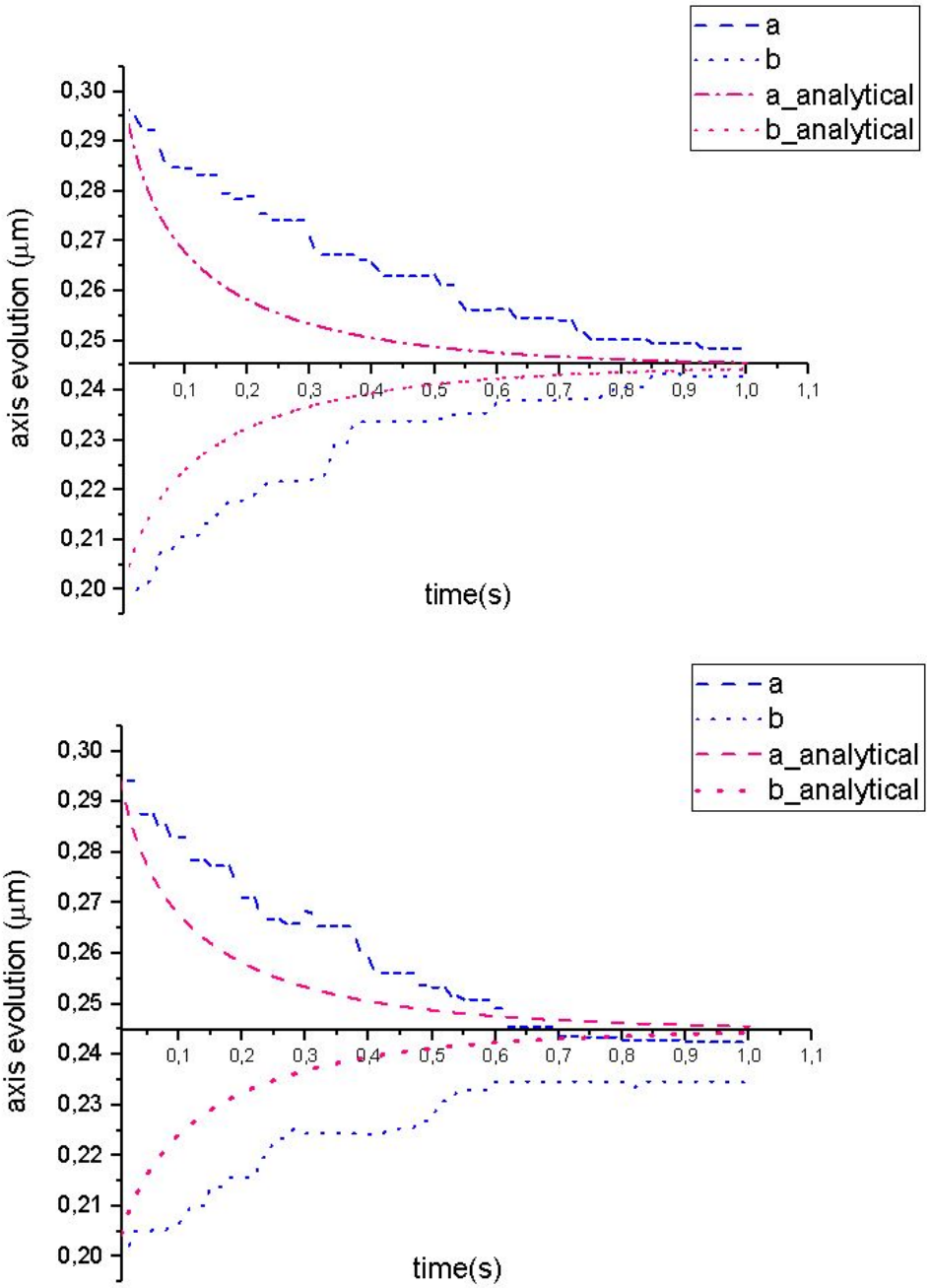

Figure 3.9: Radius axis evolutions during surface diffusion: (top) isotropic remeshing and (bottom) anisotropic remeshing.

was realized for different shape ratios of the initial ellipse, and the same conclusions were obtained. The idea of anisotropic mesh adaptation was then rejected since it seems that the volume loss is more important in comparison with the isotropic methodology.

Nevertheless, further tests have been made regarding mesh adaptation techniques but this time with the Lagrangian approach. More details regarding this subject are given to in following section.

3.8.3 Tests on surface diffusion with the Lagrangian approach using body fitted meshing and remeshing

Until now, only the Eulerian approach has been tested. In this section, we are going to illustrate some first academic cases concerning the enhanced Lagrangian approach that we have described in section 3.6.2.

Once again, we begin with simple tests regarding the shape evolution of ellipses under surface diffusion. For this case, we use exactly the isotropic metric described in the previous test case.

The geometry considered is an ellipse of $a = 0.5mm$ and $b = 0.1mm$ under surface diffusion as we have studied previously in context of the Eulerian approach in section 3.8.2. The case is presented in Table 3.3.

Data	Lagrangian approach
Mesh refinement	isotropic
h in μm in the refined mesh zone	1
h_d in μm	20
E in μm	20 μm
# Elt	∼20300
Time step in ms	5
Calculation time 12 CPU	3 min
Area loss at t=1s %	1.9

Table 3.3: Ellipse under surface diffusion: a Lagrangian calculation.

As illustrated by the results summarized in Table 3.3, the use of the proposed Lagrangian approach enables to limit the volume loss comparatively to the previous cases. The initial configuration of this case and the evolution of the 0-isovalue of the LS are described in Fig. 3.10, and Fig. 3.11.

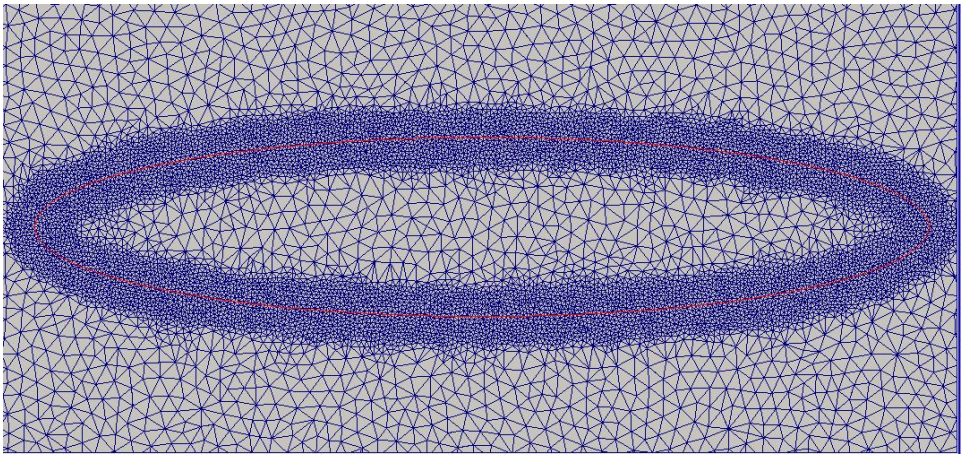

Figure 3.10: Lagrangian framework: initial configuration.

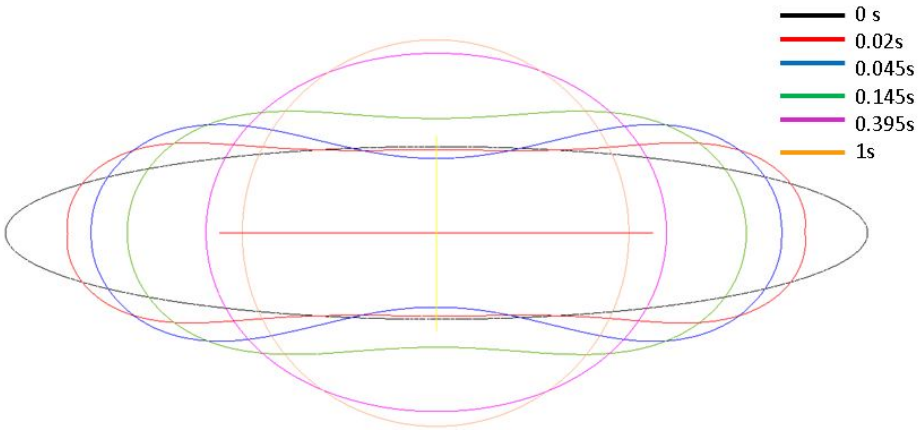

Figure 3.11: Lagrangian framework: time evolution of the 0-isovalue.

The improvement concerning the area conservation can also be explained by the increase of E (and therefore the number of mesh elements) considering in this case comparatively to the previous ones. Thus, to continue, a comparison between the Lagrangian and the Eulerian approach is made on a same configuration. A case of an ellipse with $a = 0.4mm$ and $b = 0.04mm$ axes (ratio of 10) is considered in a square domain $1mm \times 1mm$. It is a shape with higher curvature than the previous test cases and so this configuration is more realistic comparatively to the geometry of real α laths and more complex in terms of kinetics. Table 3.4 presents the two cases.

Data	Eulerian approach	Lagrangian approach
Mesh refinement	isotropic	isotropic
h in μm in the refined mesh zone	0.5	0.5
h_d in μm	20	20
E in μm	20 μm	20 μm
# Elt	~55000	~55000
Time step in ms	0.3	0.3
Convect+Direct Reinit	X	
Calculation time 12 CPU	13 min	13 min
Area loss at t=0.1s %	20	6

Table 3.4: Ellipse under surface diffusion: comparison between an Eulerian calculation and a Lagrangian one.

Isotropic mesh refinement is used for both cases. Time calculation for both cases is short even if the time step was fixed to the small value of $0.3ms$ in order to be precise on the comparison. Moreover a too large time step of thin elongated shape can lead to unrealistic split-off of the ellipse. The area conservation is clearly better with the use of the proposed enhanced Lagrangian framework as illustrated by Table 3.4 and the Figs. 3.12 and 3.13 which illustrate, respectively, the time evolution of the ellipse with the Eulerian approach and with the Lagrangian approach. With the chosen numerical parameters, we were not able to obtain a realistic interface motion thanks to the Eulerian approach.

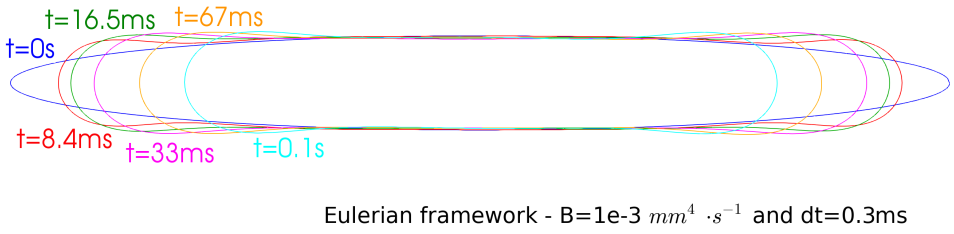

Figure 3.12: Eulerian method - Ellipse case - $a = 0.4mm$, $b = 0.04mm$.

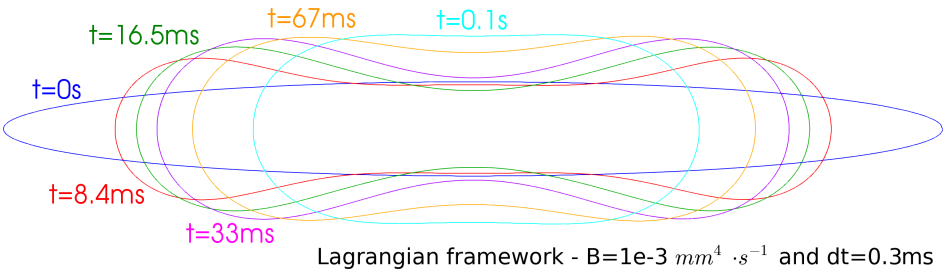

Figure 3.13: Lagrangian method - ellipse case - $a = 0.4mm$, $b = 0.04mm$.

From all the previous ellipses cases, we can conclude that the mesh adaptation techniques have facilitated the shortening of the computation time in both frameworks. Until now we have seen that the better volume conservation is obtained by using isotropic remeshing and the Lagrangian framework.

Another interesting case found in [27] is the motion by surface diffusion on a star shape. The star shape is formed by 3 ellipses with a ratio of 10 between the major and minor axis. B remains equal to 1e-3 $mm^4 \cdot s^{-1}$ and $dt = 0.5ms$. The same case with a "star" shape can be found in [25, 43].

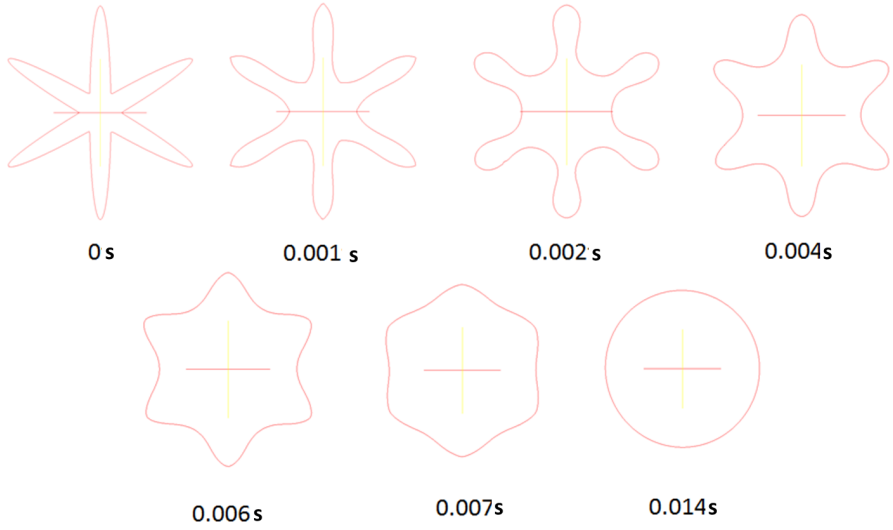

Figure 3.14: Eulerian approach - star shape evolution under motion by surface diffusion.

Data	Eulerian approach
mesh technique	isotropic
h in μm in the refined mesh zone	4
# Elt	∼13000
Time step in ms	0.1
Final time in ms	14
Convect+Direct Reinit	X
Calculation time 8 CPU	2 min
Area loss % at t=14ms	4.5

Table 3.5: "Star" shape case - Data for the Eulerian simulation.

Fig. 3.14 illustrates the shape evolution under surface diffusion with the Eulerian approach. Table 3.5 contains all the parameters of this test case. Shape convergence towards a circle is observed as expected from the literature [27, 43]. The final shape was reached after 150 iterations and the area loss at t=14ms is around 4.5 %.

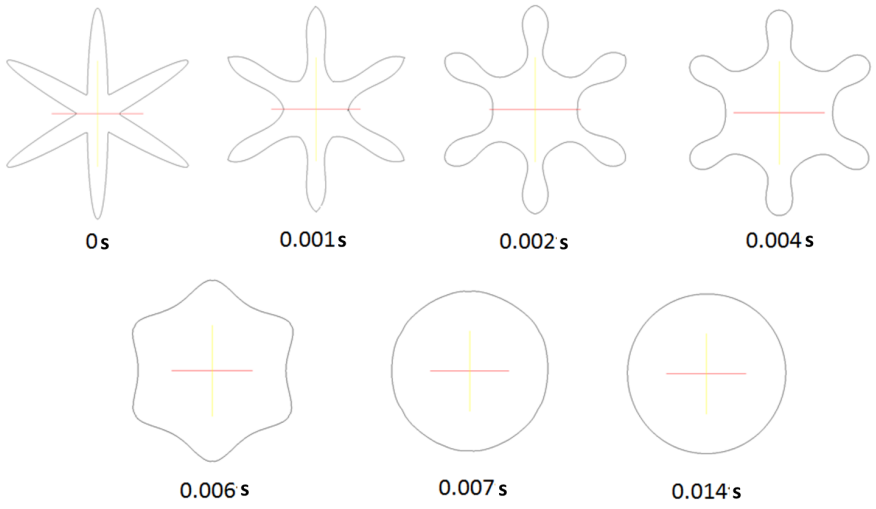

Figure 3.15: Lagrangian approach - star shape evolution under motion by surface diffusion.

Data	Lagrangian approach
Mesh refinement	isotropic
h in μm in the refined mesh zone	4
# Elt	∼14000
Time step in ms	0.1
Final time in ms	14
Convect+Exact Reinit	
Calculation time 8 CPU	2 min
Area loss % at t=14ms	2.4

Table 3.6: "Star" case - Data for the Lagrangian simulation.

Fig. 3.15, illustrates the shape evolution under surface diffusion with the Lagrangian approach. Table 3.6 contains all the parameters of this test case. As previously, the shape convergence to a circle is observed as expected. The final shape was also reached after 150 iterations and the area loss is around 2.4 %.

Both simulations seem to converge faster in the final shape than the one found in literature [27]. Since the totality of the parameters regarding this case study was not available, no safe conclusion can be made. Furthermore, main difference with [27] concerns the new Direct Reinitialization method (see section 3.5). Given a P1 representation of the LS function, the Direct Reinitialization gives a geometrical solution that is very accurate in comparison with other reinitialization methodologies. We are also able to obtain an exact description of the normal $\vec{n}$ (necessary for the calculation of the transport velocity) rather than following the classical way where the normals are computed by interpolation of the first derivative.

It is also important to highlight that, once again, the Lagrangian approach has smaller area loss than the Eulerian one (see Tables 3.6 and 3.5).

To conclude, in this section we have proved that both introduced numerical approaches are efficient for simulating surface diffusion. However, FITZ with the Lagrangian approach has given better results for all the calculation considered in the context of surface diffusion.

Thus, to complete our comparisons, it is important to examine and compare these two methodologies for motion by mean curvature in order to reach a final decision regarding what will be our final choice for simulating lamellae splitting.

3.8.4 Tests on motion by mean curvature

In the previous sections we have presented some results for testing our two approaches in context of surface diffusion. In this section, we are going to present results from simple cases simulating motion by mean curvature. Our

purpose again is to validate these results with literature cases and to decide which approach is more efficient for simulating the mechanisms of interest.

The first case performed is a sphere shrinkage case due to motion by mean curvature. We have chosen this case because the analytic solution is easily obtainable. To be more precise, the time evolution of a circle's radius $R(t)$ evolving thanks to motion by its mean curvature can be described by the Eq. 3.36:

$$\vec{v} = -A\kappa\vec{n} \rightarrow \frac{dR}{dt} = -\frac{A}{R} \rightarrow R\frac{dR}{dt} = -A \rightarrow \int_0^t \frac{1}{2}\frac{d}{dt}\left(R^2\right)\,dt = -\int_0^t A\,dt$$

$$\rightarrow \frac{R^2(t)}{2}|_0^t = -At \rightarrow R(t)^2 = R(0)^2 - 2At,$$

so the solution is:

$$R(t) = \sqrt{R(0)^2 - 2At}. \tag{3.36}$$

The Eulerian approach is first tested. As we have mentioned in previous sections, the flow chart of Fig. 3.2 is considered with a convective-diffusive formulation (see Eq. 3.23). The case is built on a square domain $1mm \times 1mm$ with a circle of initial radius of $0.2mm$. Fig. 3.16 shows, for $A = 0.1mm^2 \cdot s^{-1}$, the results obtained with an isotropic static mesh of mesh size $h = 2\mu m$ and $dt = 0.5\mu s$ and the comparison with the analytical solution (Eq. 3.36). The final error concerning the time of the circle disappearance is around 3%.

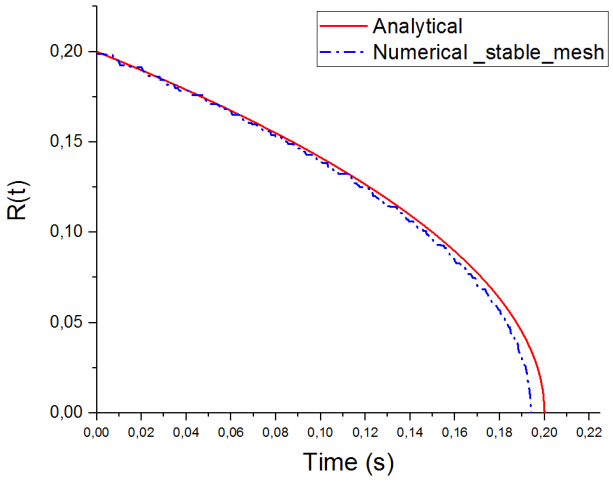

Figure 3.16: R(t) evolution (in mm) with motion by its mean curvature and static isotropic mesh ($h = 2\mu m$) thanks to the Eulerian framework.

A second comparison is done in the Eulerian framework using mesh adaptation. We use the isotropic mesh adaptation technique based on the metric that we have described in section 3.6.1.2. The mesh size at the remeshing area around the interface is fixed at $h = 1\mu m$ and the time step at $dt = 1ms$. The final error concerning the time of the circle disappearance is around 2.5%. Fig. 3.17 illustrates the comparison with the analytical solution.

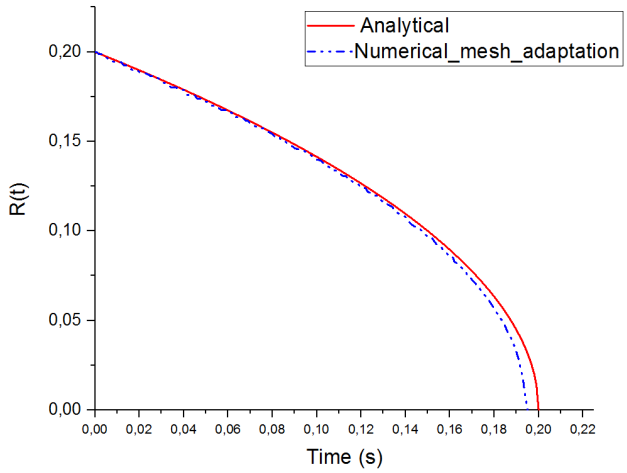

Figure 3.17: $R(t)$ evolution (in mm) with motion by mean curvature and isotropic mesh adaptation on the Eulerian methodology - $h = 1\mu m$ in the refined zone and $dt = 1\mu s$.

Our analysis continues with the same case in the Lagrangian framework by moving the mesh with the mean curvature velocity $\vec{v} = -A\kappa\vec{n}$. The mesh size at the remeshing area around the interface is fixed at $h = 2\mu m$ and the time step at $dt = 1ms$. Fig. 3.18 illustrates the comparison with the analytical solution. The final error concerning the time of the circle disappearance is around 1%.

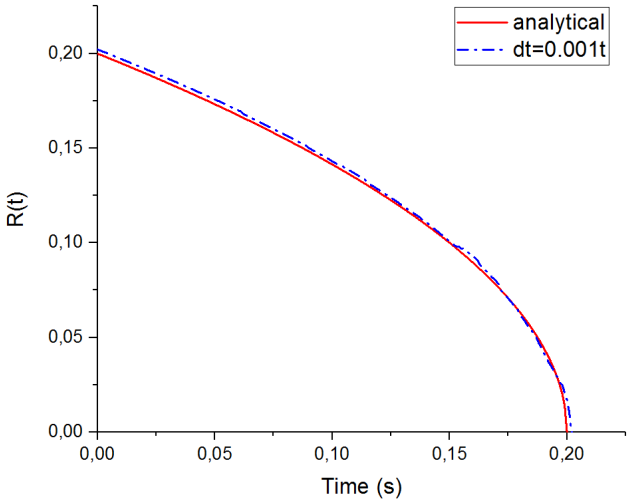

Figure 3.18: $R(t)$ evolution (in mm)with motion by mean curvature and isotropic mesh adaptation on the Lagrangian methodology - $h = 2\mu m$ in the refined zone and $dt = 1\mu s$.

From the analysis above and also from the L_2 calculation error of the $R(t)$ curves of the three previous simulations, we can conclude that the Lagrangian approach gives better results than the Eulerian one in this test case for equivalent numerical parameters.

The last test performed for testing the efficiency of motion by mean curvature in context of the Lagrangian approach is a triple junction configuration. Evolution of a T-junction due to mean curvature is presented using the proposed Lagrangian approach with body fitted meshing and remeshing. More specifically the geometry of the triple junction is defined by 3 different level sets as illustrated in Fig. 3.19. This configuration is largely discussed in [34] and [44].

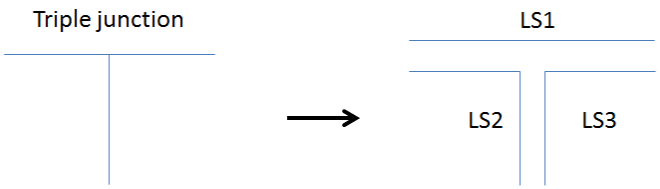

Figure 3.19: Scheme of the triple junction described with 3 LS functions.

For each level set the mean curvature κ and the mean curvature velocity

$\vec{v} = -A\kappa\vec{n}$, with $A = 0.1mm^2 \cdot s^{-1}$, are calculated using the (κ,v_s) identification solver. In order to move the mesh, the proposed methodology is to realize the half-sum of the three velocities and applied the resulting velocity to the grain boundary network.

Fig. 3.20 illustrates the body fitted mesh at $t = 0s$.

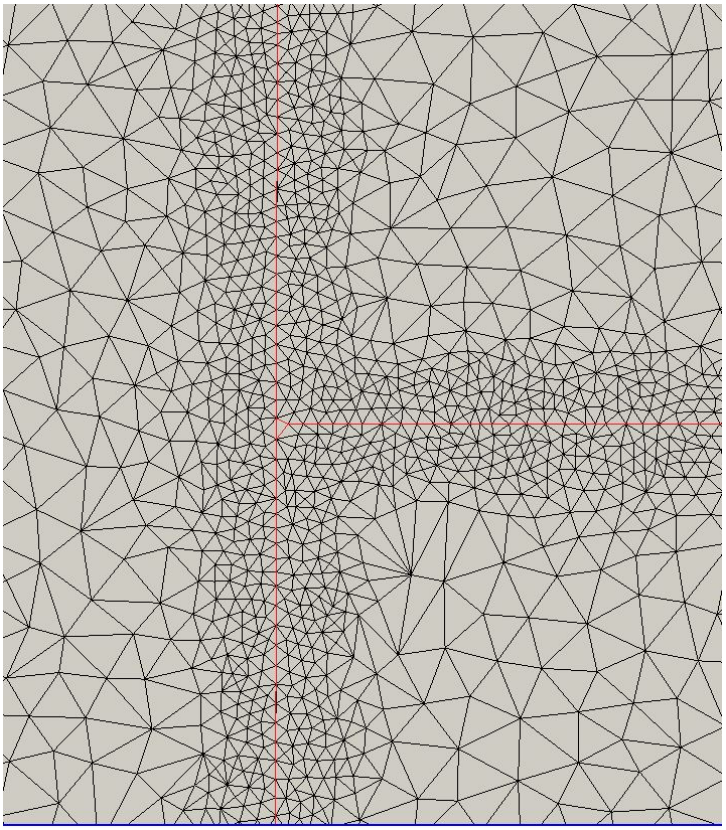

Figure 3.20: Body fitted mesh adaptation on the triple junction.

The simulation is performed with a time step $dt = 2ms$ and a final time $t = 2s$. The mesh size around the 0-isovalue is fixed to $h = 2\mu m$. The results are described in Fig. 3.21.

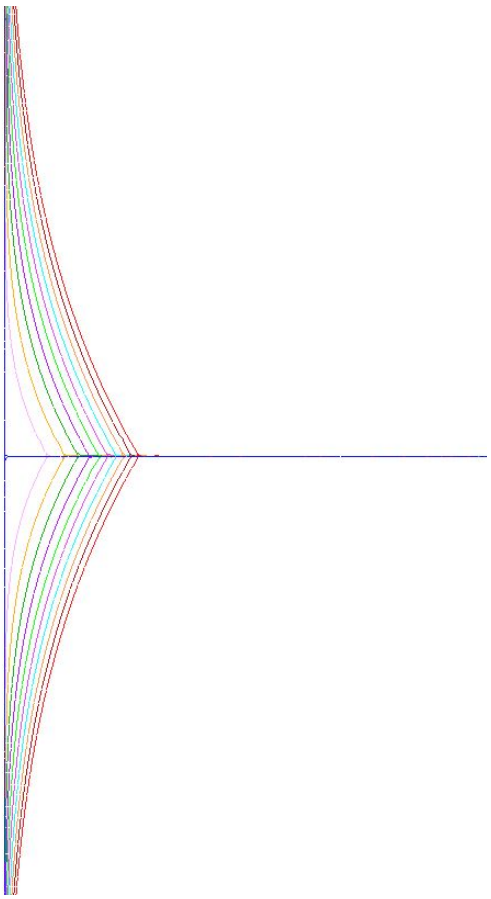

Figure 3.21: Time evolution of the T-junction. Blue and red lines are the triple junction at t=0s and t=2s respectively and intermediary colors from left to right correspond to the triple junction state at $t = 0.2i$ with $i \in \{1, \ldots, 9\}$.

Blue and red lines are the triple junction at t=0s and t=2s respectively. Intermediary lines from left to right correspond to the results at $t = 0.2i$ with $i \in \{1, \ldots, 9\}$.

Interestingly, the problem considered is totally equivalent to the problem of modeling grain growth with multiple junctions [34, 45]. The method proposed here (enhanced Lagrangian framework) constitutes a new promising numerical method for this kind of microstructure evolutions. This topic is currently studied by Florez et al. [46].

By considering the coefficient A as constant for the three interfaces, Herring's equation and Young's equilibrium should lead to the formation of equal equilibrium angles at the multiple junction between each interface [47]. Subsequently, the equilibrium angles of the triple junction should converge quickly at 120°.

In Fig. 3.21, it seems indeed that this condition is well respected. The angles at the triple junction were precisely measured from the results presented in Fig. 3.21 and the mean angle values are summarized in Table 3.7. The equilibrium is then perfectly respected during the simulation.

time	mean angle	error %
0.2 s	119.1	0.7
0.4 s	121.5	1.2
1 s	120.4	0.3
2 s	120.1	0.08

Table 3.7: Measures of the mean angle at the triple junction in Fig. 3.21.

The calculation was realized in 20 processors in 20 min. This example of T-junction is really important since this geometry is representative for the case of an α/α subboundary meeting an α/β interface. Nevertheless, in order to build a case representing the junction between α/α subboundaries and the α/β interfaces, the coupling of the surface diffusion velocity and the motion by mean curvature should be considered. In the next section, the sequence of steps followed in order to realize this calculation is presented.

3.8.5 Coupling motion by surface diffusion and motion by mean curvature

In the previous sections, the two methods (Eulerian and Lagrangian approaches) were validated for simulating separately the motions by surface diffusion and by mean curvature. Various academic cases have been examined and a conclusion was drawn regarding which approach is the most efficient for each case. For both motions described separately, the simulations following the Lagrangian approach with body fitted meshing and remeshing seems the most efficient. In this section, a last academic test case is considered to validate this choice. To simulate efficiently the lamellae splitting, we have to couple the motions due to surface diffusion and mean curvature. Driven from Derkach's work [19], the chosen configuration is two rectangles in contact in order to idealize an α lamella with an internal boundary as illustrated in Fig. 3.22, here two LS functions are considered. The dimensions of the rectangles are $0.3mm \times 0.05mm$ and they are embedded in a $1mm \times 1mm$ square domain. The used time step is $1ms$ and the physical coefficients are fixed as B =1e-6 $mm^4 \cdot s^{-1}$ and A =1e-3 $mm^2 \cdot s^{-1}$. The mesh size at the remeshed zone around the interface is fixed to $h = 1.6\mu m$.

Figure 3.22: An idealized lamella with an internal α/α interface.

With the Eulerian approach, as already mentioned, a P1 convection diffusion solver is used. In the convection diffusion equation the convective part simulates motion due to surface diffusion and the diffusive part simulates motion by mean curvature. Each motion is activated by defining areas around the interfaces where the coefficients are non zero in contrast with the rest of the domain (see Fig. 3.23 and Eqs. 3.7 and 3.8). The shape evolution is described in Fig. 3.24.

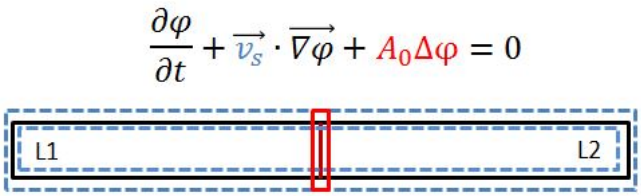

Figure 3.23: Eulerian approach: the blue-part corresponds to the part where surface diffusion is active whereas the red-part corresponds to the part where motion by mean curvature is active.

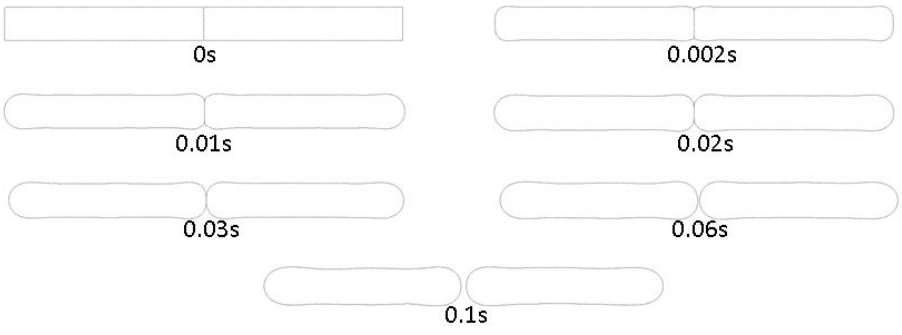

Figure 3.24: Academic case of lamella splitting with the Eulerian approach.

Lamella splitting due to surface diffusion and motion by mean curvature

is well observed after $0.1s$. The simulation was realized in 12 CPU in 26 min. However, an area loss of 8.5% is observed. Furthermore, oscillations around the interface appeared during the simulation after the splitting. The mesh around the interface is illustrated in Fig. 3.25.

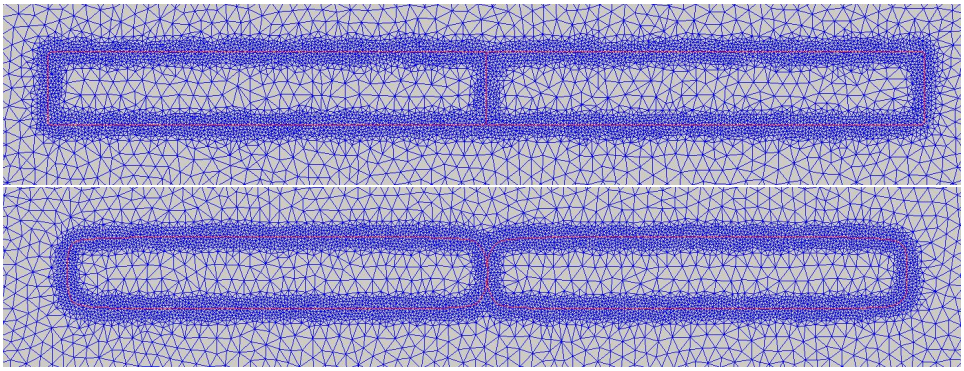

Figure 3.25: Mesh around the 0-isovalue at (top) t=0s, (bottom) t=4ms with the Eulerian approach.

The same case was realized in the Lagrangian approach. The two different velocities, defined by zone and calculated thanks to the two LS are added (with a factor 1/2 for the mean curvature part as counted twice) in order to move the mesh. Flow chart of Fig. 3.2 is then applied. Mesh and interfaces evolutions are described in Figs. 3.26 and 3.27. The area loss was limited to 6%, the calculation time in 12 CPUS was 18min and the split was observed after $0.118s$.

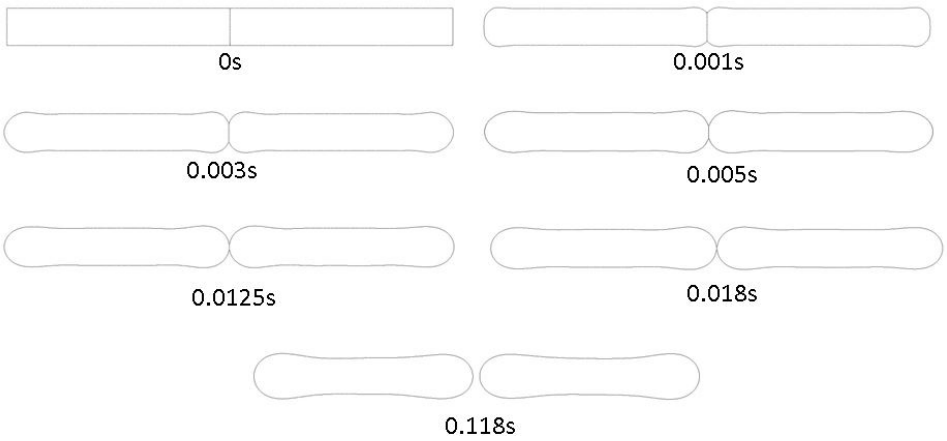

Figure 3.26: Academic case of lamella splitting with the Lagrangian approach.

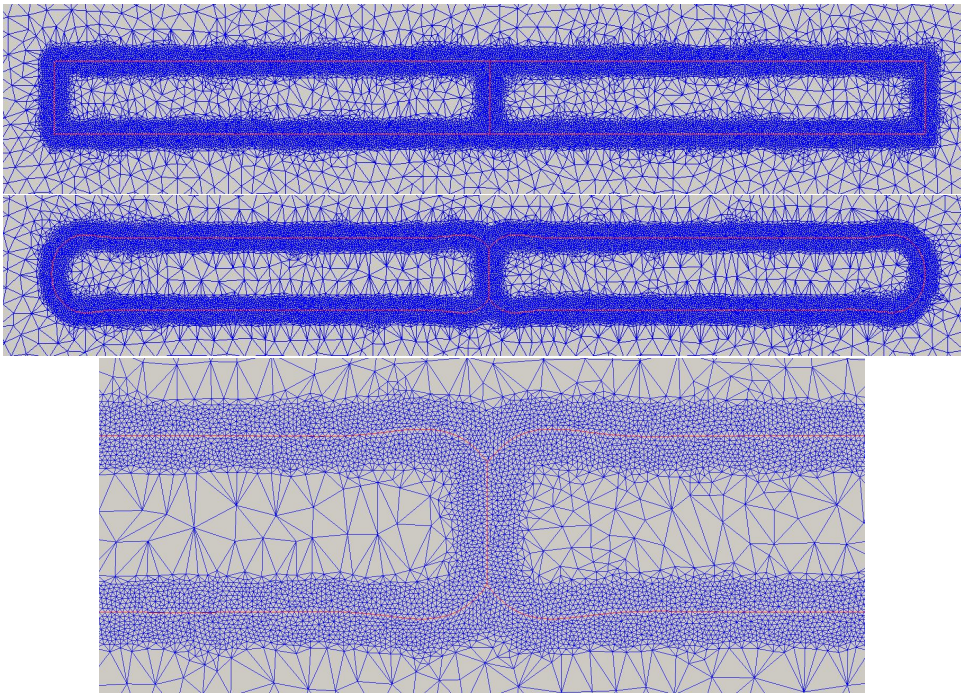

Figure 3.27: Mesh around the 0-isovalue - Enhanced Lagrangian framework: (top) initial mesh, (middle) mesh at $8ms$ and (bottom) zoom on the α/α subboundary at $t = 4ms$.

The comparison between the two methods for the case of lamellae splitting shows that in general the splitting occurs quicker with the Eulerian approach with, however, a lower initial kinetic. Moreover the area loss is more important. Regarding the calculation time the Lagrangian approach seems faster. Both approaches give very interesting results in all the tests that we have performed. To conclude, the more interesting method regarding volume conservation, time calculation and interface evolution is the enhanced Lagrangian framework approach. This method is the one selected for the following simulations. The difference observed concerning the time of splitting between the two approaches was not perfectly understood yet and will be investigated thoroughly in the future.

3.9 Conclusion

In this chapter, two full field methods were described and tested in order to simulate the mechanisms which lead to lamellae splitting. These two methods are based in several numerical tools developed in our C++ FE library called CimLib.

The first method takes place in an Eulerian framework where by providing the LS ϕ, the surface diffusion velocity is calculated using the (κ, v_s)-

identification solver. The LS is then updated by using a classical convective-diffusive solver. The diffusive part corresponds to the motion by mean curvature. The DR method is then performed in order to restore the metric property of the LS, followed by a remeshing operation. The second method takes place in an enhanced Lagrangian framework. The first step remains the calculation of the surface diffusion velocity and curvature with the (κ, v_s)-identification solver. The velocity, that couples velocities due to surface diffusion and motion by mean curvature, is constructed by calculating the two terms separately at the LS interfaces and adding them (with a factor 1/2 for the mean curvature part as counted twice). By updating the mesh, the LS is moved. Furthermore, a new topological mesher and remesher FITZ provides a conform mesh to the interface.

In comparison with literature, our method enables to model precisely surface diffusion and motion by mean curvature mechanisms in a unified numerical framework. The time calculation and precision seem reasonable in both cases.

After several tests simulating each of the two motions separately and coupled at the end, we have reached the conclusions that the enhanced Lagrangian method was better in terms of calculation time and area conservation. For these reasons this approach is adopted for the following simulations presented in the next chapter.

Chapter 4

Numerical simulations on real microstructures

Résumé en français

Dans ce chapitre, il est prouvé que la méthode numérique proposée permet de simuler efficacement les mécanismes physiques de migration interfaciale menant à la subdivision des lamelles et à l'évolution vers une forme globulaire, et ceci dans le cas d'une microstructure réelle extraite d'images expérimentales. Des efforts ont été faits pour estimer les coefficients physiques dans la méthode numérique proposée afin de réaliser des simulations en temps réel. Les coefficients ne pouvaient pas être aisément approchés car les paramètres matériaux ne sont pas connus dans la littérature scientifique. Des recherches plus approfondies doivent être effectuées l'avenir sur ce sujet afin d'améliorer la représentativit de nos simulations.

La simulation sur la microstructure réelle a donné de bons résultats concernant la conservation de surface pendant l'évolution de la forme et du temps de calcul, et ce indépendamment du nombre de lamelles traitées et de la taille du domaine. Pour cela, la méthode numérique proposée est une bonne base de départ pour ensuite développer un modèle numérique plus complet du phénomène de globularisation.

4.1 Simulating the spheroidization on real microstructures

In the previous chapters, all the responsible mechanisms for the phenomenon of spheroidization were presented as found in literature. Furthermore, some experimental results from hot compression tests performed during this PhD work, were described in detail. From these results, it was proven that motion by surface diffusion and motion by mean curvature are two mechanisms of great importance which can lead to the α lamellae splitting during the first stages of annealing. Following these results, we have presented and validated a new FE/LS methodology in order to simulate the phenomenon of α lamellae splitting at the lamellae scale.

Some academic test cases by the literature were discussed in the third chapter. In this chapter, more complicated configurations are presented in order to test the efficiency of the proposed methodology. Experimental images are considered and immersed in FE meshes in order to deal with realistic α laths geometries (see Fig. 4.1a). ImageJ software package was used for binarizing the image (see Fig. 4.1b) and extracting the signed distance functions of the α laths.

The ImageJ distance function was immersed (projection of the distance field to the FE mesh) into CimLib as initial geometry. The initial state described by Fig. 4.1(a) is representative of the experimental case described in Fig. 2.28 of Lx4 material after hot-compression at 1.34 strain and annealing for 15min at 950°C (see also Fig. 2.33(b) - second blue point). Immersion in FE mesh is realized by respecting the size and units of these experimental data. Moreover laths intersecting the boundaries of the calculation domain were removed in order to avoid numerical difficulties in the adopted enhanced Lagrangian framework.

4.2 Discussions for estimating material parameter values at $T = 950°C$

Since real microstructures were obtained and immersed as geometries for simulations, there is a need to clarify if and how laths spheroidization can be efficiently simulated in real time. As already mentioned in chapter 2, from literature and the experimental data, it is observed that interfacial kinetics are very slow and they are initiated during the first stages of thermal annealing. Only after long hours of annealing, evident spheroidization can be observed. Furthermore, the size of the lamellae of the initial microstructure is an important factor affecting the mechanism.

In our equations, the physical parameters are described by the coefficients B and A (see Eqs. 1.10 and 1.15). The B and A coefficients, as products of an interface energy and a mobility, are, respectively, the expres-

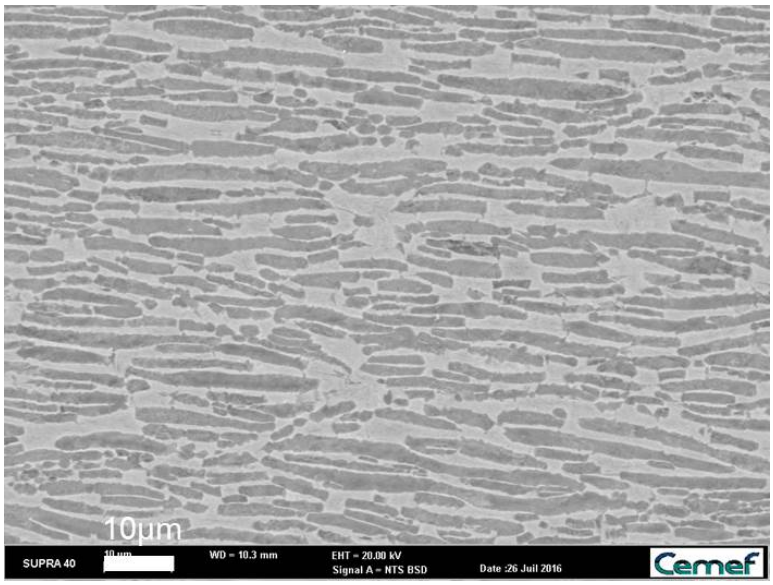

(a)

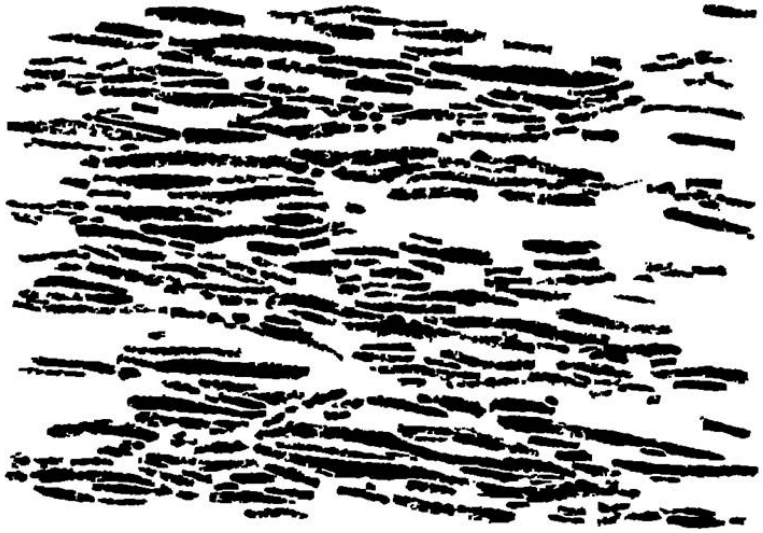

(b)

Figure 4.1: a) initial BSE micrograph image. b) Binarized microstructure extracted from experimental image a) by using ImageJ software.

sion of the thermodynamic and kinetic properties of the α/β interfaces and of the α/α sub-boundaries interfaces.

The following section is dedicated to discussions about representative values of these parameters.

4.2.1 Estimation of the B coefficient for motion by surface diffusion

In Mullins [11] and as described by Eq. 1.10, coefficient B is defined as:

$$B = \frac{\nu \gamma_{\alpha\beta} \Omega^2 D_{\alpha\beta}}{kT}, \tag{4.1}$$

with,

- $\gamma_{\alpha\beta}$ the energy of the interface between the two considered phases,
- ν the number of drifting atoms per unit area or density of the surface,
- Ω the atomic volume,
- $D_{\alpha\beta}$ the diffusivity of the interface between the two considered phases,
- $k \approx 1.38 \cdot 10^{-23} J \cdot K^{-1}$, the Boltzmann constant,
- T the absolute temperature.

From Semiatin article [21], we can identify for the considered material at $T = 1223K$ i.e. 950°C (our working experimental temperature):

- the molar volume [48], $V_m \approx 10440\, mm^3 \cdot mol^{-1}$,
- the surface energy [48], $\gamma_{\alpha\beta} \approx 0.4\, J \cdot m^{-2}$,
- the diffusivity defined as controlled by the vanadium atoms [49], $D_{\alpha\beta}(T) \approx 7.7 \cdot 10^4 e^{-17460/T(K)}$ i.e. at $1223K$, $D_{\alpha\beta} \approx 0.048\, \mu m^2 \cdot s^{-1}$.

We could not find a typical value in the literature regarding drifting atoms per unit area ν, as a commonly used coefficient does not seem to exist. In order to propose a rough approximation of the magnitude of this coefficient and how it can affect B, we assumed the following: the atoms diffuse in beta phase, that is body centered cubic (bcc), on the plane $< 110 >$. This plane has 4 sharing atoms and one central, meaning that we have 2 atoms on the whole square surface. Since the lattice constant α for body-center cubic titanium phase is α=0.3nm, we obtain for ν:

$$\nu = \frac{2}{\alpha^2 \sqrt{2}} = \frac{2}{9 \cdot 10^{-14} \sqrt{2}} \approx 1.57 \cdot 10^{13} mm^{-2}. \tag{4.2}$$

The molar volume ($V_m \approx 10440\, mm^3 \cdot mol^{-1}$) enables to calculate the atomic volume:

$$\Omega = \frac{V_m}{N_A} = \frac{10440}{6.022 \cdot 10^{23}} \approx 1.73 \cdot 10^{-20} mm^3, \tag{4.3}$$

with N_A the Avogadro number. Substituting these values in Eq. 4.1, we obtain:

$$B = \frac{(1.57 \cdot 10^{13} \frac{1}{mm^2}) \cdot (0.4 \cdot 10^{-6} \frac{J}{mm^2}) \cdot (1.73 \cdot 10^{-20} mm^3)^2 \cdot (0.048 \cdot 10^{-6} \frac{mm^2}{s})}{1.38 \cdot 10^{-23} \frac{J}{K} \cdot 1223K}$$
$$\approx 5.35 \cdot 10^{-9}\, \mu m^4 \cdot s^{-1}.$$

4.2.2 Estimation of the A coefficient for motion by mean curvature

In the work of Mullins [11] and in the domain of grain growth modeling [47], the A coefficient describing the motion by the mean curvature is expressed as follow:

$$A = \underbrace{M\,(T)}_{\frac{bf\Omega}{kT} * e^{-\frac{[\![E]\!]}{kT}}} \quad \gamma_{\alpha\alpha} = \frac{\gamma_{\alpha\alpha} bf\Omega}{kT} e^{-\frac{[\![E]\!]}{kT}} = \frac{\gamma_{\alpha\alpha} bf\Omega}{kT} e^{-\frac{Q}{RT}}, \tag{4.4}$$

where M is defined as the grain boundary mobility, $\gamma_{\alpha\alpha}$ denotes the energy of the α/α interfaces, b is the burgers vector norm associated with hoping event, f the Debye frequency, R the gas constant, and $[\![E]\!]$ the difference between the free energy of the two grains [2, 11, 19]. $[\![E]\!]$ is linked to the activation energy Q by the relation $[\![E]\!] = Q/N_A$ as k with R.

From literature [2, 11, 19] we can obtain:

- a typical value for the burgers vector norm $b \approx 0.26nm$,
- a typical value for the Debye frequency $f \approx 1.45 \cdot 10^{13}\, s^{-1}$,
- from Semiatin [2], we found $Q \approx 160\, kJ \cdot mol^{-1}$ and $\gamma_{\alpha\alpha} \approx 0.4\, J \cdot m^{-2}$.

Concerning the $\gamma_{\alpha\alpha}$ coefficient, from Herring's relation [12, 13], we know that the expression $2\gamma_{\alpha\beta} cos\delta/2 = \gamma_{\alpha\alpha}$ (see Fig. 1.7 and Eq. 1.1) [50, 51], denotes a relation between the energy of the α/β interface and the energy of the subboundary verified where the groove appears. By assuming moreover that $\gamma_{\alpha\alpha}$ can't be larger than $\gamma_{\alpha\beta}$, the minimum dihedral angle that we can obtain is $\delta = 120°$ for which $\gamma_{\alpha\alpha} = \gamma_{\alpha\beta} \approx 0.4J \cdot m^{-2}$. We could assume that this approximation is the upper bound of the $\gamma_{\alpha\alpha}$ value. Indeed this parameter is usually related to the misorientations observed at these

subboundaries [47, 52]; then the low misorientations observed in chapter 2 implies probably lower values of this parameter. Finally, for the sake of simplicity, the value $\gamma_{\alpha\alpha} \approx 0.4J \cdot m^{-2}$ will be used as following. So A can be approximated with the following calculations:

$$A \approx \frac{4 \cdot 10^{-7} \frac{J}{mm^2} \cdot 2.6 \cdot 10^{-7} mm \cdot 1.73 * 10^{-20} mm^3 \cdot 1.45 \cdot 10^{13} s^{-1}}{1.38 \cdot 10^{-23} \frac{J}{K} \cdot 1223K} \cdot e^{-\frac{1.6 \cdot 10^5 \frac{J}{mol}}{8.3145 \frac{J}{mol \cdot K} \cdot 1223K}}$$

$$A \approx 2.27 \cdot 10^{-1} \mu m^2 \cdot s^{-1}.$$

4.2.3 Conclusions regarding the A and B coefficients

The following remarks can be done concerning the order of magnitude obtained for coefficients A and B. To begin with, the value of A is in agreement with existing data discussed in the literature [11,19,53]. On the other hand, discussions regarding the coefficient B are limited in the literature concerning the spheroidization phenomenon. In our estimation, which was obtained by using typical values found in the work of Semiatin et al. [21,49], the order of magnitude of $B \approx 10^{-8} - 10^{-9} \mu m^4 \cdot s^{-1}$ is far from the order of magnitude found in Mullins [11] or Derkach [19] $\approx 10^{-4} \mu m^4 \cdot s^{-1}$. That can be easily explained by the fact that both Mullins and Derkach work deal with the phenomenon of grooving at free surfaces where the diffusivity coefficient is generally estimated around $10^3 \mu m^2 \cdot s^{-1}$ while in our case diffusivity is $D_{\alpha\beta} \approx 0.048\, \mu m^2 \cdot s^{-1}$ at $1223K$.

In the next sections simulation results are presented using geometries extracted from real microstuctures where the determined coefficients are used.

4.3 Motion by surface diffusion on an immersed microstructure

4.3.1 Lx4 material

In this section, simulations of surface diffusion on immersed geometries from microstructures extracted from experimental images are presented. The purpose is to test the efficiency of the adopted methodology (Lagrangian framework using (κ, v_s)-identification solver and FITZ).

The procedure followed is more or less the same as the one of the academic test cases for the surface diffusion discussed in Chapter 3. Fig. 4.2 displays the immersed microstructure of Fig. 4.1 in the considered FE mesh, the size of the simulation domain is $200\mu m \times 120\mu m$ (with an experimental image of $180\mu m \times 100\mu m$). The number of α laths treated is 165. All the α laths are expressed with only one common LS function.

The conform mesh at the interface obtained with the use of FITZ is one of the advantages of the Lagrangian methodology. In Fig. 4.2 we can observe the conform mesh around the 0-isovalue, with a global view on Fig. 4.2(a) and with a zoom on some laths on Fig. 4.2(b). The number of elements used is around 270000 with an isotropic mesh refinement around the laths (mesh metric defined with Eqs. 3.27 and 3.28). The maximum mesh size is $h_d = 1\mu m$, while the minimum mesh size around the interface is $h = 0.2\mu m$ and $E = 1\mu m$. Here the thickness used to define $\tilde{\phi}$ is different from E and is equal to $0.3\mu m$. The initial functions ϕ and $\tilde{\phi}$ are described in Fig. 4.3.

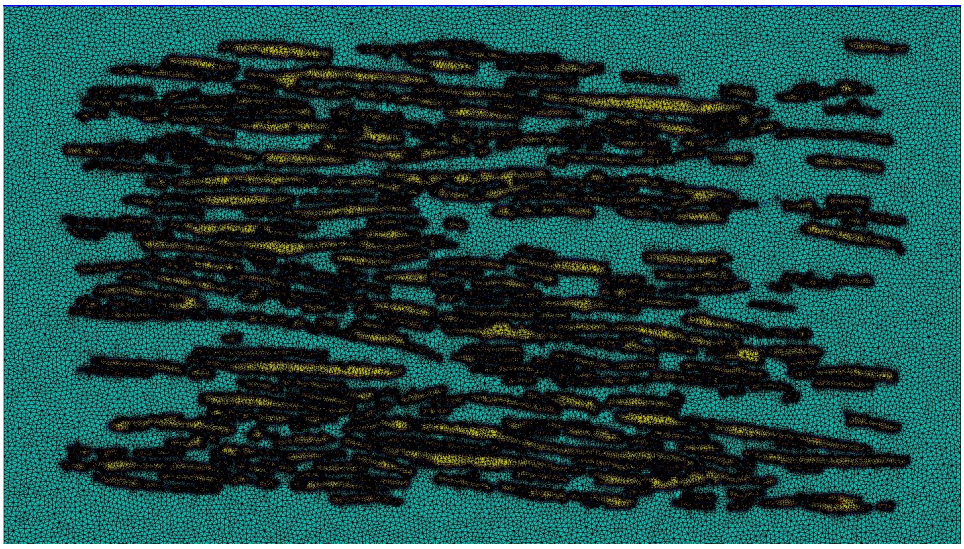

(a) Global mesh

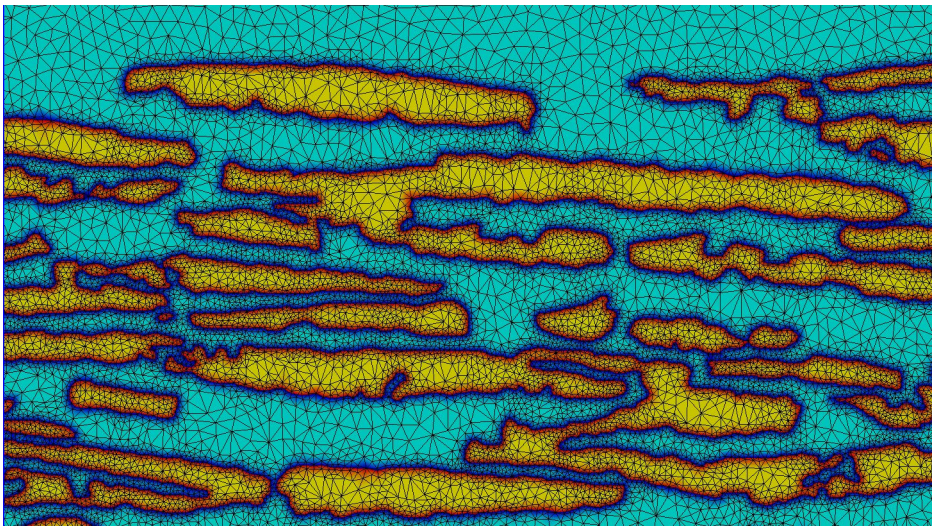

(b) Zoom

Figure 4.2: Conform mesh adapted to the experimental image.

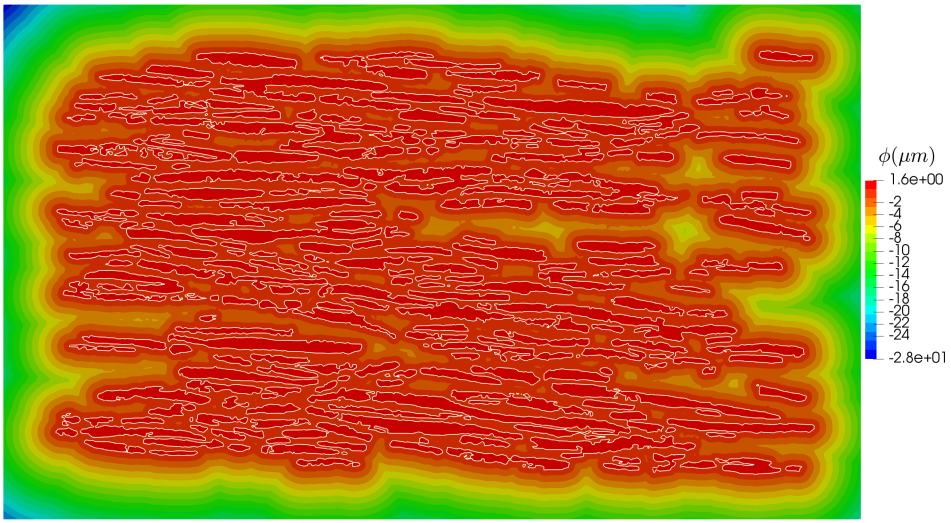

(a) immersed microstructure - distance field ϕ (μm)

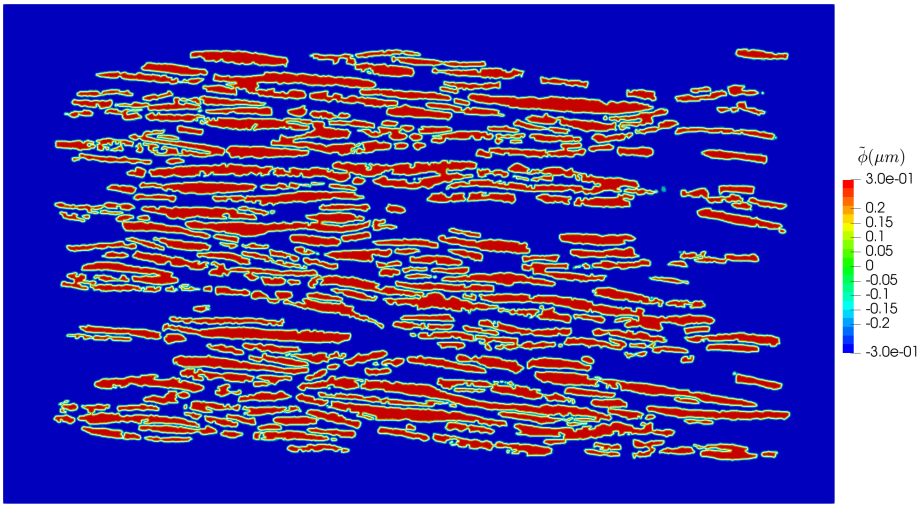

(b) filtered distance - $\tilde{\phi}$

Figure 4.3: LS functions: (top) ϕ and (bottom) $\tilde{\phi}$. White lines correspond to the lamellae/laths interfaces.

As detailed in Fig. 4.4, the velocity field is evaluated only in the thickness used to build $\tilde{\phi}$. Comparatively to the velocity scale, the time step dt was fixed to $12h$. The simulation was realized in 20mins in 24 CPUs. Fig. 4.5 illustrates the time evolution of the microstructure.

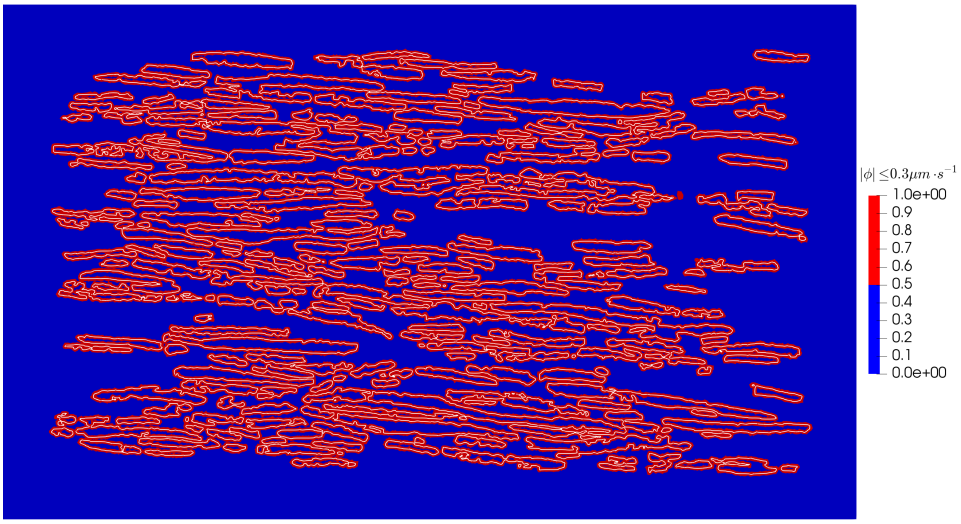

(a) Zone where the surface diffusion field is considered

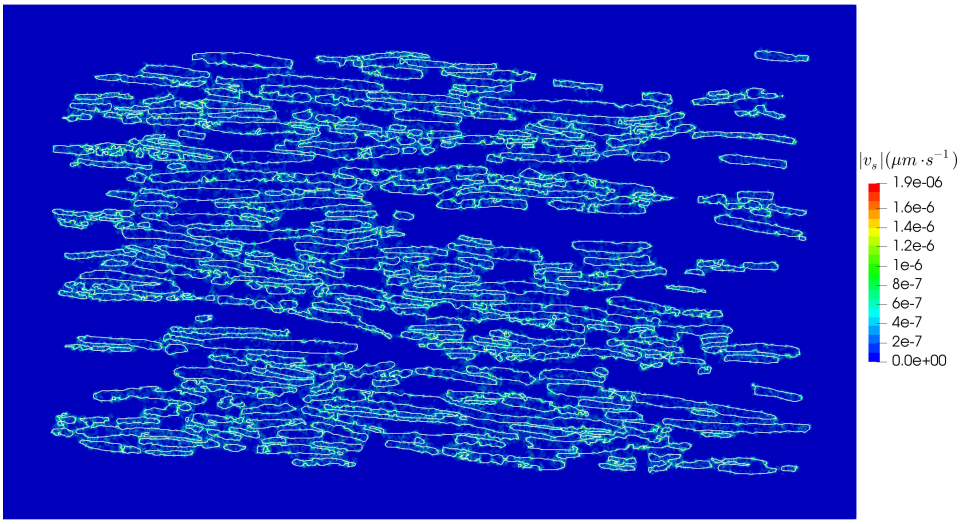

(b) Norm of the Lagrangian velocity ($\mu m \cdot s^{-1}$)

Figure 4.4: Illustration at $t = 0s$ of the velocity field.

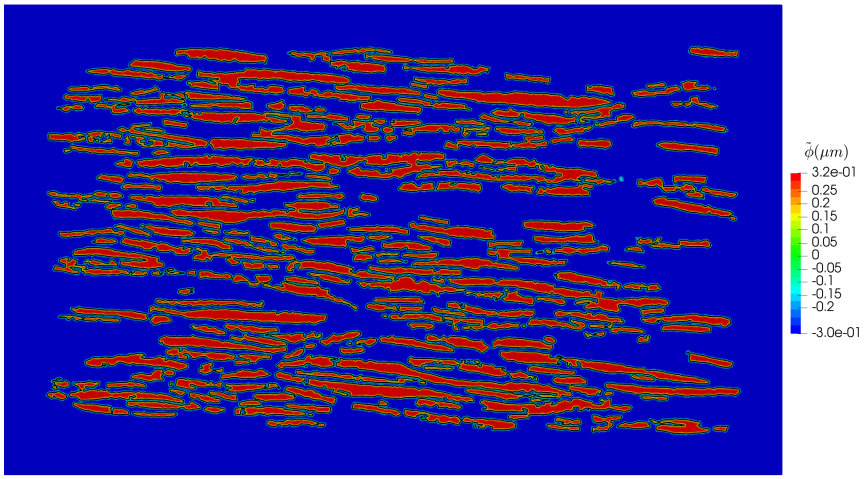

(a) $t = 0s$

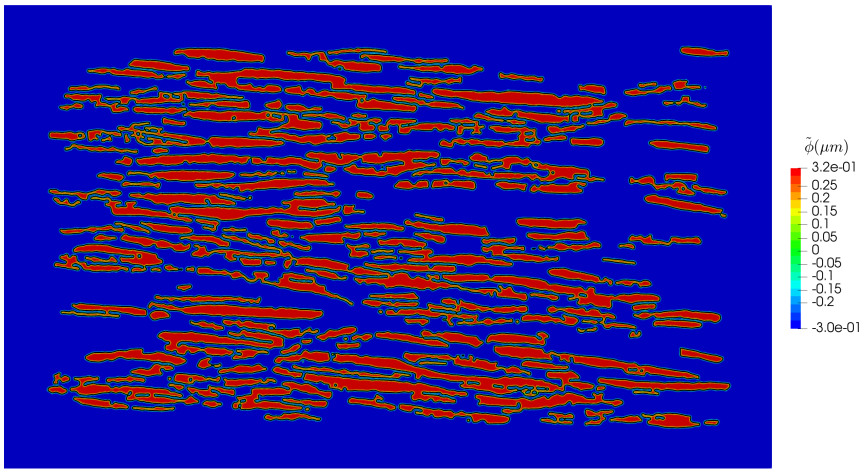

(b) $t = 10days$

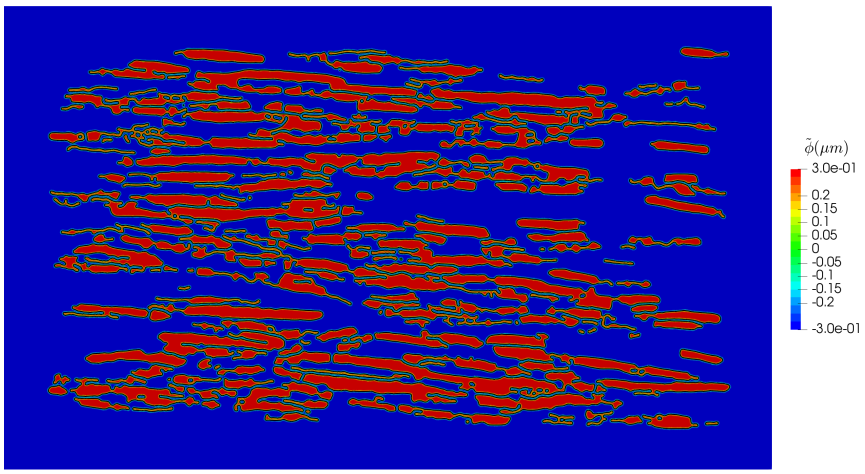

(c) $t = 50days$

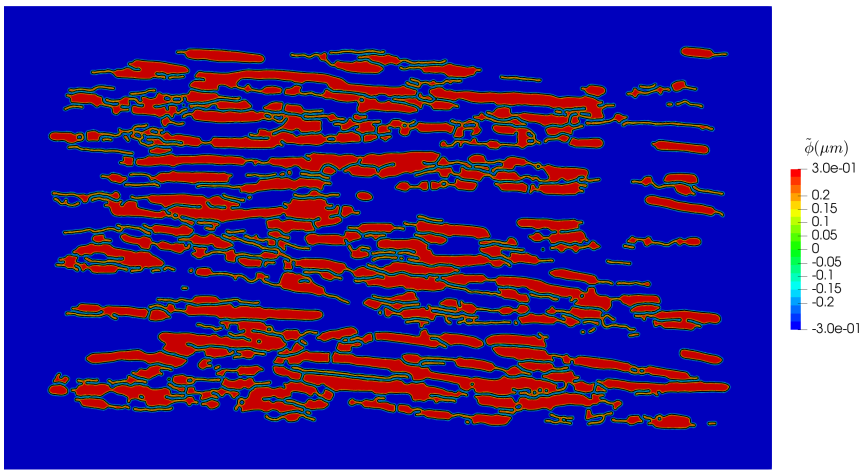

(d) $t = 100days$

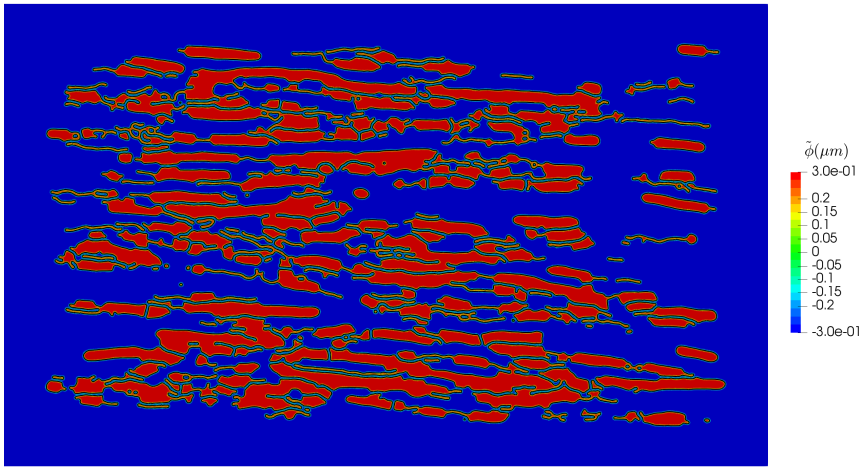

(e) $t = 200days$

Figure 4.5: α Microstructure evolution - Function $\tilde{\phi}$ with black lines for the lamellae/laths interfaces.

Microstructural evolution from the initial elongated shape of the particles to more circular ones is observed. Area loss until the end of the simulation is limited to 1.75% at t = 200days. From this simulation we can make the following remarks:

1. shape evolution of long isolated lamellae/laths is coherent with surface diffusion mechanism,
2. the smaller particles tend to evolve faster towards a spheroidal shape,
3. volume conservation is very well verified,

4. some lamellae/laths have numerically merged,

5. the global kinetic is very low comparatively to experimental results described in Fig. 2.33(b).

Regarding remark 5., the unrealistic numerical kinetics can be explained by the fact that our simulation is more representative of a static spheroidization phenomenon with large lamellae without the presence of a α/α sub-boundaries. Indeed, it is well known that static spheroidization without pre-deformation can lead to very low evolution of the microstructure. Moreover, in such context, additional mechanisms should be taken into account (coarsening, phase transformation etc.) as they are described in chapters 1 and 2. The fast evolution observed in Fig. 2.33(b) in terms of spheroidization during the first hour of thermal treatment can be explained by the presence of numerous α/α interfaces inside the lamellae enabling their fragmentation in smaller laths evolving faster to spheroidized shape.

Finally remark 4. illustrates the limit to use only one level set function for all the lamellae/laths leading to numerical coalescence when contact occurs. In section 4.4, we will illustrate how this weakness can be solved. The study that was realized for Lx4 material was also realized for the Lx2 material and the results are discussed in the following section.

4.3.2 Lx2 material

A new immersed microstructure coming from the Lx2 material is considered. The size of the simulation domain is $205\mu m \times 100\mu m$ (with an experimental image of $195\mu m \times 90\mu m$). All the α laths are expressed with only one common LS function. As for the previous test case, this initial state was obtained after hot-compression at 1.34 strain and 15min of thermal treatment at 950 °C/ $1223K$. Fig. 4.6 illustrates the global evolution with time and the conclusions are similar to the previous Lx4 microstructure. The time step dt was fixed to $6h$. The simulation was realized in 28mins in 24 CPUs. Finally the alpha area loss was limited to 3% at $t = 200days$.

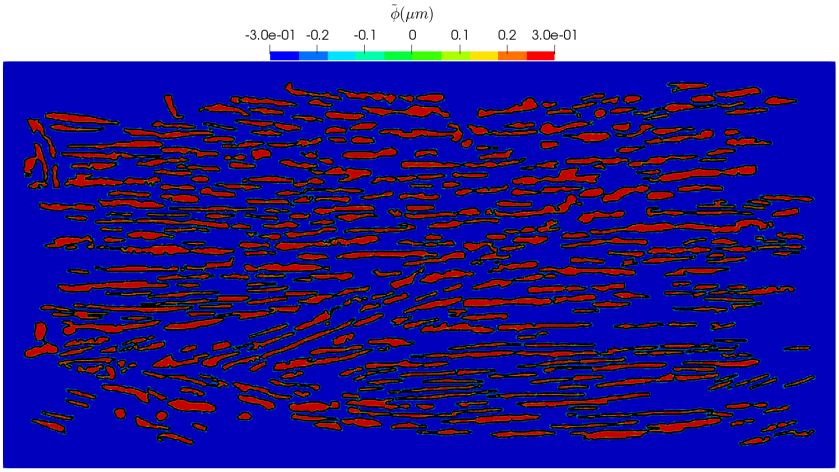

(a) $t = 0s$

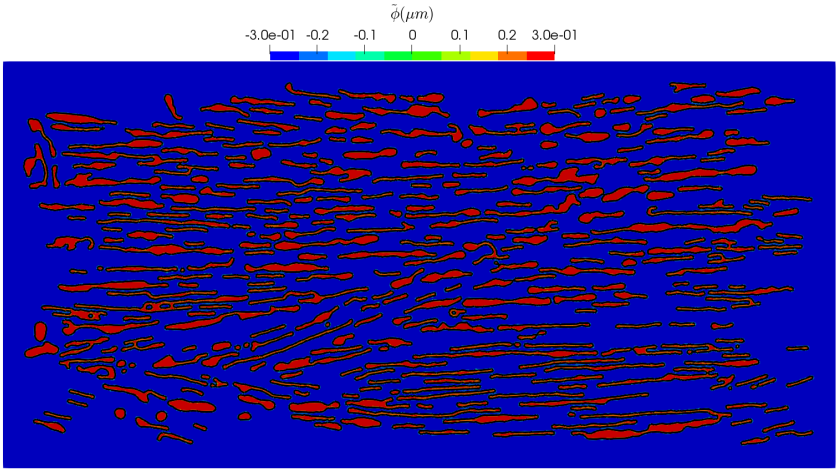

(b) $t = 50days$

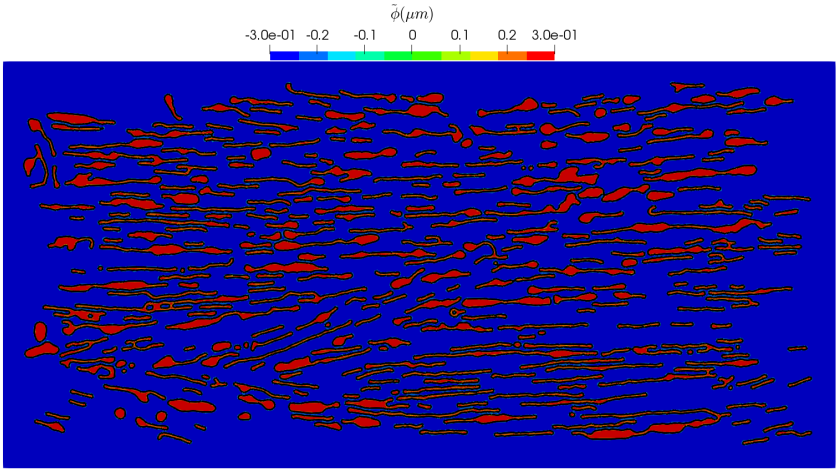

(c) $t = 100days$

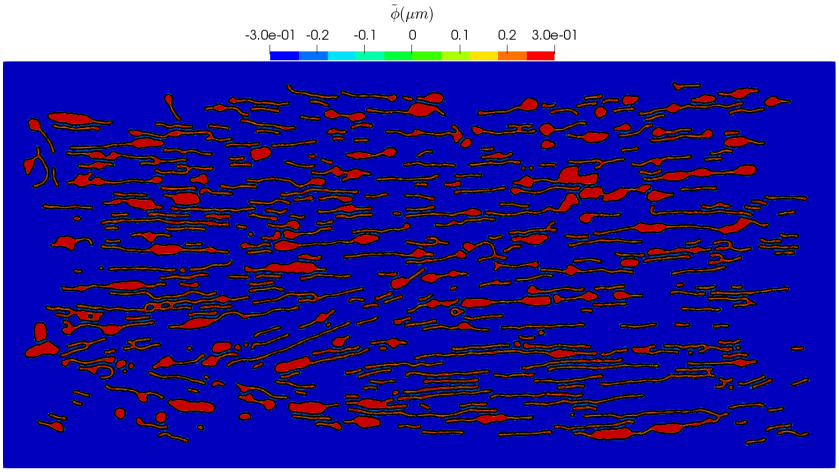

(d) $t = 200 days$

Figure 4.6: α microstructural evolution - function $\tilde{\phi}$ with black lines for the lamellae/laths interfaces.

4.4 Coupling motion by surface diffusion and motion by mean curvature

The previous simulations have shown that the proposed methodology enables to respect area conservation of each phase. Furthermore, the lamellae/laths shape evolution is coherent with an evolution towards more spheroidal shapes with very slow motion as illustrated by the Fig. 4.7 which describes the quasi steady-state obtained for the test case of Fig. 4.6. However, one of the weaknesses of the previous simulations, as clearly illustrated by Fig. 4.7, is that laths merging can occur, something that does not correspond with experimental observations.

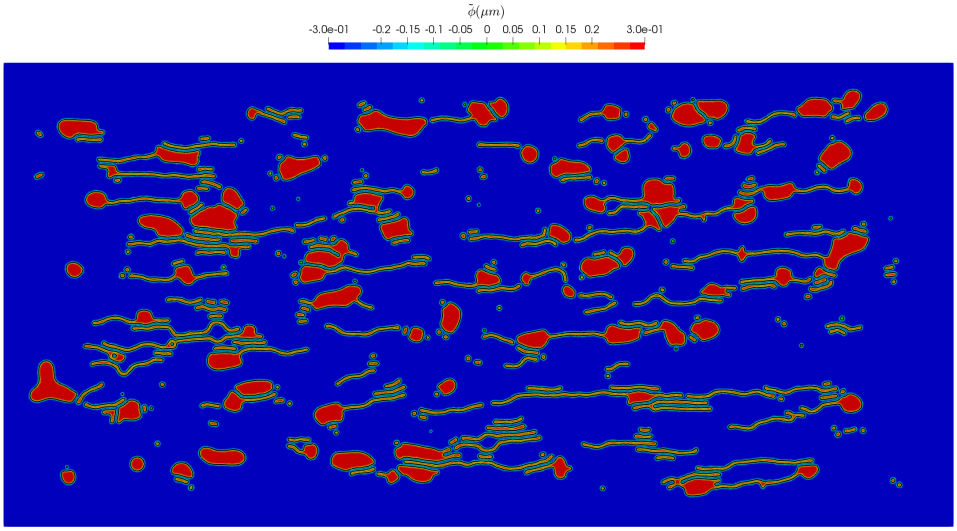

Figure 4.7: Quasi steady-state of the Fig. 4.6 test case.

As we have already mentioned when studying the physics of the phenomenon, lamellae/laths in contact keep their boundary. The challenge is then to simulate a realistic boundary evolution between two evolving laths in case of contact. When such interfaces come in contact, physically α/α interfaces must be taken into account in the global kinetic. In chapter 3, we have shown that we were able to couple motion by mean curvature and motion by surface diffusion in some simple cases. Now, we are going to perform simulations coupling these two motions in the considering geometry of section 4.3. With the coupling of these two mechanisms we expect to obtain a more realistic shape evolution of the lamellae/laths.

The concept of coupling these two mechanisms was described in section 3.8.5 and is recalled below:

- the Lx2 microstructure describes in Fig. 4.6(a) is considered,
- we index the different initial lamellae/laths by using a model [33] that enables to identify separately the different connected components (see Fig. 4.8),
- each separated lamella/lath is described by one distance function, that we will denoted as ϕ_i, obtained thanks to direct reinitialization of the belonging field to the corresponding connected components,
- for each distance function we calculate the surface diffusion velocity $\vec{v}_{s_i} = B\Delta_s\kappa_i\vec{n}_i$ and the curvature κ_i which is used in order to calculate the mean curvature velocity $\vec{v}_{\kappa_i} = -A\kappa_i\vec{n}_i$,

- we define the applied velocity areas for surface diffusion and mean curvature separately, $\vec{v}_{s_i} = B\Delta_s\kappa_i\vec{n}_i\chi_{\alpha\beta_i}$ and $\vec{v}_{\kappa_i} = -A\kappa_i\vec{n}_i\chi_{\alpha\alpha i}$, with $\chi_{\alpha\beta_i}$ and $\chi_{\alpha\alpha i}$ the characteristic functions, respectively, of α/β and α/α interfaces,

- at the end we add all the different velocities of each lamella/lath at one global velocity which is used in the considered enhanced Lagrangian framework. The mean curvature velocity contribution of the concerned distance functions at α/α interfaces, is divided by a factor of 2 (because counted twice) in the global kinetic:

$$\vec{v}\,(x,t)_{global} = \sum_i \left(B\Delta_s\kappa_i\vec{n}_i\chi_{\alpha\beta_i} - \frac{A}{2}\kappa_i\vec{n}_i\chi_{\alpha\alpha i} \right). \tag{4.5}$$

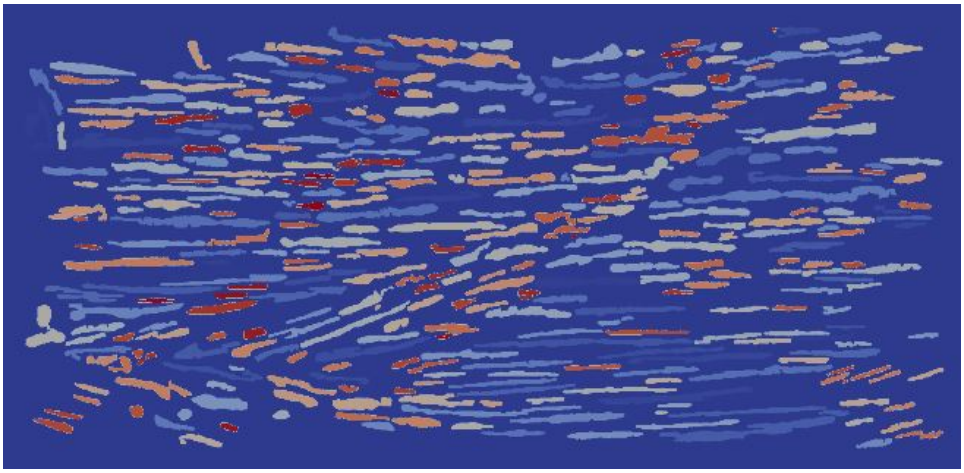

Figure 4.8: α lamellae/laths indexing.

All the numerical parameters of the previous test case are also considered here. Moreover, since in this simulation we include the velocity due to motion by mean curvature, the coefficient A is defined thanks to the value discussed in section 4.2.2 as $A = 0.227\mu m^2 \cdot s^{-1}$. The only difference concerns the time step which is equal to $1min$ as the mean curvature velocity could be important comparatively to the surface diffusion velocity.

Fig. 4.9 illustrates the results obtained.

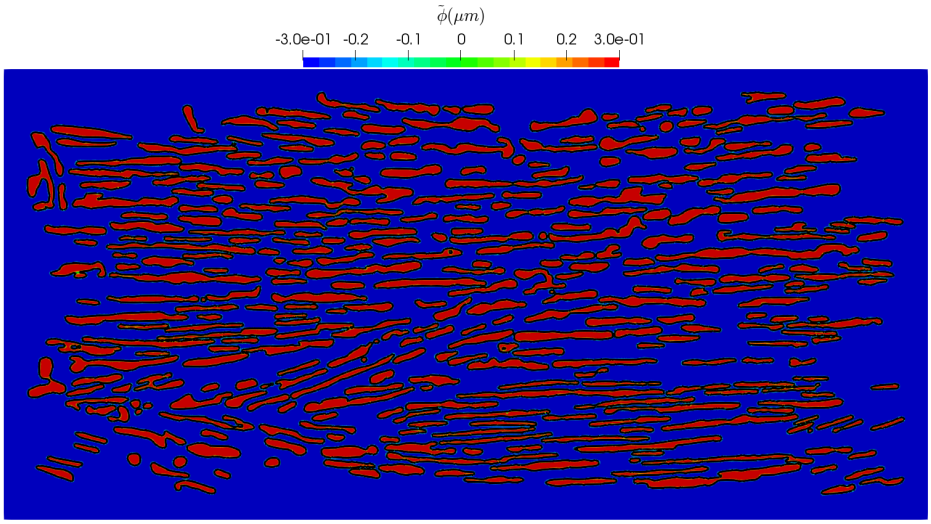

(a) $t = 50days$

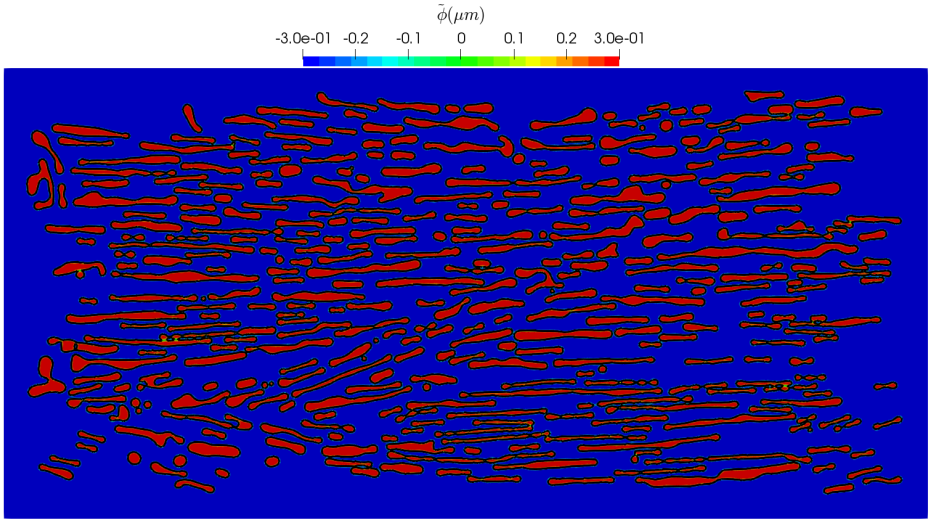

(b) $t = 200days$

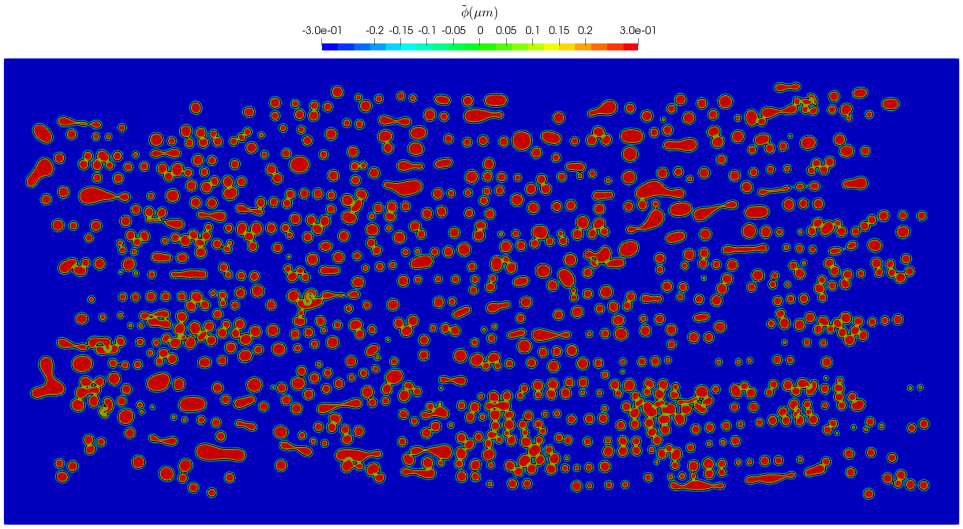

(c) Quasi steady-state

Figure 4.9: α lamellae/laths evolution with motions by surface diffusion and mean curvature.

A different shape evolution is observed in comparison with the case where only surface diffusion was considered for the same microstructure (see Fig. 4.6) and coalescence events are avoided typically where the curvature velocity is activated as illustrated in Fig. 4.10. This element indicates that even without α/α subboundaries considered initially inside the lamellae, the very close proximity (or even contact) of some laths/lamellaes lead to the activation of the curvature velocity with an impact on the global kinetic. The calculation time for this simulation was 5h in 24 CPUs. The fact that each particle is treated separately and the small time step increased the time calculation. Interestingly, surface diffusion seems globally more active in this simulation comparatively to the results described in Fig. 4.6 and at the same time a better volume conservation was observed (1% of area loss at $t = 200days$). This difference can probably be a coupled effect of the smaller time step with the presence of $\vec{v}_k$ in some locations. Moreover, mesh size at the laths/lamellae interfaces is also an important parameter which leads to detect more or less precisely the zone of contact forming α/α interfaces and the α lamellae/laths thicknesses with an impact on the microstructure evolution. This spatial precision is indeed important in the occurence of numerical splitting of very fine and long lamellae under surface diffusion (some examples are evident in the quasi steady-state described by Fig. 4.9c). A thorough study of these elements constitute a perspective of these results.

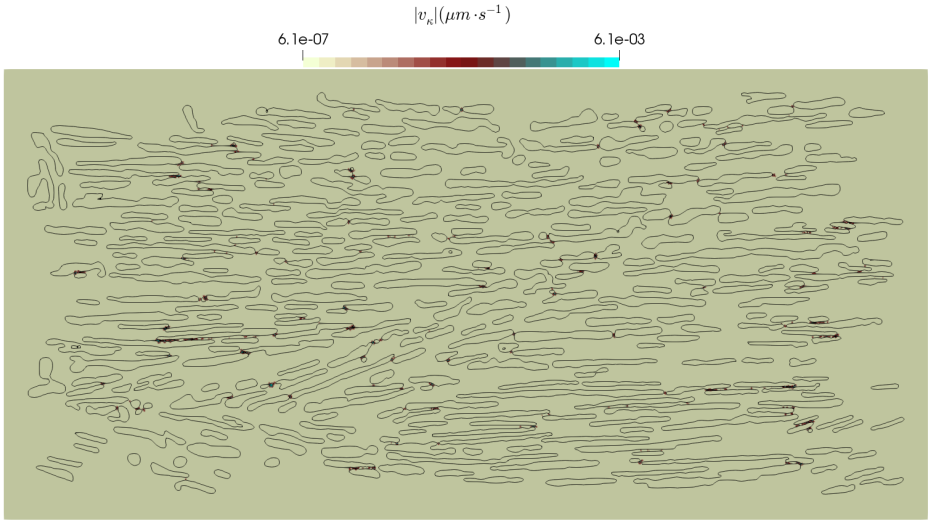

Figure 4.10: $|v_\kappa|$ at $t = 50days$ with black lines for the lamellae/laths interfaces.

In this section, we have proved that we are able to couple the motion of surface diffusion and motion by mean curvature in real microstructures extracted from experimental images.

4.5 Conclusion

In this chapter, it is proven that the proposed numerical framework enables to efficiently simulate the coupling of motion by surface diffusion and motion by mean curvature on real microstructures extracted from experimental images.

Efforts have been made to approximate the physical coefficients in order to perform real time simulations. Further investigation must be done in the future on this topic in order to improve the representativity of our simulations.

A first perspective would be the consideration of a representative number of α/α subboundaries inside the initial microstructure. With the existence of subboundaries we could verify the occurrence of lamellae splitting leading to smaller laths as well as the acceleration of the surface diffusion mechanism comparatively to the kinetics exhibited in this chapter.

Secondly, a long term perspective of this work, is to take into account all the additional mechanisms (coarsening, phase transformation, appearance of subboundaries during deformation, anisotropy of B and A coefficients etc) in order to be even more precise concerning the numerical modeling of the microstructure evolution of titanium alloys during metal forming. Moreover, the proposed numerical strategy is usable in 3D; thus working with realistic

3D shapes for the lamellae/laths constitutes another exciting perspective of this work.

Conclusions-Perspectives

The general objective of this thesis is to contribute to the understanding of the phenomenon of spheroidization in α/β titanium alloys during deformation and prolonged annealing and to introduce a numerical framework to efficiently simulate it. This is of utmost importance since spheroidized microstuctures exhibit higher strength and ductility. The ability to simulate microstructure evolution upon thermomechanical processing and more particularly this phenomenon is thus of interest for the titanium industry.

In Chapter 1, a literature review has been presented summarizing the information found about spheroidization in α/β titanium alloys. Experimental efforts have been made to better describe the evolution of the phenomenon. Various information of great value for our research, were found regarding the governing mechanisms of spheroidization on its different stages. On the other hand, very few attempts have been made until now to efficiently simulate this phenomenon. The focus of this PhD thesis is on modeling the interfacial kinetics. The mathematical description found in literature for the two governing mechanisms of motion by surface diffusion and motion by mean curvature is given. These two mechanisms are responsible for the lamellae splitting during hot deformation and subsequent annealing.

The experiments performed in this thesis, presented in chapter 2, mostly aimed at better understanding the driving mechanisms of the spheroization phenomenon and provided qualitative and quantitative informations regarding the microstructure evolution. The entire work was carried out on the alloy Ti-64 processed at 950 °C. All the mechanisms reported in literature were confirmed throughout the experiments.

Subboundaries formation appear to be the most important factor regarding the spheroidization of the α phase. During deformation, the α lamellae accumulate dislocations, which lead to intralamellar misorientations and the formation of subboundaries. The existence of subboundaries initiates the grooving process through interfacial kinetics that leads to lamellae splitting into shorter laths and eventually to lath spheroidization. The higher the strain the more subboundaries are formed and the faster the α lamellae will split. Furthermore, the size of the lamellae is also an important factor, since it was noticed that the thicker lamellae form less easily subboundaries and undergo a slower α phase evolution. In addition, the orientation of the α

lamellae with respect to the applied deformation is also a very important factor. The lamellae that are initially parallel to the compression direction undergo kinking, leading to quicker fragmentation. Nevertheless, the shape of the α lamellae does not change drastically during hot-deformation but during short or prolonged annealing after deformation. At the early stages of annealing, the interfacial mechanisms as surface diffusion at the α/β interface and motion by mean curvature at the α/α interface are the predominant mechanisms leading to lamellae splitting. During long term annealing, the predominant mechanism switches to be coarsening (bulk diffusion). In fact, except for crystal plasticity that clearly occurs during deformation and leads to the formation of subboundaries, all the other mechanisms of surface diffusion, motion by mean curvature and bulk diffusion, may occur simultaneously, during deformation and during post-deformation annealing.

The numerical part of the thesis is focused on simulating the two mechanisms of surface diffusion and motion by mean curvature, which were identified as being responsible for lamella splitting, and to be predominant in the first stages of post-deformation annealing. A full field approach based on a Level-Set/ Finite Element framework was introduced for that purpose and is compatible with the future implementation of the other involved mechanisms (crystal plasticity and bulk diffusion) to simulate the whole spheroidization process.

Several numerical tools from the state of the art were used as the (κ,v_s)-identification solver developed by Bruchon et al. [20,26,27], providing, in our P1 formulation, the calculation of the curvature and of the surface laplacian of the curvature with a correct precision. Two different approaches were tested for the coupling of motion by mean curvature at the α/α interfaces and motion by surface diffusion at the α/β interfaces.

The first approach is based on a Eulerian framework where the lamellae/laths interfaces described by a distance function ϕ are updated by a classical convection diffusion solver, the convective part corresponding to the surface diffusion velocity and the diffusive one to the motion by mean curvature. Each time step is completed by a Direct Reinitialization method to preserve the metric property of the distance function, followed by a remeshing operation.

The second approach is based on an enhanced Lagrangian framework developed by Shakoor et al. [41, 42]. The first step remains the same, calculation of the curvature and surface laplacian of the curvature. Then the two different velocities of surface diffusion and motion by mean curvature are calculated and added to a final global velocity that couples both motions. With this final velocity, enhanced Lagrangian evolution coupled with remeshing (H-adaptation) of the FE mesh is performed. Direct Reinitialization method is then used. A originality of this strategy is that the volume of each phase is respected precisely when remeshing operations are performed, using a conformed to the interface mesh strategy (FITZ).

Both methods have enabled us to simulate surface diffusion velocity and motion by mean curvature in a unified numerical framework. The results provided from the academic cases have very good time calculation and precision. By comparing the two approaches, it was highlighted that the enhanced Lagragian approach with the use of FITZ (body fitted mesh) is the most efficient one.

This approach was then adopted to deal with real microstructures which were extracted from our experimental results and immersed as geometries in Finite Element meshes. Surface diffusion simulations could thus be performed on real microstructures while respecting the volume conservation and reaching fast time calculations. Finally the most important achievement was the coupling of the two different motions of surface diffusion and motion by mean curvature on real microstructures. Those last simulations gave reasonable time calculations with excellent volume conservation independently of the number of lamellae treated, or their size.

Still further work must be done in order to include all the mechanisms of spheroidization in the simulations. A domain that definitely should be included in the perspectives of this work is the study of the α/β interfaces and diffusion kinetics occurring during deformation and annealing. Studying these aspects is important for getting right values of model parameters. We have indeed proposed a numerical model that is efficiently working regarding a numerical point of view, but it stills missing a better calibration of two physical parameters, the coefficients B for motion by surface diffusion and the coefficient A for motion by mean curvature.

Further model developments should also be done to account for the whole process of spheroidization: crystal plasticity is needed to simulate the formation of the α/α subboundaries during deformation, bulk diffusion for describing coarsening over prolonged annealing. Only if the four different mechanisms would be all immersed in the calculations, it could be stated that a global numerical framework has been built to efficiently simulate the phenomenon of spheroidization at constant phase fractions.

To make the simulation really complete, phase transformation (which also proceeds by bulk diffusion) must be taken into account as well. The phase equilibrium is not only dependent on temperature but also on deformation.

An increase of α volume fraction during deformation has been observed in this work, something that was unexpected because the opposite effect was reported in the literature but in α/β alloys with different initial microstructures (not lamellar). During post-deformation annealing, inverse phase transformation must occur to retrieve static phase equilibrium. Since there are very few information available in literature for this phenomenon in α/β titanium alloys with initial lamellar microstructure and our results do not give a clear image on the subject, further experimental work should be performed to get a better understanding and description of dynamic

phase equilibrium, and how this could participate to the phenomenon of spheroidization.

Finally, 3D microscopy could help in order to obtain informations regarding the shape evolution of an α lamellae in three dimensions during deformation and prolonged annealing, while using also this information in order to perform 3D simulations with the proposed numerical framework. Indeed, if the proposed numerical strategy was detailed and used in 2D in this work, it is directly usable in 3D.

Bibliography

[1] G. Lütjering and J.C. Williams. *Titanium*, volume 2. Springer, 2003.

[2] S.L. Semiatin and D.U. Furrer. Modeling of microstructure evolution during the thermomechanical processing of titanium alloys. Technical report, DTIC Document, 2008.

[3] S. Mironov, M. Murzinova, S. Zherebtsov, G.A. Salishchev, and S.L. Semiatin. Microstructure evolution during warm working of Ti-6Al-4V with a colony-α microstructure. *Acta Materialia*, 57(8):2470 – 2481, 2009.

[4] S. Zherebtsov, M. Murzinova, G. Salishchev, and S.L. Semiatin. Spheroidization of the lamellar microstructure in Ti-6Al-4V alloy during warm deformation and annealing. *Acta Materialia*, 59:4138 – 4150, 2011.

[5] N. Stefansson and S.L. Semiatin. Mechanisms of globularization of Ti-6Al-4V during static heat treatment. *Metallurgical and Materials Transactions A*, 34(3):691–698, 2003.

[6] N. Stefansson, S.L. Semiatin, and D. Eylon. The kinetics of static globularization of Ti-6Al-4V. *Metallurgical and Materials Transactions A*, 33(11):3527–3534, 2002.

[7] I. Weiss, F.H. Froes, D. Eylon, and G.E. Welsch. Modification of alpha morphology in Ti-6Al-4V by thermomechanical processing. *Metallurgical and Materials Transactions A*, 17(11):1935–1947, 1986.

[8] H. Margolin and P. Cohen. Evolution of the equiaxed morphology of phases in Ti-6Al-4V. *Titanium'80*, 1:1555–1561, 1980.

[9] H. Margolin and P. Cohen. Kinetics of recrystallization of alpha in Ti-6Al-4V. *Titanium'80,*, 4:2991–2997, 1980.

[10] G.A. Salishchev, S.V. Zerebtsov, S. Mironov, and S.L. Semiatin. Formation of grain boundary misorientation spectrum in alpha-beta titanium

alloys with lamellar structure under warm and hot working. In *Materials Science Forum*, volume 467, pages 501–506. Trans Tech Publ, 2004.

[11] W.W. Mullins. The effect of thermal grooving on grain boundary motion. *Acta Metallurgica*, 6(6):414–427, 1958.

[12] C. Herring. Effect of change of scale on sintering phenomena. *Journal of Applied Physics*, 21(4):301–303, 1950.

[13] C. Herring. Surface tension as a motivation for sintering. *The physics of powder metallurgy*, 27(2):143–179, 1951.

[14] B. H. Prada, J. Mukhopadhyay, and A. K. Mukherjee. Effect of strain and temperature in a superplastic Ni-modified Ti-6Al-4V alloy. *Materials Transactions, JIM*, 31(3):200–206, 1990.

[15] J. Koike, Y. Shimoyama, I. Ohnuma, T. Okamura, R. Kainuma, K. Ishida, and K. Maruyama. Stress-induced phase transformation during superplastic deformation in two-phase Ti-Al-Fe alloy. *Acta Materialia*, 48(9):2059 – 2069, 2000.

[16] J. J. Jonas, C. Aranas, A. Fall, and M. Jahazi. Transformation softening in three titanium alloys. *Materials and Design*, 113:305 – 310, 2017.

[17] H.S. Yang, G. Gurewitz, and A.K. Mukherjee. Mechanical behavior and microstructural evolution during superplastic deformation of Ti-6Al-4V. *Materials Transactions, JIM*, 32(5):465–472, 1991.

[18] H. Matsumoto, K. Yoshida, S.-H. Lee, Y. Ono, and A. Chiba. Ti-6Al-4V alloy with an ultrafine-grained microstructure exhibiting low temperature high strain-rate superplasticity. *Materials Letters*, 98:209 – 212, 2013.

[19] V. Derkach. Surface evolution and grain boundary migration in a system of 5 grains. *Research Thesis Technion- Israel Institut of Technology*, 2010.

[20] J. Bruchon, D. Pino Muñoz, F. Valdivieso, and S. Drapier. Finite element simulation of mass transport during sintering of a granular packing. part i. surface and lattice diffusions. *Journal of the American Ceramic Society*, 95(8):2398–2405.

[21] S.L. Semiatin and D.U. Furrer. Modeling of microstructure evolution during the thermomechanical processing of titanium alloys. *ASM Handbook*, 22:522–535, 2009.

[22] S.L. Semiatin, S.L. Knisley, P.N. Fagin, D.R. Barker, and F. Zhang. Microstructure evolution during alpha-beta heat treatment of Ti-6Al-4V. *Metallurgical and Materials Transactions A*, 34(10):2377–2386, 2003.

[23] S. Osher and J.A. Sethian. Fronts propagating with curvature-dependent speed: Algorithms based on hamilton-jacobi formulations. *Journal of Computational Physics*, 79(1):12 – 49, 1988.

[24] J.A. Sethian. A fast marching level set method for monotonically advancing fronts. *Proceedings of the National Academy of Sciences*, 93(4):1591–1595, 1996.

[25] P. Smereka. Semi-implicit level set methods for curvature and surface diffusion motion. *Journal of Scientific Computing*, 19(1):439–456, 2003.

[26] J. Bruchon, D. Pino Muñoz, F. Valdivieso, S. Drapier, and G. Pacquaut. 3D simulation of the matter transport by surface diffusion within a level-set context. *European Journal of Computational Mechanics/Revue Européenne de Mécanique Numérique*, 19(1-3):281–292, 2010.

[27] J. Bruchon, S. Drapier, and F. Valdivieso. 3D finite element simulation of the matter flow by surface diffusion using a level set method. *International Journal for Numerical Methods in Engineering*, 86(7):845–861, 2011.

[28] H. Digonnet and T. Coupez. Object-oriented programming for "fast and easy" development of parallel applications in forming processes simulation. In *Computational Fluid and Solid Mechanics 2003*, pages 1922–1924. Elsevier, 2003.

[29] M. Bernacki, Y. Chastel, T. Coupez, and R.E. Logé. Level set framework for the numerical modelling of primary recrystallization in polycrystalline materials. *Scripta Materialia*, 58(12):1129 – 1132, 2008.

[30] L. Ville, L. Silva, and T. Coupez. Convected level set method for the numerical simulation of fluid buckling. *International Journal for Numerical Methods in Fluids*, 66(3):324–344, 2011.

[31] M. Bernacki, H. Resk, T. Coupez, and R.E. Logé. Finite element model of primary recrystallization in polycrystalline aggregates using a level set framework. *Modelling and Simulation in Materials Science and Engineering*, 17(6):064006, 2009.

[32] M. Shakoor, B. Scholtes, P.-O. Bouchard, and M. Bernacki. An efficient and parallel level set reinitialization method – application to micromechanics and microstructural evolutions. *Applied Mathematical Modelling*, 39(23):7291 – 7302, 2015.

[33] B. Scholtes, M. Shakoor, A. Settefrati, P.-O. Bouchard, N. Bozzolo, and M. Bernacki. New finite element developments for the full field modeling of microstructural evolutions using the level-set method. *Computational Materials Science*, 109:388 – 398, 2015.

[34] M. Bernacki, R.E. Logé, and T. Coupez. Level set framework for the finite-element modelling of recrystallization and grain growth in polycrystalline materials. *Scripta Materialia*, 64(6):525–528, 2011.

[35] M. Bernacki, H. Resk, T. Coupez, and R.E. Logé. Finite element model of primary recrystallization in polycrystalline aggregates using a level set framework. *Modelling and Simulation in Materials Science and Engineering*, 17(6):064006, 2009.

[36] C. Gruau and T. Coupez. 3D tetrahedral, unstructured and anisotropic mesh generation with adaptation to natural and multidomain metric. *Computer Methods in Applied Mechanics and Engineering*, 194(48):4951 – 4976, 2005. Unstructured Mesh Generation.

[37] J. Bruchon, H. Digonnet, and T. Coupez. Using a signed distance function for the simulation of metal forming processes: Formulation of the contact condition and mesh adaptation. from a lagrangian approach to an eulerian approach. *International journal for numerical methods in engineering*, 78(8):980–1008, 2009.

[38] R.C. Almeida, R.A. Feijóo, A.C. Galeao, C. Padra, and R.S. Silva. Adaptive finite element computational fluid dynamics using an anisotropic error estimator. *Computer Methods in Applied Mechanics and Engineering*, 182(3-4):379–400, 2000.

[39] R. Boussetta, T. Coupez, and L. Fourment. Adaptive remeshing based on a posteriori error estimation for forging simulation. *Computer methods in applied mechanics and engineering*, 195(48-49):6626–6645, 2006.

[40] Y. Mesri, W. Zerguine, H. Digonnet, L. Silva, and T. Coupez. Dynamic parallel adaption for three dimensional unstructured meshes: Application to interface tracking. In Rao V. Garimella, editor, *Proceedings of the 17th International Meshing Roundtable*, pages 195–212, Berlin, Heidelberg, 2008. Springer Berlin Heidelberg.

[41] M. Shakoor, P.-O. Bouchard, and M. Bernacki. An adaptive level-set method with enhanced volume conservation for simulations in multiphase domains. *International Journal for Numerical Methods in Engineering*, 109(4):555–576, 2017.

[42] M. Shakoor, M. Bernacki, and P.-O. Bouchard. A new body-fitted immersed volume method for the modeling of ductile fracture at the

microscale: Analysis of void clusters and stress state effects on coalescence. *Engineering Fracture Mechanics*, 147:398 – 417, 2015.

[43] S. Osher and J.A. Sethian. Motion by intrinsic laplacian of curvature. *Interfaces and Free Boundaries*, 1(1):107–123, 1 1999.

[44] H. Garcke, B. Nestler, and B. Stoth. A multiphase field concept: numerical simulations of moving phase boundaries and multiple junctions. *SIAM Journal on Applied Mathematics*, 60(1):295–315, 1999.

[45] Y. Jin, N. Bozzolo, A.D. Rollett, and M. Bernacki. 2D finite element modeling of misorientation dependent anisotropic grain growth in polycrystalline materials: Level set versus multi-phase-field method. *Computational Materials Science*, 104(Supplement C):108 – 123, 2015.

[46] S. Florez, T. Toulorge, and M. Bernacki. Body-fitted remeshing of moving interfaces. Technical report, DIGIMU project, 2018.

[47] J. Humphreys, G.S. Rohrer, and A. Rollett. *Recrystallization and related annealing phenomena (third edition)*. Elsevier, 2017.

[48] S.L. Semiatin, B.C. Kirby, and G.A. Salishchev. Coarsening behavior of an alpha-beta titanium alloy. *Metallurgical and Materials Transactions A*, 35(9):2809–2819, 2004.

[49] S.L. Semiatin, T.M. Brown, T.A. Goff, P.N. Fagin, R.E. Turner, J.M. Murry, D.R. Barker, J.D. Miller, and F. Zhang. Diffusion coefficients for modeling the heat treatment of Ti-6Al-4V. *Metallurgical and Materials Transactions A*, 35(9):3015–3018, 2004.

[50] G.L.J. Bailey and H.C. Watkins. Surface tensions in the system solid copper-molten lead. *Proceedings of the Physical Society. Section B*, 63(5):350, 1950.

[51] C.S. Smith. Grains, phases, and interphases: an interpretation of microstructure. *Trans. Metall. Soc. AIME*, 175:15–51, 1948.

[52] W.T. Read and W. Shockley. Dislocation models of crystal grain boundaries. *Phys. Rev.*, 78:275–289, 1950.

[53] W.W. Mullins. Two-dimensional motion of idealized grain boundaries. *Journal of Applied Physics*, 27(8):900–904, 1956.

Résumé

Les alliages de titane α/β ont beaucoup d'applications dans des domaines industriels divers comme l'aéronautique. Le phénomène de globularisation qui se produit lors de traitements thermomécaniques est un phénomène important dans la mesure où une microstructure globulaire présente une tenue mécanique et une ductilité accrues.
Les microstructures lamellaires sont constituées de colonies de lamelles de phase α parallèles qui se développent dans les grains β au cours de leur refroidissement. La globularisation se fait en deux étapes : les lamelles se subdivisent d'abord en segments plus courts, puis ces segments globularisent, au cours de la déformation à chaud et des traitements thermiques. La subdivision des lamelles se fait au niveau des sous-joints formés au cours de la déformation à chaud. Lors de traitements thermiques prolongés, les plus gros globules de phase α grossissent au détriment des plus petits. La formation des sous-joints et le grossissement des globules n'ont pas été étudiés en détail dans ce travail. L'accent a été mis sur les mécanismes de migration des interfaces α/β et α/α qui conduisent à la subdivision des lamelles et à leur globularisation.
Des essais de compression à chaud et des traitements thermiques appliqués à des échantillons de Ti-6Al-4V ont permis de confirmer que l'épaisseur des lamelles et de leur orientation sont des facteurs importants pour la globularisation. Les lamelles plus fines et celles orientées parallèlement à l'axe de compression globularisent plus facilement. Ce travail expérimental a permis de mieux appréhender la complexité du phénomène de globularisation et d'introduire un cadre numérique adapté pour sa simulation. Une méthode à champ complet, basée sur la méthode Level-Set dans un cadre Eléments Finis, a ainsi été testée pour simuler les mécanismes physiques de migration interfaciale menant à la subdivision des lamelles et à l'évolution vers une forme globulaire. Les premiers résultats sont très prometteurs et illustrent le potentiel du cadre numérique proposé.

Mots Clés

Globularisation, alliage de titane α/β, analyse expérimentale, simulation des mécanismes physiques de migration interfaciale, éléments finis, level-set, méthode à champ complet.

Abstract

α/β titanium alloys have many industrial applications in various fields such as aeronautics. Spheroidization is a phenomenon that occurs in initially lamellar α/β titanium alloys during thermomechanical processing and receives considerable attention as spheroidized microstructures exhibit enhanced strength and ductility.
Lamellar microstructures are made of colonies of parallel α lamellae developed inside β grains while they are cooled down. Spheroidization actually proceeds in two successive steps: the lamellae first split into smaller α laths, which subsequently undergo spheroidization. This occurs during hot-deformation and subsequent annealing. Lamella splitting occurs where subboundaries were formed inside lamellae during hot-deformation. Over long term annealing the spheroidized α phase particles undergo coarsening. The formation of subboundaries and coarsening were not addressed in this work. The focus has been placed on the interfacial kinetics mechanisms leading α lamellae splitting during the first stages of spheroidization.
Hot compression tests and subsequent annealings carried out on Ti-6Al-4V samples confirmed that the thickness and the orientation of the lamellae are important factors with regards to spheroidization. Thinner lamellae and lamellae oriented parallel to the compression axis spheroidize faster. Those experiments contributed to a better understanding of the phenomenon and allowed to introduce a suitable numerical framework to simulate the early stages of spheroidization. A full field method in a Finite Element/ Level Set framework has thus been tested for simulating the involved physical mechanisms of interface migration that lead to lamellae splitting and the subsequent shape evolution of the α laths towards a spheroidal shape. First results are promising and illustrate the potential of this numerical framework

Keywords

Spheroidization, α/β titanium alloys, experimental analysis, simulation of the physical mechanisms of interfacial migration, finite element method, level-set, full field method.